



L-Università ta' Malta
Faculty of Engineering

Master of Science in Engineering Dissertation

Characterization of Insertion Devices Using a Micro-Magnetic Measurement Bench

Mohamed R. Bashir ATTIR

Supervised by:

Prof. Ing. Andrew. SAMMUT

Co-supervised by:

Prof. Ing Nicholas SAMMUT

*A dissertation submitted in partial fulfilment of the requirements
for the degree of Master of Science in Engineering*

by the

Faculty of Engineering

March 2024



L-Universit`
ta' Malta

University of Malta Library – Electronic Thesis & Dissertations (ETD) Repository

The copyright of this thesis/dissertation belongs to the author. The author's rights in respect of this work are as defined by the Copyright Act (Chapter 415) of the Laws of Malta or as modified by any successive legislation.

Users may access this full-text thesis/dissertation and can make use of the information contained in accordance with the Copyright Act provided that the author must be properly acknowledged. Further distribution or reproduction in any format is prohibited without the prior permission of the copyright holder.

Copyright Notice

1. Copyright in text of this dissertation rests with the Author. Copies (by any process) either in full, or of extracts may be made only in accordance with regulations held by the Library of the University of Malta. Details may be obtained from the Librarian. This page must form part of any such copies made. Further copies (by any process) made in accordance with such instructions may not be made without the permission (in writing) of the Author.
2. Ownership of the right over any original intellectual property which may be contained in or derived from this dissertation is vested in the University of Malta and may not be made available for use by third parties without the written permission of the University, which will prescribe the terms and conditions of any such agreement.
3. Publication rights over the academic and/or research results presented in this dissertation are vested jointly in both the Author and his/her academic Supervisor(s), and unless such rights are explicitly waived in writing, both parties must be listed among the authors in any academic publication that is derived substantially from this work. Furthermore, any other public communication / disclosure of any form that focuses on the project must acknowledge that this work has been carried out by the Author and the Supervisor(s) (named explicitly) through the University of Malta.



UNIVERSITY OF MALTA

FACULTY/INSTITUTE/CENTRE/SCHOOL Engineering

DECLARATION BY POSTGRADUATE STUDENTS

Student's Code 0125524A

Student's Name & Surname Mohamed R. Bashir ATTIR

Course Master of Science in Engineering

Title of Long Essay/Dissertation

Characterization of Insertion Devices Using a Micro-Magnetic Measurement Bench

Word Count 32000

- (a). Authenticity of Long Essay/Dissertation** I hereby declare that I am the legitimate author of this Long Essay/Dissertation and that it is my original work. No portion of this work has been submitted in support of an application for another degree or qualification of this or any other university or institution of higher education. I hold the University of Malta harmless against any third party claims with regard to copyright violation, breach of confidentiality, defamation and any other third party right infringement.
- (b). Research Code of Practice and Ethics Review Procedures** I declare that I have abided by the University's Research Ethics Review Procedures. Research Ethics & Data Protection form code.

Signature of Student

MOHAMED R. BASHIR ATTIR
Name of Student (in Caps)

Date

Funding

This research project was funded by the University of Malta in Msida, Malta and the Paul Scherrer Institute (PSI) in Villigen, Switzerland.



Acknowledgements

I would like to extend my sincere gratitude to the Insertion Devices Group at PSI. The opportunity to work within such a distinguished team and facility has been nothing short of a privilege. Their willingness to share expertise and foster a collaborative environment has been a cornerstone of my research journey. So thank you *Dr. Thomas Schmidt, Dr. Marco Calvi, Mr. Marc Brügger, Mr. Steffen Danner, Mr. Lars Huber, Mr. Marcus Schmidt* and *Dr. Sebastian Richter*.

I owe a great deal of appreciation to my supervisors *Dr. Andrew Sammut* and *Dr. Nicholas Sammut* for their invaluable guidance and steadfast support, which began even before my research officially started. Their wisdom, encouragement, and constant help have been critical to my development and success in this endeavor.

My family deserve special recognition for their unwavering support, which has been the most significant to me. The encouragement, understanding, and endless patience they have shown me are the pillars upon which I leaned throughout this journey.

This journey has been one of growth, challenge, and discovery, made possible by many people. To everyone who has played a part, your contributions have enriched my experience and left a lasting impact on both my personal and academic life. May this be a positive step for a brighter future.

Dedicated to my family

Mohamed Attir

March 2024

Abstract

Light sources are structures that produce intense beams of electromagnetic light such as X-rays. The produced light can be used in various research fields such as the study of material's structure and dynamics at a molecular and atomic levels. The Swiss Free Electron Laser (SwissFEL) and Swiss Light Source (SLS) are two examples of light sources that are operated by the Paul Scherrer Institute (PSI) in Switzerland. An undulator is an insertion device that is the key component to generate the desired electromagnetic light with great intensity and the ability for tuning over a wide range of wavelengths. Undulators are constructed from a series of magnetic elements that create a magnetic field along the device forcing accelerated electrons, such as those from free electron laser, to oscillate and radiate light in a desired wavelength.

It is essential to characterize undulators to ensure the correct electromagnetic light is generated and an overall optimal performance of the light source structure is maximised. Magnetic measurement benches play a crucial role in this process by utilizing magnetic field sensors such as Hall probes to measure the magnetic field profile and analyse the properties of insertion devices. At PSI, the new generation of undulators are to be installed inside a narrow vacuum chamber which results in a more constrained characterization environment, hence, the need for a miniature magnetic measurement bench that can navigate inside the narrow chamber, measure the magnetic field with high precision and accuracy on-site is of high significance. Given the physical constraints of the new generation of undulators, and the lengthy process of commissioning and deploying new ones, the need for a compact, precise and modular measurement bench is of high importance.

This dissertation follows the improvements on the implemented prototype of a micro magnetic measurement bench and the integration of all systems on one single printed circuit board, such that all components can travel freely along the undulator while correcting the Hall probe sensor position drifts in 2-degrees of freedom. The traversal movement is achieved via a linear motor, and the probe drift correction is tracked via the use of precision laser positioning system. The corrections are then performed via 2 mechanical stages linked to 2 miniature motors. The magnetic measurement and data acquisition is performed by a previously developed small form-factor, 3-axes Teslameter. The bench was tested on a prototype undulator with passive force compensation side magnets which is planned to be utilised in an upcoming upgrade to the SLS facility (upgrade to SLS2.0). The prototype undulator with force compensation magnets was characterised nonetheless using the implemented bench and the effect of the side magnets on the field enhancing magnets was studied and quantified.

Table of Contents

Copyright Notice	i
Declaration of Authorship	ii
Funding	iii
Acknowledgements	iv
Abstract	v
Contents	vi
List of Figures	ix
List of Tables	xii
List of Acronyms	xiv
1 Introduction	1
1.1 Research Topic Introduction	1
1.2 Project Overview	3
1.3 Research Goals	3
1.4 Dissertation Structure	4
2 Literature Review	6
2.1 Light Sources Working Principles	6
2.2 Measurement Benches	9
2.2.1 Granite Slab Based Measurement Benches	10
2.2.2 The Magnetic Measurement System CASPER	15
2.2.3 The ALBA Magnetic Measurement System	15
2.2.4 SAFALI Based Measurement Bench	17
2.2.5 Magnetic Measurement Benches at PSI	19
2.2.5.1 Measurement Benches for the ARAMIS Undulators	20
2.2.5.2 Micro Magnetic Measurement Bench	22
2.3 New SLS2.0 Undulator Prototype	24

2.4	Literature Review Conclusion	28
3	Bench Overview & Motion Controls	30
3.1	Overview of the Implemented Mechanical Bench	31
3.1.1	Hall Probe Positioning System	32
3.1.2	Magnetic Pole Adjustment System	34
3.1.3	Limitations of the Previously Implemented Mechanical System	35
3.2	Overview of the Previously Implemented Electronic System	36
3.2.1	Limitations of the Previously Implemented Electronics System	38
3.3	Improvements on the Previously Implemented Bench	39
3.4	Motion Control Design and Performance	42
3.4.1	Linear Motor Performance	45
3.4.2	Overview of the CAN Bus	49
3.4.3	Implementation of the CAN Bus	53
3.4.3.1	Software of the CANopen Bus	56
3.4.4	Hall Probe Positioning System Controllers & Performance . . .	58
3.4.4.1	PSDs Working Principle	60
3.4.4.2	Position Feedback Loop Overview and Performance . . .	63
3.5	Chapter Summary	74
4	Communication, Software & PCBs	75
4.1	USB Connection to the Teslometer	75
4.1.1	Overview of USB Link	76
4.1.2	Implementation of the USB Link	78
4.2	EnDat Communication Link	80
4.2.1	Implementation of EnDat	83
4.3	Printed Circuit Boards	85
4.3.1	PLC side PCB	86
4.3.2	Base PCB	87
4.3.2.1	Power Delivery and Regulators	89
4.3.3	Control PCB	90
4.4	Main μ MMB Program Flow	92
4.5	Chapter Summary	96
5	Magnetic Measurements of the New Undulator	97
5.1	Measurement Setup	97
5.2	Test Plan	100
5.2.1	Finding the Vertical Centre	101
5.2.2	Repeatability Testing	104
5.2.2.1	Sources of Error Investigation	107
5.2.3	Magnetic Measurement at Different Gaps	111
5.2.4	Magnetic Field at Different Horizontal Offsets	113
5.3	Chapter Summary	115
6	Discussions & Conclusion	117
6.1	Summary of the Dissertation	117
6.2	Summary of the Research Goals and Results Achieved	117
6.3	Limitations of the μ MMB	118

6.3.1	Mechanical Bench	118
6.3.2	Electronics System	120
6.4	Future Improvements	121
 Bibliography		129
 Appendix		130

List of Figures

1.1	Basic SwissFEL Structure	1
2.1	Functional Principles of Light Sources and Synchrotron Radiation . .	7
2.2	The Concept of Electron Bunching and Coherent Light Generation . .	7
2.3	Operational Gap of an Undulator	9
2.4	Granite Base Magnetic Measurement Bench at ESRF	11
2.5	Hall Probe Bench Under Laser Calibration at ESRF	12
2.6	One of the Motorised Stage for the Stretched Wire Field Integral Bench at ESRF	13
2.7	Granite Slab Used for SLS Measurement Bench at PSI	14
2.8	The Hall Probe Mover Assembly for The Granite Measurement Bench at PSI	14
2.9	Hall Probe Bench Prototype Using a Stretched Tape (Red Line) and a Hall Probe (Blue Dot)	16
2.10	Schematic Illustration of the SAFALI System to Measure IVUs	18
2.11	The Hall Probe Position with and Without Position Correction	19
2.12	The Structure of a Magnetic Array Used in the ARAMIS Undulators with the Screw Driven Wedge Flexors	20
2.13	Simplified Block Diagram of Bench A for the ARAMIS Undulators . .	21
2.14	3D Render of the μ MMB Assembled Inside a Vacuum Chamber	23
2.15	μ MMB for IVUs	24
2.16	The RADIA Model of the New Undulator Magnets with Force Com- pensation Side Magnets	25
2.17	The Undulator Vacuum Chamber Unit with Attached Gap Drive System	26
2.18	The Attractive Magnetic Force Between Undulator Arrays with and Without Force Compensation Magnets	27
2.19	The undulator consists of four FM arrays (orange and blue) and eight CM arrays (green)	28
3.1	The μ MMB Fitted Inside a Segment of The Designated Vacuum Chamber	31
3.2	A 3D Model of the μ MMB's Two Main Components Highlighted . . .	32
3.3	A 3D Model of the Hall Probe Positioning System	33
3.4	A Sketch of the Vertical Drive of the Probe Positioning System	33
3.5	A Sketch of the Horizontal Drive of the Probe Positioning System . .	34
3.6	A 3D Model of the Magnetic Pole Adjustment System	35
3.7	The Previously Implemented Mechanical μ MMB	35
3.8	Block Diagram of the Previously Implemented Bench	38
3.9	The Implemented PCBs for μ MMB	39

3.10	The Old and the New Hall Probe Holders	40
3.11	The Space Available Inside the New Vacuum Chamber	41
3.12	Block Diagram of the New Implementation of the μ MMB	42
3.13	Airex C10 Series Linear Motor	43
3.14	Linear Motor Commutation Solution	44
3.15	Custom PCB for the Hall Effect Sensors	45
3.16	Custom Commutation PCB attached to the Bench	45
3.17	Block Diagram of the Velocity Controller of the MCLM3002	46
3.18	Initial Linear Motor Step Response - $K_P = 90$, $K_i = 60$	47
3.19	Ambient Noise Levels of the Velocity Values from the Motion Controller	48
3.20	Linear Motor Velocity Step Response - $K_P = 110$, $K_i = 70$	49
3.21	Block Diagram of a Generic CAN Network	50
3.22	CAN Message Format	51
3.23	CANopen SDO Message Format for the Faulhaber Motion Controllers	51
3.24	MCBL3002/MCLM3002 Motion Controller From Faulhaber	52
3.25	Block Diagram of the Implemented CANopen Bus	53
3.26	Schematics of the Implemented CANopen Bus	54
3.27	Schematics of a Motion Controller	55
3.28	Custom Component Created of the Control PCB	55
3.29	Block Diagram of the Position Controller of the MCBL3002	59
3.30	Block Diagram of the Implemented SAFALI System	60
3.31	One-Dimensional PSD Cross-section	61
3.32	Simplified Diagram of the Two-Dimensional PSD	62
3.33	(a). Incident Light on the PSDs When Probe is Aligned (b). Incident Light on the PSDs When a Displacement error is Present in the Probe Holder Position	63
3.34	Flowchart of the PLC Programs Loops Running in Parallel	64
3.35	Correction Message Bundled on the PLC to be Sent Over ZigBee	65
3.36	ZigBee Network Between the PLC and the Raspberry Pi	66
3.37	Schematics for the PLC Interface Circuitry	67
3.38	XBee S2C TH and XBee S2C SMD	68
3.39	The Closed-Loop vs Open-Loop Performance of the Hall Probe Positional System	69
3.40	A Simplified Illustration of the Test Setup for th Hall Probe Positioning System	70
3.41	Stability of the Hall Probe Positioning System with and without Feedback	71
3.42	Probe Positional System Y-axis Performance - X-axis Correction is Disabled	72
3.43	The Complete Feedback Loop of the Hall Probe Positioning System	72
3.44	Feedback Loop Sampling Time Distribution	73
4.1	Chunk of Data Received from the Teslameter (20-Bytes)	78
4.2	USB Isolation Schematics	79
4.3	Overview of the Signals and Components of the EnDat Interface	81
4.4	EnDat2.2 Data Transmission of Position Values and Timing Diagram	82
4.5	EnDat Interface Initialisation Process	83
4.6	Schematics of the EnDat Interface Circuitry and Connector	84

4.7	Block Diagram of the Electronic System	85
4.8	The 3D Version and the Manufactured Version of the PLC Side PCB	86
4.9	Base PCB Component Segmentation (a). Power Input, Battery Charging and Power Regulation Segment (b). Middle Segment of the Base PCB with the Control PCB (top grey PCB) and the Teslameter (bottom blue box) (c). Motion Controllers Segment	88
4.10	The 3D and Manufactured Base PCB (a). Designed Base PCB (b). Manufactured and Assembled Base PCB	88
4.11	The Power Delivery Block Diagram of the μ MMB	89
4.12	The 3D Version of the Designed Base PCB	91
4.13	The 3D Version of the Designed Base PCB	92
4.14	Main Loop of the μ MMB Program	93
4.15	PLC Commands to Operate the Bench over the ZigBee Wireless Link	94
4.16	Flowchart of the Magnetic Measurement Mode	95
5.1	3D Model of the Test Setup	98
5.2	Actual Test Setup Used to Characterise the new Undulator Prototype	98
5.3	Illustration of the Test Setup	99
5.4	Serial Test Matrix to Evaluate the Bench's Performance and Characterise the Prototype Undulator	100
5.5	The Variable Gap U-Frame (blue frame) & and the Accompanied HMI	101
5.6	RMS Vertical Magnetic Field vs Relative Offset	103
5.7	Typical Magnetic Measurement Performed at a gap of 6mm and a Velocity of 10mm/s	105
5.8	An Illustration of the Linear Interpolation on a Reference Magnetic Measurement	106
5.9	The Superimposed Percentage Errors from the 100 Magnetic Measurements at each Position	106
5.10	The Maximum, Mean, and Standard Deviation of the 100 Magnetic Measurements at each Position	107
5.11	The Errors of the Hall Probe Position During the 100 Magnetic Measurements at each Position	108
5.12	The FFT Analysis for the Four Test Conditions Including FFT From a Typical Magnetic Measurement	110
5.13	The New Probe Holder Stage - Linear Bearings Slot Highlighted in Red	111
5.14	Measurements Results of the Gap vs K correlation for 11 Different Gaps	113
5.15	Model and Manufactured Magnets for the Force Compensated Prototype Undulator (The radia model differs from the manufactured magnets - due to time constraints from the manufacturing process)	114
5.16	The Effect of the Force Compensation Magnets on the Main Field of the Undulator	115
6.1	Main Controller Future Upgrade Suggestions for the μ MMB	122
A.1	The Schematics of the Stand-alone Battery Charger	130
A.2	The Schematics of the Raspberry Pi Zero W	131

List of Tables

3.1	List of Frequently used indices for OD Objects for the Faulhaber Motion Controllers MCLM3002 & MCBL3002	57
3.2	CONTROLWORD Byte and the Corresponding STATUSWORD . . .	58
4.1	Command List Implemented in the 3-axes Teslameter Instrument . . .	77
4.2	EnDat Mode Command Set as Defined by the Standard [1]	81
5.1	Performance Comparison Between Current Bench, Previously Implemented Bench, and the Teslameter as a Stand-alone Instrument	107

List of Acronyms

SwissFEL Swiss Free Electron Laser.

SLS Swiss Light Source.

PSI Paul Scherrer Institute.

IVU In-Vacuum Undulator.

CPMU Cryogenic Permanent Magnets Undulator.

SAFALI Self-Aligned Field Analyser with Laser Instrumentation.

CASPER ChAracterization SetuP for field Error Reduction.

DOA Degrees Of Adjustment.

PSD Position Sensitive Diodes.

CAN Controlled Area Network.

GUI Graphical User Interface.

PCB Printed Circuit Board.

PLC Programmable Logic Controller.

HMI Human Machine Interface.

Chapter 1

Introduction

1.1 Research Topic Introduction

Light sources such as the Swiss Free Electron Laser (SwissFEL) or Swiss Light Source (SLS) play a crucial role in various research fields such as biology, chemistry and material science. For instance, in material science, light sources enable scientists to investigate the properties and internal bonds of materials on a molecular and atomic level. This helps to construct a more comprehensive understanding of the behaviour of different materials under extreme conditions and provide sufficient knowledge to improve key features in their properties.

The ability for studying materials at this scale is due to the use of X-rays. Fundamental laws of optics state that the smallest structure that can be distinguished is approximately the size of the wavelength of the light bounced from that object. The wavelength range of the visible light is between 380nm and 700nm. Therefore, to be able to distinguish atom sized objects and specific atomic bonds, light with very short wavelength is required. X-rays wavelength is in the range between 10nm and 0.01nm making X-rays the ideal light to be used to study atomic phenomena.

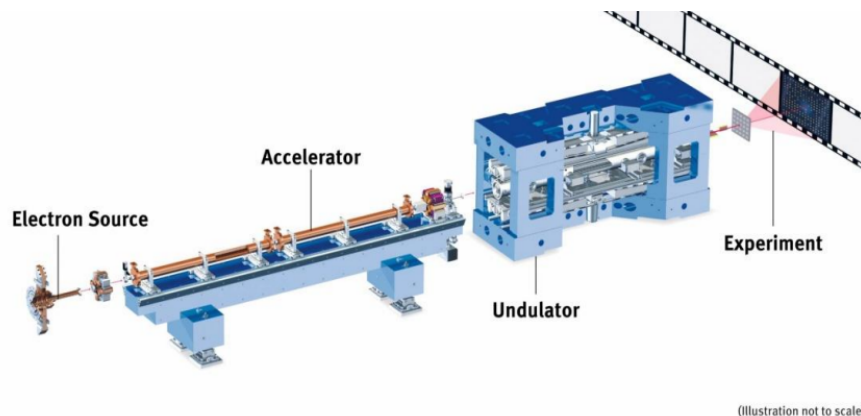


Figure 1.1: Basic SwissFEL Structure [2]

Figure 1.1 shows the basic structure of SwissFEL which was built and is currently operated by Paul Sherrer Institute (PSI). The main components of SwissFEL are the electron source at the beginning of the machine, followed by an RF linear accelerator that gathers, aligns and accelerates the electrons to nearly the speed of light. The accelerated electrons then pass-through insertion devices such as undulators to produce the required light for experiments to be carried out at the end of the machine.

Undulators are the crucial component responsible of generating the light of specific wavelength needed to conduct various experiments. To ensure precise control over the generated light, undulators need to be characterised and optimised for various working conditions. This is done by conducting a measurement campaign of the magnetic field of undulators at different configurations, analyse the results and optimise for the various operating conditions and requirements accordingly. In-Vacuum Undulators (IVU) are very common nowadays since they allow for small gap operation resulting in stronger fields when using permanent magnet undulators. A disadvantage of IVUs are their setup and optimisation periods are substantially longer than out-of-vacuum undulators. When an undulator is installed inside a vacuum chamber and is in operation, it is very difficult to optimise without the need of taking apart the apparatus of the chamber and any other tuning systems around it such that magnetic measurements can be performed. This raises the need for a versatile and compact measurement system that is capable of performing measurement campaign while the insertion device is installed inside a vacuum chamber and in the beam line of a light source.

Currently, the Swiss Light Source SLS is undergoing a major upgrade to SLS2.0 where new undulators are being designed and manufactured to be operated in the new version of the machine. Historically, the light beams used in SwissFEL mainly utilise permanent magnets IVUs to produce the required X-rays. In SLS2.0, a new version of IVUs are in the design process where the attraction force between the magnetic arrays is mitigated significantly via the use of passive force compensation side magnets. The attraction forces between the magnetic elements of an undulator scales with the length of the device i.e. with how many magnets there are in the opposing arrays and with the distance between them or the gap. This requires a lot of rigidity and strength from the mechanical structure holding the magnetic arrays apart. With the new design of undulators, the introduced side magnets help reduce this mechanical load resulting in smaller and more compact devices. This can be beneficial in terms of size and production cost of insertion devices.

1.2 Project Overview

The commissioning time of IVUs in comparison to other types of undulators is significantly longer which negatively affects the time and effort required for periodic maintenance and the repairability of the device. This is due to lengthy installation process of the device where the undulator is firstly installed inside a narrow vacuum chamber, then the frame and supporting structure is fixed into place making it very difficult to reach the magnets to perform any measurements or optimisation on the insertion device.

Moreover, the new design could potentially have enormous benefits as it would reduce the attractive force between the undulator array by a factor of 8 or more, which allows for smaller more compact devices to be manufactured [3]. As a consequence of the compactness, the new design could potentially be much cheaper to manufacture which could be specifically beneficial in an upgrade of this size. However, the magnetic field from the side force compensation magnets interacts to an extent with the main undulator field and hence, this interference needs to be analysed and quantified.

In this dissertation, the new magnetic force compensation undulators are characterised using an improved version of the micro magnetic measurement bench. This type of undulator will be used for the first time at PSI as part of the SLS2.0 upgrade. The Micro Magnetic Measurement Bench (μ MMB) [4] was developed previously in a collaboration project between the Insertion Devices Group at PSI and the University of Malta. The magnetic acquisition system that interfaces to the bench was implemented by Cassar et al. as a joined project between SENIS AG, Insertion Devices Group at PSI, and the University of Malta.

1.3 Research Goals

The previously developed bench was a prototype and a proof of concept of the mechanical part of the bench. The prototype needs to be improved in terms of implementation, compactness, and ease of use. Once these aspects are improved, the bench is to be used to characterise the new prototype undulator for the SLS2.0 upgrade. The goals for this research are:

- Revise the previously designed bench, specifically the electrical and electronic aspects.
- Improve on the previously implemented system by upgrading to new hardware when applicable, improve the implementation of the bench in terms of physical footprint and add new hardware to perform any lack of functionality.

- Integrate all bench parts, including the 3-axes Teslameter, on a single Printed Circuit Board (PCB) that can move with the mechanical bench inside narrow spaces such as a vacuum chamber.
- Improve on the software implemented previously for smoother measurement process, improve user friendliness and better serviceability for commissioning and future upgrades.
- Improve the bench's overall ease of use by creating a wireless link between the on-board electronics and a PLC station with a Graphical User Interface (GUI). The GUI allows for the operation of the implemented measurement bench with minimal previous knowledge to the system components and makes it more versatile.
- Once the bench's performance is satisfactory, the measurement system as a whole is to be used to characterise the new prototype undulator design for the first time with force compensation magnets which is planned to be used in the upcoming SLS2.0 upgrade.

The prototype undulator introduces a new magnetic design where adjacent to the field enhancing magnets on both sides is another set of magnets that repels the opposite magnet arrays. This should reduce the attraction forces between the top and bottom magnet arrays and mitigate the mechanical deformations in the supporting frame of the undulator due to the stresses on the material due to the attraction force.

1.4 Dissertation Structure

This dissertation follows the improvement in the implementation of the previously prototyped μ MMB and then using it to characterise a new undulator prototype with force compensation magnets. The dissertation is divided as follows:

Chapter 2 is the literature review where a brief introduction to synchrotron radiation and the basic structure and composition of light sources based on that principle and the role of insertion devices in generating the x-rays in such facilities. Also, the importance of accurate and precise magnetic field measurement in light sources is highlighted. The introduction is followed by a brief history of magnetic measurement benches that were utilised to characterise insertion devices in light-source structures around the globe over recent years.

Chapter 3 is an overview of the μ MMB with the basic structure, the motivation and importance of the miniature mechanical design. The previously implemented bench is described in detail, limitations are highlighted, and improvements on

both the mechanical and electronic aspects of the bench are justified. Furthermore, the commissioning process is explained, and the tuning process and performance of the motion systems is presented in detail.

Chapter 4 details the different communication schemes between the different components and subsystems of the bench along with their hardware implementation and the different Printed Circuit Boards (PCBs) manufactured to integrate all the electronics components of the bench. The flow of the main software of the bench is briefly explained along with the dedicated sub-routines that allow the bench to perform the required tasks.

Chapter 5 briefly describes the measurement setup of the implemented bench which is to be used to characterise the aforementioned prototype undulator with force compensation magnets. This is followed by the test plan to benchmark the performance of the measurement system and characterise the prototype undulator and the effect of the side magnets on the field enhancing magnets. The performance of the implemented bench is also compared to the previous version and the 3-axes Teslameter as a stand-alone instrument.

Chapter 6 is a summary chapter where the results obtained from the testing phase are outlined and critical analysis of the implemented system. Future improvements to elevate the performance of the measurement system are highlighted and specific suggestions to further enhance the implemented magnetic measurement bench are listed.

Chapter 2

Literature Review

In this chapter, the working principles of light sources such as SwissFEL and SLS are briefly explained. Moreover, different magnetic measurement benches from similar institutes around the world are reviewed including the previous version of the bench and the new undulator prototype with force compensation magnets is briefly reviewed with highlights to the advantageous and drawbacks of such a concept.

2.1 Light Sources Working Principles

Light sources such as SwissFEL and SLS produce X-rays by synchrotron radiation. The light generated from synchronous radiation has high brilliance and high intensity when compared to other conventional methods of x-rays generation such as using x-ray tubes. In other terms, the generated X-rays are concentrated in a narrow spectral band and a small phase space volume with high magnitude in the frequency spectrum. Synchronous radiation facilities comprise of mainly an electron source, a linear accelerator, insertion devices, and experimental area. To generate X-rays, a linear accelerator pushes electrons from the electron source to near the speed of light, the accelerated electrons then pass-through magnetic fields from insertion devices and the accelerated electrons exhibit a force (Lorentz force) that is orthogonal to the direction of electron velocity and to the magnetic field which causes movement or in other term wiggles, along a certain trajectory. As a result of the wiggling, the electrons emit energy within the range of infrared to X-rays to be used in various applications in a controlled experimental area.

Figure 2.1 illustrates light generation when an electron e passes through a plane undulator, the path of the electron is represented by the black wiggling vector \vec{R} , the generated light is represented by the yellow cones and the undulator's vertical or y magnetic field B is represented by the red arrows.

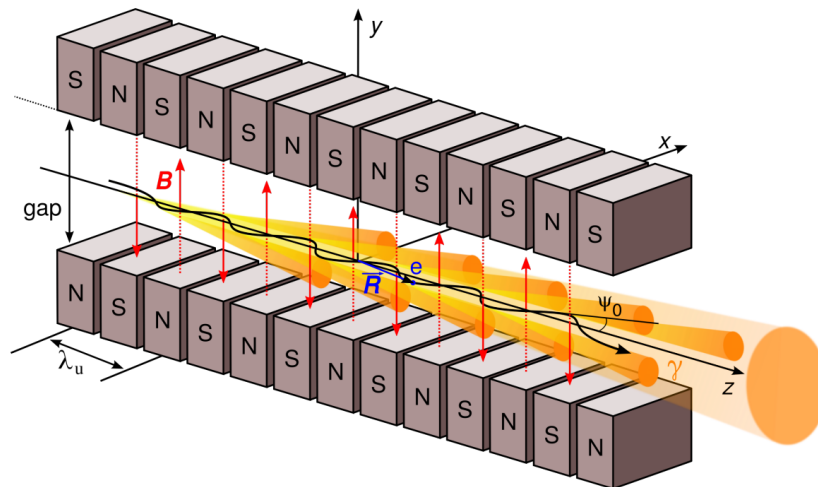


Figure 2.1: Functional Principles of Light Sources and Synchrotron Radiation - Specifically in a Plane Undulator [6]

Insertion devices consist of alternating magnetic elements to construct a planar magnetic field along the device's length. There are mainly two types of insertion devices which are wigglers and undulators, and the main difference between the two is that wigglers emit light over a broad spectrum that could span from visible light to X-rays at the same time while undulators emit monochromatic light plus few harmonics. A monochromatic light is defined within a very short range on the electromagnetic spectrum, making light generated by undulators more tunable with high brilliance.

This can also be explained in terms of coherence, in FEL devices, when electrons are accelerated, they are accelerated in bunches and every bunch leads the one behind by a distance of λ . This physical lead distance is important in generating coherent light as it allows the light produced from each electron bunch passing through an undulator to be superimposed in such a way that the generated light from each bunch additively supports each other. Figure 2.2 highlights the concept of electron or particle bunching and illustrates coherent light generation.

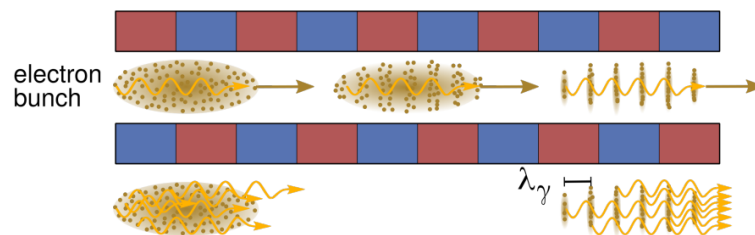


Figure 2.2: The Concept of Electron Bunching and Coherent Light Generation [6]

The generated light's wavelength is defined by Equation 2.1 which is also known as the fundamental undulator equation.

$$\lambda = \frac{\lambda_u}{2\gamma^2} \left(1 + \frac{K^2}{2}\right) \quad (2.1)$$

Where,

- λ is the wavelength of the generated light
- λ_u is the undulator period length
- γ is the relativistic Lorentz factor

The main parameter of an undulator is the K-Value or the undulator strength parameter. "The K-Value gives a measurement of the electron deflection angle when divided by the relativistic Lorentz factor γ " [7]. The K-Value is defined by Equation 2.2.

$$K = \frac{e}{2\pi \cdot m_{e,0} \cdot c} \lambda_u B_0 \quad (2.2)$$

Where,

- e is the charge of an electron
- $m_{e,0}$ is the mass of an electron at rest
- c is the speed of light
- B_0 is the amplitude of the magnetic field

By substituting the values for e , $m_{e,0}$ and c , Equation 2.2 can be simplified into Equation 2.3

$$K = \frac{1.602 \times 10^{-19}}{2\pi \times 9.109 \times 10^{-31} \times 3 \times 10^8} \lambda_u B_0$$

$$K \approx 93.302 \lambda_u|_{\text{in mm}} B_0|_{\text{in T}} \quad (2.3)$$

From Equations 2.1 and 2.3, it can be seen that the strength of the magnetic field is a key parameter to tune the undulator's strength or K-Value to generate a specific wavelength light since the period of the undulator is constant by design. Hence, an accurate measurement of the magnetic field is critical to allow for the operation of an undulator over a wide range of photons wavelengths.

The magnetic field strength of an undulator can be increased mainly in two ways, either by using stronger magnetic elements such as powerful permanent magnets and superconducting magnets or by decreasing the operational gap between the magnetic arrays of an undulator. Superconducting magnets allow for very high currents to run

through a superconductor which consequently creates a stronger magnetic field. On the other hand, a small operational gap in permanent magnets undulator yields a stronger magnetic field as well, however, at the cost of additional complexity of the measurement system and the mechanical supporting structure of the permanent magnets undulator.

Undulators operating with small gaps are usually In-Vacuum Undulators (IVUs) which means the magnetic arrays are installed inside a vacuum chamber and is sealed all around apart from the two ends of the chamber. Also, the attraction forces between the top and bottom magnets are enormous and need to be sufficiently supported by a strong mechanical frame to keep the arrays from contact which adds for the cost of production and significantly increase the size of the device. The attraction forces are also directly related to the length of the device i.e. the longer the device, the stronger the attraction forces are and the larger the size of the device is to be able to withstand such loads which can be in the range of dozens of tons. Figure 2.3 illustrates the operational gap of an undulator.

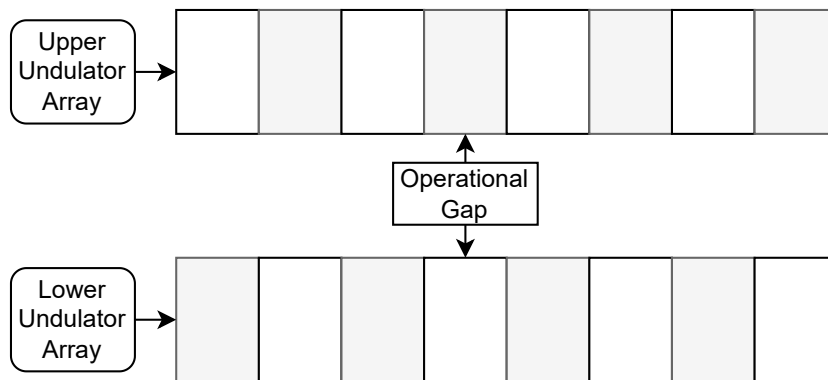


Figure 2.3: Operational Gap of an Undulator

Due to the space constraints introduced inherently by an IVU structure, the measurement of the magnetic field with high precision while the undulator is assembled, is a great challenge that requires innovative solutions to be achieved.

2.2 Measurement Benches

Measuring the magnetic field of an undulator is a critical task to tune the appropriate K-Value which is consequently responsible of generating the required light wavelength. It is also important to study the quality and the homogeneity of the magnets used to construct the undulator as the field profile is indicative of any alignment errors in the undulator composition such as magnets height, pitch and gap errors. Hence, measurement of the magnetic field profile is essential for the alignment and optimisation

procedures of the undulator.

The main concept of a measurement bench is to move a magnetic sensing element along an undulator's length in its spatial centre at a consistent velocity while keeping the sensing element at the spatial centre of the undulator. This is a very important aspect of measurement benches as the undulator's main magnetic field (Vertical magnetic field or B_y) is extremely sensitive to any variations, as small as tens of microns, in the vertical position of the sensing element. Therefore, stability is a highly desirable feature when measuring the magnetic field of an insertion device such as an undulator.

There are various ways to obtain magnetic field measurements that use different technologies such as stretched wire, pulsed wire systems for local measurements, stretched rotating rectangular coil and probably the most common is Hall probes. The choice depends on many factors such as the field strength of the measured device and the required accuracy of the measurement [8].

In the next section, several magnetic benches that were implemented in similar facilities to SLS and SwissFEL around the world to accomplish the task of precise magnetic field profiling are discussed.

2.2.1 Granite Slab Based Measurement Benches

The European Synchrotron Radiation Facility (ESRF) in France designed and implemented a magnetic measurement bench that incorporates both a Hall probe based measurement bench to measure the magnetic field profile and a stretched wire measurement apparatus to measure the field integrals along insertion devices. Figure 2.4 shows the measurement bench next to an undulator[9].



Figure 2.4: Granite Base Magnetic Measurement Bench at ESRF [9]

The Hall probe based measurement system is positioned on a granite slab of 4 meters and can be changed to 6 meters on demand. The slab is then mounted on vertically adjustable feet to ensure proper level of the slab's upper surface. This is required due to the natural deflection of long and heavy objects such as the equipped granite slab. The surface of the granite slab is accurately machined to achieve a surface flatness that is lower than $15\mu\text{m}$.

The upper surface is equipped with precision guide rails for a linear motor to traverse the Hall probe along the insertion device under measurement with parallelism of $15\mu\text{m} \pm 2\text{m}$ and the linear motor is also directly mounted on the slab. The linear motor of choice provides negligible magnetic interference to minimise any magnetic noise to be transferred to the Hall probe. A closed loop control system is implemented for the linear motor using an optical ruler (an optical encoder).

The main carriage of the linear motor mounted on the slab is equipped with two motor stages in the x and y directions for correct Hall probe positioning. Figure 2.5 shows the Hall probe bench under laser calibration.

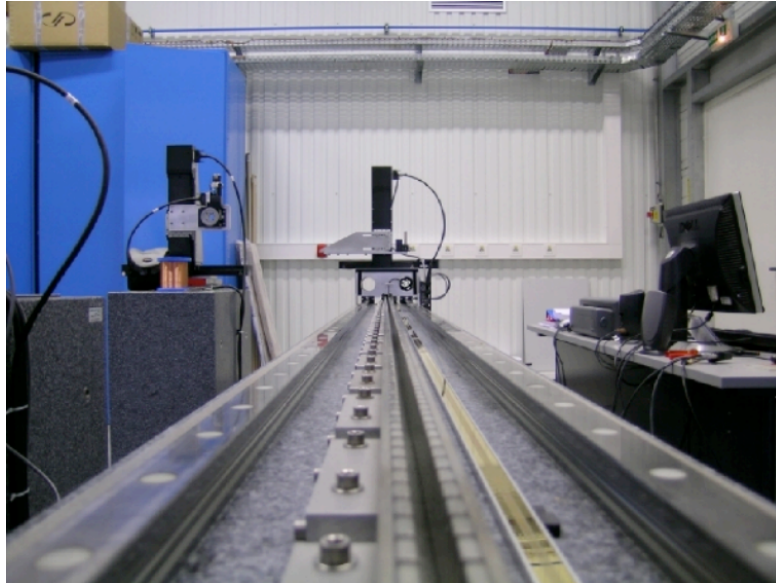


Figure 2.5: Hall Probe Bench Under Laser Calibration at ESRF [9]

The Hall probe is mounted on an aluminium plate that 0.5m long where each field component (x , y and z) from the Hall probe is interfaced to three voltmeters and is capable of performing measurements at a speed of 50 mm/s and up 100 mm/s.

The second part of the measurement bench is a stretched wire apparatus to measure the field integrals which are required in the optimisation procedure of an undulator. The stretched wire assembly is attached to the granite slab similar to the Hall probe bench and consists of two identical motorised stages that are fixed at both ends of the slab. Each stage consists of 3 motors that are in closed-loop control for correct alignment and is capable of measuring both the first and the second integrals of the magnetic field. The stretched wire apparatus attached to the granite slab is shown in Figure 2.6



Figure 2.6: One of the Motorised Stage for the Stretched Wire Field Integral Bench at ESRF [9]

The voltmeters, motor drives and power supplies are all integrated in a single cabinet that interfaces to a PC for the end-user to control all the different components of both the Hall probe and the stretched wire assemblies.

At PSI, a granite-based measurement system was implemented to conduct measurement campaign for SLS undulators and is currently located in the measurement laboratory of the Insertion Devices Group at PSI. Figure 2.7 shows the granite slab and Figure 2.8 shows the Hall probe holder and mover which is similar to that implemented at ESRF.



Figure 2.7: Granite Slab Used for SLS Measurement Bench at PSI [4]

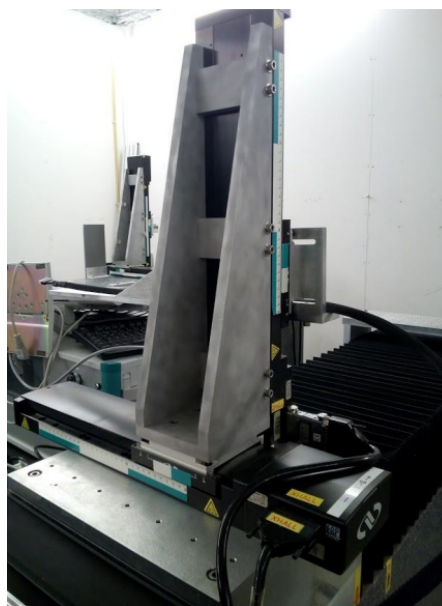


Figure 2.8: The Hall Probe Mover Assembly for The Granite Measurement Bench at PSI [4]

Granite slabs are used as stable surfaces due to the advancements in its manufacturing where the surface finish can be extremely flat with minimum pits to as low as a few microns. On the other hand, a major disadvantage is the size and weight of the granite slabs making it inconvenient to move the measurement bench to the location at which undulator is installed in order to perform any measurement campaigns.

As a consequence of the immobility of this approach, the undulator or the insertion device must first be assembled in a lab environment where the granite bench is located where magnetic measurement can be performed. Upon the completion of the magnetic

measurements, the undulator must be disassembled and transferred to its operating place.

This can introduce all sorts of issues that might occur during the disassembly and re-assembly process where some characteristics of the magnetic field might change drastically resulting in the measurement campaign to be nullified and in extreme cases, the campaign needs to be repeated going through all the aforementioned procedure.

Due to these issues, a more agile approach is needed to avoid such problems and save time and effort in the measuring and optimisation process of undulators.

2.2.2 The Magnetic Measurement System CASPER

Superconducting and cryogenic undulators are becoming more popular as stronger magnetic fields are desirable. A measurement setup was developed at the *Karlsruhe Institute of Technology* (KIT) [10] for the synchrotron *ANgströmquelle Karlsruhe* (ANKA) to measure a superconducting undulator at its operating temperature of 4 K with the ability to measure both the magnetic field via Hall probe sensor and the field integrals using a stretched wire setup. The measurement system is called (ChAracterization SetuP for field Error Reduction) or CASPER.

The superconducting magnets are installed inside a chamber that mimics cryogenic conditions (vacuum at extremely low temperature). The Hall probe sensor is mounted on a brass sledge that is guided by two guiding rails at both sides of the superconducting magnets while the sledge is driven along the undulator's gap via computer-controlled synchronised stepper motors at each end. The position and the direction of movement of the Hall probe and the brass sledge is determined to the nearest 1 μm via an interferometer. Stretched wire measurement is conducted in a similar way to the Hall probe measurement where a pair of stepper motors at each end of the undulator work synchronously to achieve field integral measurements.

Improvements were implemented to the CASPER system and a new measurement bench was implemented and is called CASPER II [11]. The new systems was commissioned using a 30 cm mock-up undulator and was deemed ready to characterise superconducting undulators that are up to 2 m in length since the system performed similar to room temperature systems at cryogenic conditions.

2.2.3 The ALBA Magnetic Measurement System

At the ALBA synchrotron light source in Barcelona, a new concept of a measurement bench was developed, and a prototype was implemented. The versatility of the prototype bench allows it to be used to measure multiple designs of large, closed structures, i.e. different IVU designs with different physical characteristics [12].

The concept is based on using a long stretched flexible tape with a Hall probe sensor attached to it and can be inserted from either ends of the closed insertion device and is then pushed to the other end like “threading a needle”. The tape’s material used in the implemented prototype is carbon fibre with a cross section of $16 \text{ mm} \times 1.6 \text{ mm}$ and the ends of the tape are attached to a C-shaped structure through a mechanism that allows for variable tension force on the tape and horizontal alignment of the Hall probe.

The C-shaped structure is made of aluminium and is based on a granite table and the whole structure can move back and forth on precision linear guides that are powered by computer controlled stepper motors. Figure 2.9 illustrates a 3-dimensional picture of the implemented bench.

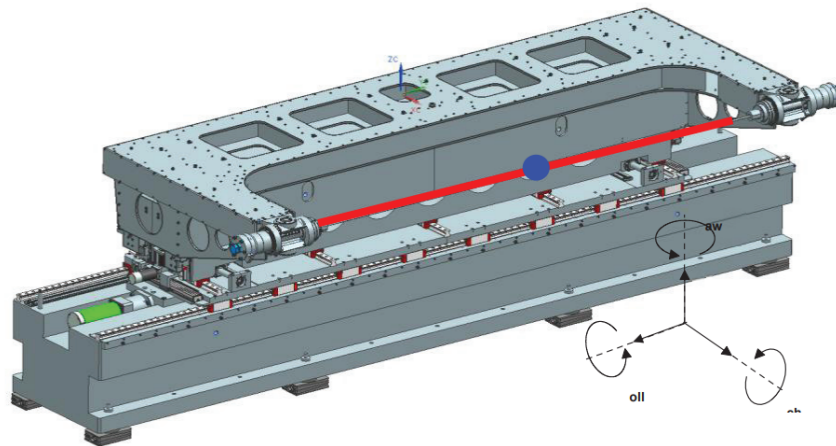


Figure 2.9: Hall Probe Bench Prototype Using a Stretched Tape (Red Line) and a Hall Probe (Blue Dot) [12]

The implemented prototype was able to achieve accurate magnetic field measurements while measuring closed magnetic structures such as IVUs. The design was considered feasible and performs according to the specifications. The prototype bench was used to characterise magnets at the *Centro de Investigaciones Energéticas, Medioambientales y Tecnológicas* (CIEMAT) in Madrid and the performance was comparable to a standard granite slab based system [13].

The main advantage of this design is its ability to measure IVUs on-site with high accuracy field mapping. However, multiple downsides can be listed for this approach such as the bulky design as the prototype uses a granite table as the supporting structure. Furthermore, the device under measurement needs to fit within the “C” aperture and its length must be less than one third of the “C” thus, making the designed bench specific to certain IVU lengths and difficult to transfer to a beam line tunnel to perform on-site magnetic field measurements.

2.2.4 SAFALI Based Measurement Bench

The SAFALI measurement system [14] previously mentioned is difficult to make compatible with multiple undulator designs as different undulator versions can vary in their physical attributes such as length, frame type and dimensions of the vacuum chamber. This is the main reason that such systems are implemented to cater for a specific version of IVUs.

Insertion devices, and particularly IVUs are compact, complex in their structure and usually are integrated with multiple sub-systems apart from the magnets such as hydraulic alignment systems. Commissioning and measuring IVUs with bulky measurement benches such as those based on a granite slab is inefficient time-wise and prone to errors due to the length of the process where the magnets needs to be measured and optimised close to the bulky bench, disassembled and transferred to their operating position, reassembled and finally installed inside the vacuum chamber in the beam line of operation. During these steps of transferring the magnets from the measurement facility to the operating beam line, the magnetic field quality of the undulator is not guaranteed to remain at a similar level to the measured state.

This is one of the limitations to IVUs in comparison to out-of-vacuum undulators and in an effort to address this issue, two measurement benches were designed and implemented on a concept that was developed in RIKEN SPring-8 Center (RSC) Japan to characterise an IVU and a Cryogenic Permanent Magnets Undulator (CPMU) [14]. The developed magnetic measurement systems are based on a Hall probe and are capable of conducting measurement campaigns inside vacuum chambers while actively stabilising the Hall probe sensor position using optical laser beams. The measurement systems are referred to as the Self-Aligned Field Analyser with Laser Instrumentation (SAFALI).

The SAFALI systems were used to measure two undulators, one is an IVU that is installed in SLS at PSI and was operated for approximately three years and the other is a CPMU to demonstrate the concept of CPMUs. The formerly mentioned IVU was measured to study the effect of radiation to the magnets during operation and the latter was measured to quantify the variations in the magnetic properties of the permanent magnets due to the low operating temperature in a cryogenic environment.

Measurement benches rely significantly on the manufacturing accuracy and low tolerances of mechanical components such as the guiding rails and the base tables to minimise deviations in the sensor's position from the spatial centre of the insertion device under measurement. However, due to pitching, rolling and yawing of the actuation table, the sensor's position can deviate from the spatial centre of the insertion device when the probe is travelling along the guiding rails. These fluctuations

can drastically impact the accuracy and repeatability of the measurement and must be kept as low as possible.

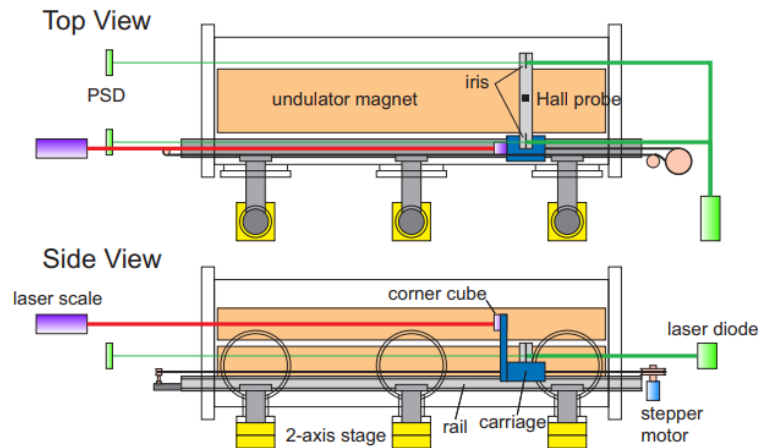


Figure 2.10: Schematic Illustration of the SAFALI System [14]

Figure 2.10 illustrates the SAFALI measurement bench developed and highlights the basis of performing magnetic measurement for IVUs. The Hall probe is attached on a cantilever and is connected to a carriage that travels along the undulator via tensioned loop wire through a stepper motor. A cubic mirror is also attached to the carriage to reflect a laser scale to determine the longitudinal position of the Hall probe.

Two irises are attached to the Hall probe cantilever at both ends with a diameter of 2 mm. With two laser beams installed on one side of the undulator and Position Sensitive Detectors (PSDs), the transverse position of the Hall probe can be determined. The laser beams are aligned with the irises on the Hall probe cantilever such that a portion of the laser beam passes through, and the incident light is then detected by the two PSDs. The average position of the incident light detected by the PSDs defines the position of the Hall probe. The position feedback is then used to actively correct the Hall probe position via the three sets of 2-axis stages which in hand move the rail accordingly to maintain the probe at the spatial centre of the device under measurement. Figure 2.11 shows the effectiveness of the active correction loop where the error of the transverse position in the x and y axes is significantly minimised to within $5 \mu\text{m}$ of the undulator centre when compared to a probe without the correction loop.

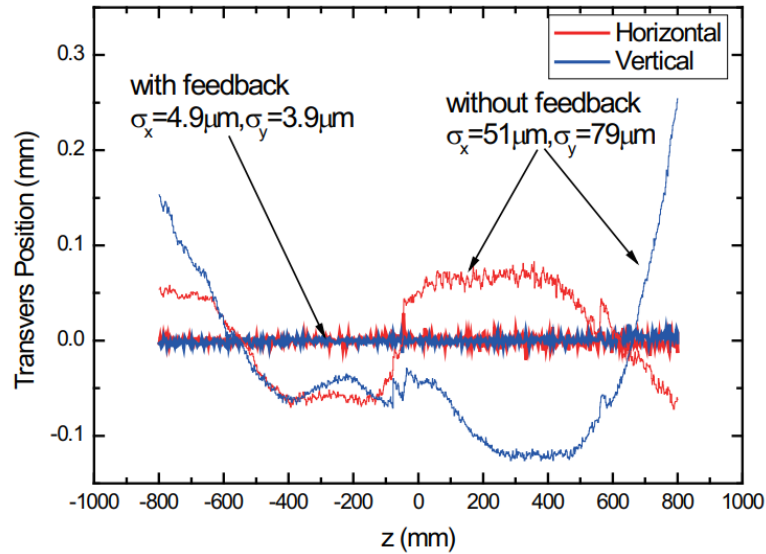


Figure 2.11: The Hall probe Position with and Without Position Correction [14]

The other bench was developed based on the previously mentioned IVU bench; however, it caters for conducting magnetic measurement in cryogenic conditions for a CPMU. The stepper motor that drives the carriage is swapped with one that is capable of operating within vacuum conditions. The Hall probe's position is corrected in a similar manner using three sets of 2-axis stages connected to the guiding rails, however, the position correction of the Hall probe performed worse in comparison to that in the above mentioned IVU bench.

The SAFALI system solves multiple issues by being portable and its ability to conduct magnetic measurements on the site where the IVU is installed in beam line tunnels without the need to transfer the IVU to a specialised measurement lab. This is especially beneficial in X-ray Free Electron Laser (FEL) facilities where multiple undulators are installed and each undulator require final magnetic field check after the assembly process. The ability to measure in the beam line tunnel is referred to as “*In-Situ*” undulator field measurement.

2.2.5 Magnetic Measurement Benches at PSI

Over the years, PSI has designed and deployed multiple types of undulators in SLS and SwissFEL such as the granite-based measurement bench previously mentioned in Section 2.2.1. The commissioning and optimisation stages of such devices required robust magnetic measurement benches to ensure correct field mapping. Examples of measurement benches used previously at PSI are discussed in this section.

2.2.5.1 Measurement Benches for the ARAMIS Undulators

The ARAMIS beam line is the hard x-ray beam that can generate x-rays in the range between 0.1 and 0.7nm and is constructed from 13 identical planar permanent magnets undulators. The permanent magnets arrays for each of the 13 undulators have a unique feature that allows for the individual magnets in each array to be height adjustable by $\pm 30 \mu\text{m}$ via a flexor that is moved by a wedge driven by a screw mounted to the lower side of each magnet [7]. This allows for the optimisation process to be automated by an integrating solution in the measurement bench. A sample of the magnetic arrays for the ARAMIS undulators with the wedge screw system is shown in Figure 2.12.

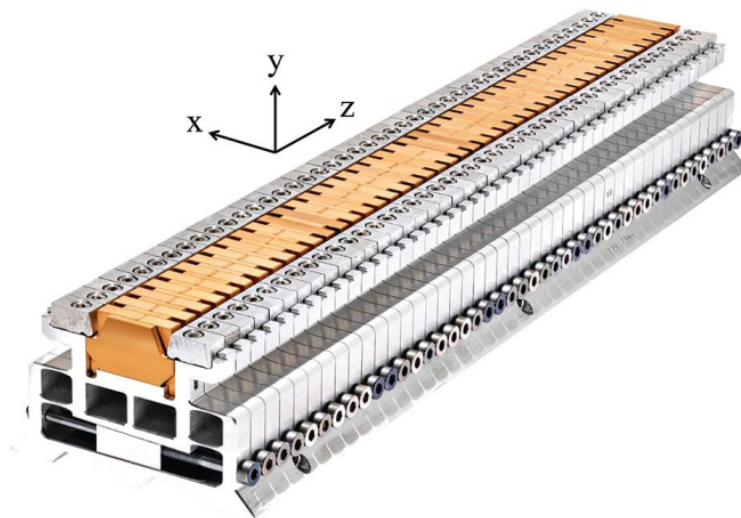


Figure 2.12: The Structure of a Magnetic Array Used in the ARAMIS Undulators with the Screw Driven Wedge Flexors [7]

Two measurement benches were designed and implemented to characterise and optimise the ARAMIS undulators with the novel automated optimisation process. Bench A handles the optimisation process via the use of a tuning robot that interfaces with the height adjustment screw for each magnet and is able to carry out the field corrections according to an optimisation algorithm calculated from the magnetic field measurement. The downside of the automated optimisation process is that the robot cannot reach the magnets when the undulator is installed inside the vacuum chamber, hence, Bench B was implemented to measure the magnetic field once the vacuum components are assembled around the undulators.

Both benches are based on a magnetic data acquisition system designed by SENIS specifically for the SwissFEL project and is coupled with “Hall probe S” which are available in the SENIS catalogue [15]. Since the data acquisition system has an analogue output, the transduced voltage is interfaced to an ADC card connected to a

Beckhoff PLC through a real-time EtherCAT bus. The position of the Hall probe is collected from an encoder interfaced to the same PLC system.

Bench A is composed of a linear motor that displaces both the measuring head and the tuning robot along the length of the undulator. The Hall probe, the SENIS transducer and the ADC cards are attached to the measuring head to minimise cabling length and minimise the effect of noise from lengthy connections. The measuring head is equipped with motors to correct the probe position through a SAFALI feedback system.

The tuning robot consists of a motorised screwdriver that interfaces with the magnets height adjustment hex screw and is able to perform corrections to both the upper and the lower magnet arrays of the undulator.

Bench B is to be used for field measurement when the vacuum components are assembled around the undulator. The space constraints of the vacuum chamber required the use of a different linear motor from Bench A which is a piezo motor that is small enough to fit inside the chamber. The probe stabilisation system was also adjusted due to the size limitations where a new set of motors are mounted at six points along the guiding rails and the correction is performed by moving the rails instead of the measuring head itself. The ADCs are also mounted outside the chamber and the magnetic field signals were transferred via long cable.

The measurement speed for both benches is 10mm/s along the undulator, and the probe position stabilisation is achieved through a SAFALI system similar to the one implemented by Tanaka et al. [14] that actively corrects the probe's x, y axes and pitch angle. Figure 2.13 shows a simplified block diagram of the measurement benches A.

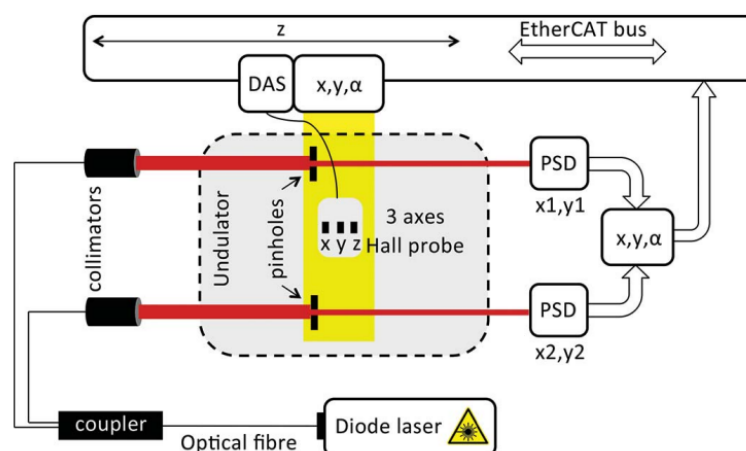


Figure 2.13: Simplified Block Diagram of Bench A for the ARAMIS Undulators [7]

A slight difference in the reproducibility of the field measurement between Bench A and Bench B was found which was attributed to disturbances in the laser beam that provides position feedback of the probe position. The laser beam errors are mainly due to two sources which are the laser pointing stability and the air turbulences in the measurement site. Given that Bench A performs measurements outside the vacuum chamber, the laser has more disturbance sources when compared to Bench B which performs measurement inside the vacuum chamber. This highlights the main limitation for the SAFALI based measurement systems which is the pointing stability of the laser beams as any physical jitter in the beams is directly translated to noise in the feedback signal.

The ARAMIS benches divided the characterisation and the optimisation processed by measuring and optimising the undulators outside the vacuum chamber using Bench A, and confirmed no major disturbances to the magnetic field quality from the vacuum component's assembly using Bench B. This can be greatly beneficial as Bench A automates the optimisation process through the height adjustment system implemented in the magnetic arrays and the time needed for such a process is significantly reduced.

2.2.5.2 Micro Magnetic Measurement Bench

Given the promising results and the excellent performance obtained from the ARAMIS benches, a new magnetic measurement bench was developed at PSI that combines the tasks of both the ARAMIS benches into one compact solution. The main aspect of the new bench is the novel miniature design based on a Hall probe paired with a novel reduced form factor, high accuracy, three-axis Teslameter [5], which allows for magnetic field measurement and magnetic pole optimisation for IVUs while the device is assembled inside a vacuum chamber, however, not in vacuum conditions. The miniature bench is hence called the Micro Magnetic Measurement Bench (μ MMB) [4].

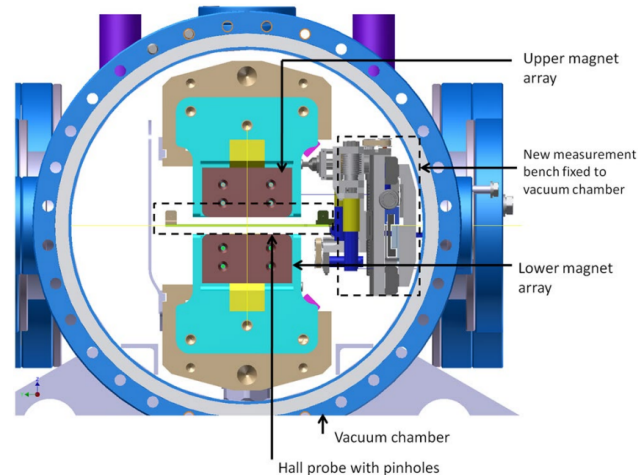


Figure 2.14: 3D Render of the μ MMB Assembled Inside a Vacuum Chamber [4]

The mechanical design of the bench can be divided into two parts:

Probe Stabilisation System Traversing the length of an undulator is prone to errors due to many factors such as tolerance errors in the guides or initial misalignment between the measurement bench and the undulator. To reduce the effect of such as controllable errors from the manufacturing process, a miniature probe stabilisation system was implemented based on the SAFALI system that can correct the Hall probe position in three different degrees of freedom (DOF). The correction axes are actuated using miniature BrushLess Direct Current (BLDC) motors paired with small form factor motor drives both from Faulhaber.

Magnetic Field Adjustment System As mentioned previously, the design of the magnet arrays of the ARAMIS undulators incorporates a magnet height control system that is operated via hex screw and can move each individual magnet by a distance of $\pm 30\mu\text{m}$, however, a separate bench with a tuning robot was needed to access these screws. The μ MMB incorporates this feature on the same bench via two motorised hex screwdrivers assembly one for each magnets array of the undulator. The screwdriver is engaged and rotated also via the same miniature BLDC motors and motor drives pair from Faulhaber.

Figure 2.15 shows the implemented μ MMB with its two main parts highlighted, and Figure 2.14 shows a 3D render of the bench assembled inside a vacuum chamber.

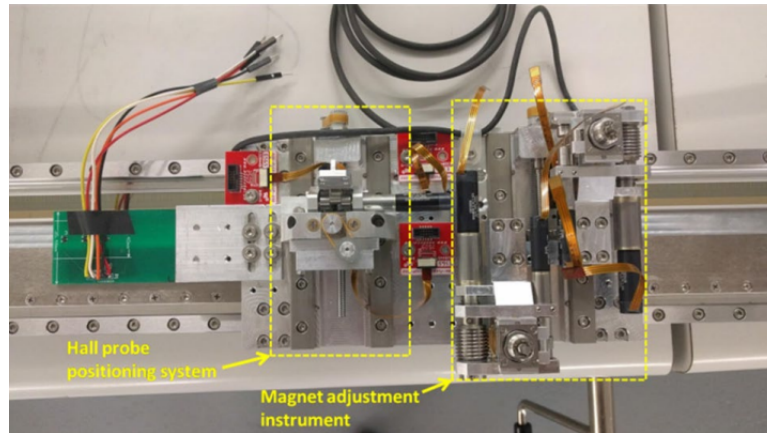


Figure 2.15: μ MMB for IVUs [4]

The bench travels along the undulator's length on rails installed inside the vacuum chamber via an ultra low-profile BLDC linear motor paired with the same controller used for the rotary motors in the probe stabilisation and the magnetic field adjustment systems. The reduced form factor Teslameter is interfaced to a Hall probe and handles the magnetic data acquisition with high accuracy and repeatability. The lateral position of the Hall probe is acquired from a high precision Heidenhain absolute linear encoder.

All the bench components are controlled by a Raspberry Pi single board computer which with some complementary electronics connects all the motors and the Teslameter for a user to operate the bench and performs measurements from a PC station situated conveniently close to the undulator being measured.

The micro magnetic measurement bench prototype showed promising results throughout the assessment campaign when compared to previously implemented benches at PSI with a field reproducibility of 0.09%. However, the prototype was not fully developed and tested for the magnetic field adjustment system which leaves room for improvements. This dissertation is a continuation of work on the micro magnetic measurement bench and the previously implemented prototype is described in detail in Chapters 3 and 4.

2.3 New SLS2.0 Undulator Prototype

PSI operates two light sources which are SLS and SwissFEL, both facilities have adapted different undulators designs over the years of operation. A major upgrade to the SLS facility is underway and new insertion devices are needed to improve the facility and achieve the new operation specifications.

Undulators in general are large and heavy structures due to the required stability and specifically the enormous physical stresses that must be withstood from the attraction

force between the facing magnets. These forces are particularly larger when operating in small gaps in the mm range. Furthermore, the attraction force scales with the length of the device since more magnets will be used in a longer undulator.

The new design for IVUs introduces opposing side magnets adjacent to the main undulator magnets that repel each other in order to reduce the attraction forces from the main undulator magnets. Theoretically, the repulsion from the force compensation magnets can completely cancel the attraction force from the main undulator field magnets which reduces the physical stiffness requirement for the undulator's supporting mechanical structure. This allows for small and compact undulators to be designed which reduces the manufacturing costs by using less materials and increases the mobility of the device. Also, due to the convenient size, more devices can be fit in the beam lines of a light sources.

On the other hand, the magnetic design phase of undulators is more complex due to the additional force compensation magnets which arises the need for complex models and consequently longer and computationally demanding simulations. Although the financial benefits are apparent, introducing force compensation magnets might potentially interfere with the undulator's main magnetic field magnets and may affect the strength and homogeneity of the magnetic field. Hence, this effect must be studied and characterised for a better understanding of the new undulator prototype.

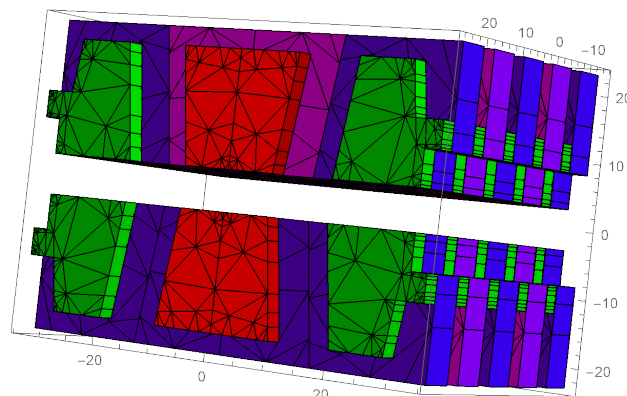


Figure 2.16: The RADIA Model of the New Undulator Magnets with Force Compensation Side Magnets [16]

Figure 2.16 shows a mathematical model of the magnets with force compensation side magnets using a simulation tool called RADIA [17] where the permanent magnets are in blue and purple to distinguish the two different magnetisation directions while the iron poles are in red and green to distinguish between the ones which enhance the undulator field and the ones which compensate the forces respectively.

The stiffness required to produce an accurate magnetic field is provided by the vacuum chamber itself. The chamber is produced from a single block of aluminium

with guiding rails for a measurement bench and upper and lower I-Beams for the permanent magnets undulator which is unlike other designs where the physical strength is provided by an external frame.

The chamber is 500mm long and the desired length of the undulator is achieved by joining multiple 500mm segments one after the other. The modular aspect allows for the same magnetic design to produce multiple undulators for different needs and different lengths according to the space available in the storage ring of SLS2.0. Figure 2.17 shows a segment of the modular vacuum chamber frame for SLS2.0 IVUs.

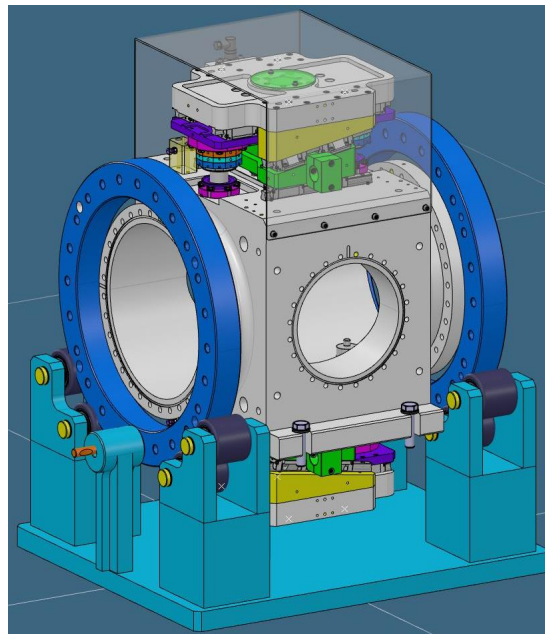


Figure 2.17: The Undulator Vacuum Chamber Unit with Attached Gap Drive System [16]

The concept of magnetic force compensation in IVUs was previously implemented by [Kinjo et al.](#) by building a proof of concept prototype for a Lightweight Compact Variable Gap Undulator (LCVGU) [18]. The implemented prototype showed promising results in magnetic field quality and the mechanical stresses reduction on the supporting frame. Figure 2.18 shows the attractive magnetic force between the magnetic arrays of the prototype with and without the force compensation magnets.

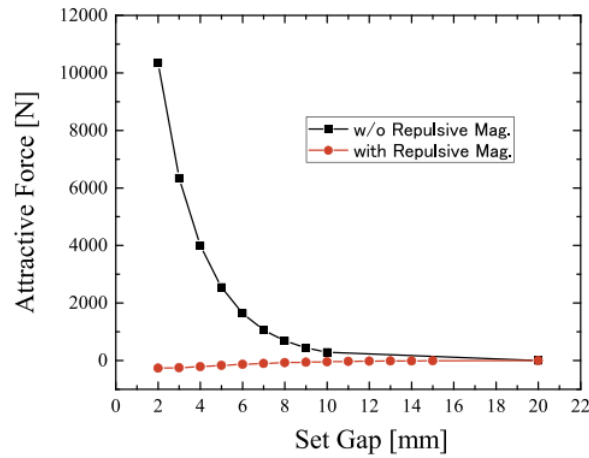


Figure 2.18: The Attractive Magnetic Force Between Undulator Arrays with and Without Force Compensation Magnets [18]

The implemented prototype realised the concept of magnetic force compensation, this reduces the complexity of the mechanical design for variable gap IVUs and consequently, reduces cost and time for constructing undulators. Also, the magnetic field quality was shown to be comparable to conventional IVUs which further ensures the validity, effectiveness and allows for more lightweight compact undulators design for space constrained facilities.

The force compensation concept was implemented on different undulator designs where a new device was implemented in The Shanghai High Repetition Rate XFEL and Extreme Light Facility (SHINE) with APPLE III undulator structure [19]. The APPLE III undulator design is an out-of-vacuum device and consists of 4 magnetic array that are installed 45° apart from each other. The required magnetic field is then controlled through a combination of phasing the magnetic arrays and varying the operational gap. Figure 2.19 illustrates the structure of the implemented APPLE III undulator.

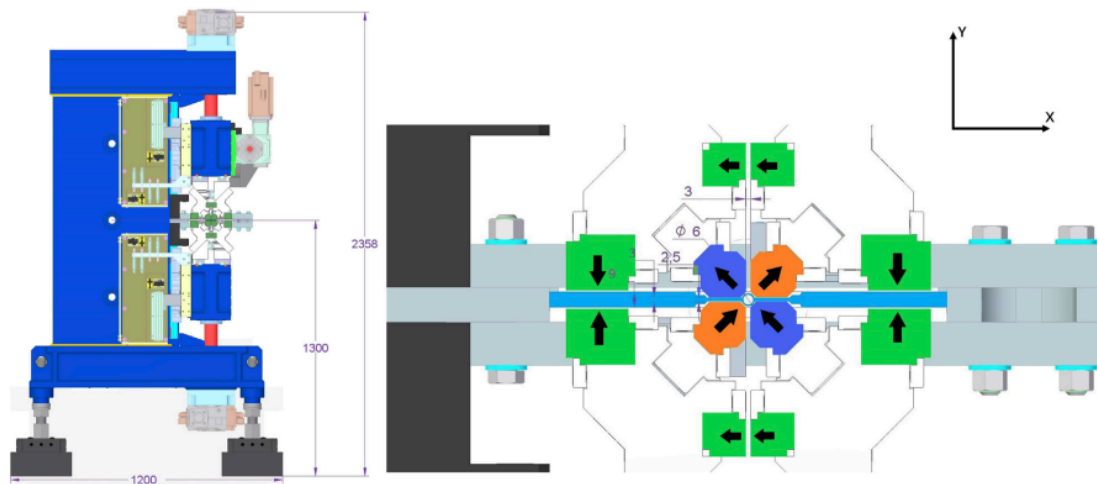


Figure 2.19: The undulator consists of four FM arrays (orange and blue) and eight CM arrays (green) [19]

2.4 Literature Review Conclusion

The literature reviewed in this chapter presented a brief introduction to synchrotron radiation and the basic structure and composition of light sources based on that principle. The role of insertion devices in generating the x-rays in such facilities was also explained and the importance of accurate magnetic field from undulators as a key feature for proper operation was clarified.

Furthermore, several magnetic measurement benches technologies that were used in light sources facilities over the years were mentioned starting from the early benches with heavy and bulky structure similar to the ones based on granite slabs to the light more compact measurement systems such as SAFALI based benches.

Most of the mentioned measurement systems were not equipped with the ability to measure multiple undulators using the same hardware and the field of magnetic measurement for insertion devices requires further development in that manner to implement a universal system with the ability to measure closed structure such as IVUs without the need of transporting them to an equipped lab.

Magnetic benches that are based on the SAFALI system are more compact and easier to deploy for measurement albeit being mostly implemented to only measure specific undulators with no ability to optimise the magnetic field while the insertion device is commissioned in the beam line. The automated procedure with the robot is a fascinating and very attractive option for many facilities, however it will take time, because the magnet structure must be adapted appropriately with the specific block-keeper design.

In addition, a new undulator design is under test as part of SLS2.0 at PSI upgrade where the concept of force compensation using side magnets was listed along with

the advantageous, disadvantageous and the extra complications that need to be considered during the design phase.

The μ MMB prototype which was previously developed [4] is based on the SAFALI system and was designed with the ability to carry out both magnetic measurement and optimisation while an IVU is located in the beam line. The bench was mechanically designed to cater for measuring insertion devices of various lengths due to a modular approach in the linear movement stage which is discussed in detail in Chapter 3. The prototype showed promising results and required further improvements in its implementation such that all components can fit inside a vacuum chamber and travel freely along the IVU's length. The work presented in this dissertation is based on the implemented prototype with some improvements and using the improved version to characterise the new undulator prototype.

Chapter 3

Bench Overview & Motion Controls

In this chapter, the mechanical aspects of the μ MMB are explained along with the motion mechanisms for the different parts of the bench. The limitations of the implemented system are highlighted, and the improvements performed to the mechanics to address these problems are discussed. Furthermore, the commissioning procedure for the bench was performed and the motion systems were tested and tuned given that the bench prototype has not been utilised in the recent 4 years.

The measurement system is required to meet the following criteria:

- Perform magnetic measurements at a speed of 10 mm/s.
- The magnetic measurement maximum absolute error must be similar to the previous measurement system or better. i.e. the maximum error must be $\leq 0.37\%$.
- The position of the Hall probe sensor must be ≤ 20 mm from the center of the insetion device. Hence, the Hall probe sensor position must be actively corrected during magnetic measurements at a rate of ≥ 10 Hz which corresponds to ≥ 10 position corrections for every mm travelled.
- All subsystems of the measurement bench must travel freely inside a narrow vacuum chamber along the mechanical bench without physical interfering with the undulator inside.

3.1 Overview of the Implemented Mechanical Bench

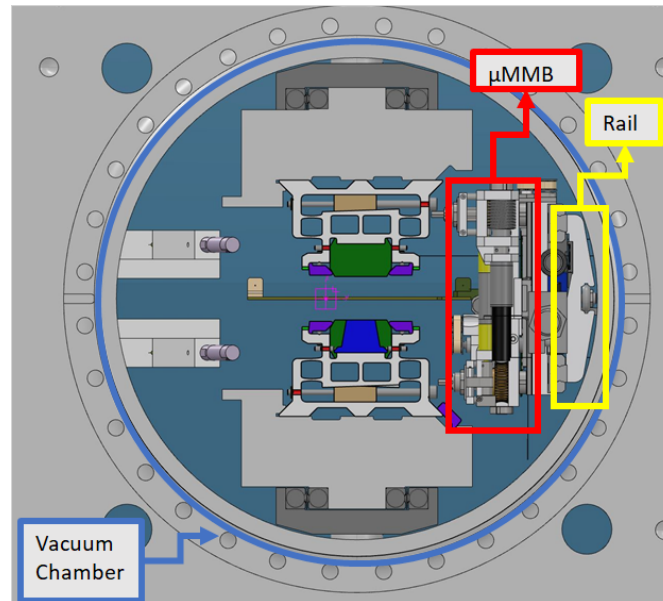


Figure 3.1: The μ MMB Fitted Inside a Segment of The Designated Vacuum Chamber

The bench consists of an aluminium base plate that slides along a linear aluminium rail via low friction linear bearings, and the rail is fitted to a slot that is built into the structure of the vacuum chamber. Figure 3.1 is a 3D model of the μ MMB (in red marking) attached to the mentioned rail (in yellow marking) and fitted inside the designated vacuum chamber (in blue marking).

Attached to the base plate is the main two mechanical subsystems of the bench which are the Hall probe positioning system and the magnetic pole adjustment system. The base plate assembled with the two subsystems is translated along the insertion device via a low-profile modular BLDC linear motor which allows the bench to be used in measuring insertion devices with different lengths. A 3D model of the two components is as shown in Figure 3.2.

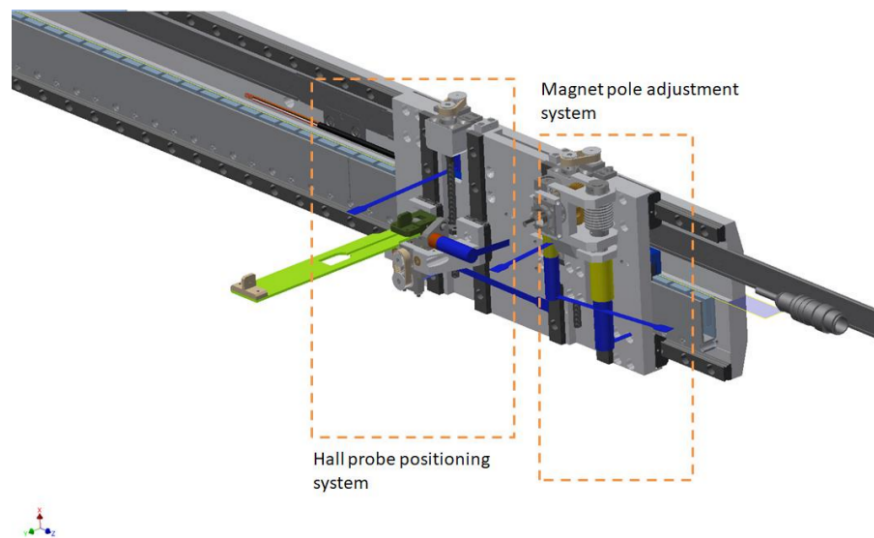


Figure 3.2: A 3D Model of the μ MMB the Two Main Components Highlighted [4]

3.1.1 Hall Probe Positioning System

The quality of the measured magnetic field from an undulator is dependent on many factors when using a Hall probe. Many of the factors are compensated electronically and through software calibration from the magnetic acquisition system, however, the physical stability of the probe is desirable to cater for magnetic field variations due to the position of the sensor with respect to the spatial centre of an undulator. The probe positioning system ensures that magnetic field errors caused by the probe position are minimised. This is done by performing active correction to the position of the sensor during measurement i.e. while the probe is moving along an undulator. The μ MMB's probe positioning system is equipped with 3 Degrees of adjustment (DOA) to adjust the sensor's position in the horizontal, vertical and the roll angle. The movement is performed by using BLDC mini motors from Faulhaber [20], the chosen motors are integrated in the design of the bench by the mechanical design team for the Insertion Devices Group at PSI and are held in place via circular slot and a set screw. Given the limited space available for motors on the bench, the choice of using these mini motors was primarily due to their compact size and the integrated single-turn absolute rotary encoder to keep track of the shaft position. The rotary movement is then transferred to the horizontal and vertical via combination of a reduction gearbox, two rotary gears and tension belt and lastly a ball-screw. As for the roll angle, a reduction gearbox and a rotary link translates the rotations of the angle correction motor to linear movement on the Hall probe holder. Figure 3.3 shows a 3D model of the horizontal, vertical and the roll angle correction DOA.

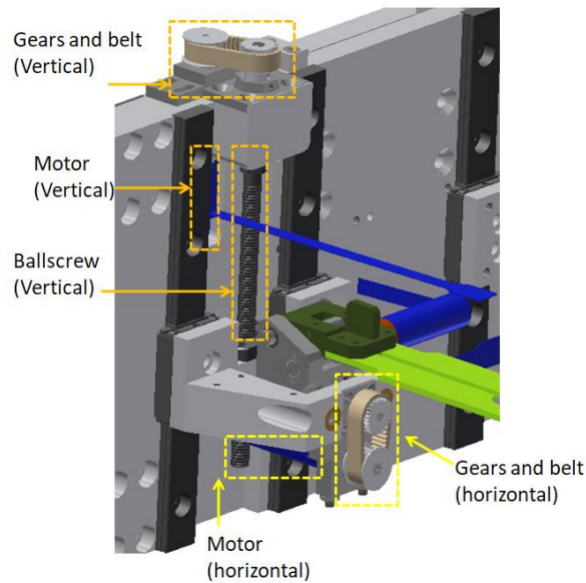


Figure 3.3: A 3D Model of the Hall Probe Positioning System [4]

To perform position correction to the Hall probe, a position feedback loop was implemented according to the SAFALI system presented in Chapter 2. Hence, the probe position is obtained from a pair of two lasers and two Position Sensitive Diodes (PSDs). The light beam from the lasers passes through 2 pinholes attached to the Hall probe holder and a spot of incident light is then detected by the PSDs. This gives an accurate indication of the probe position to calculate the errors and perform correction.

The horizontal and vertical drive systems of the probe positioning system utilise similar components with different parameters. A basic sketch of those systems is shown in Figures 3.4 and 3.5. Therefore, the relationship between the shaft rotation and the linear movement of the probe holder can be derived as follows.

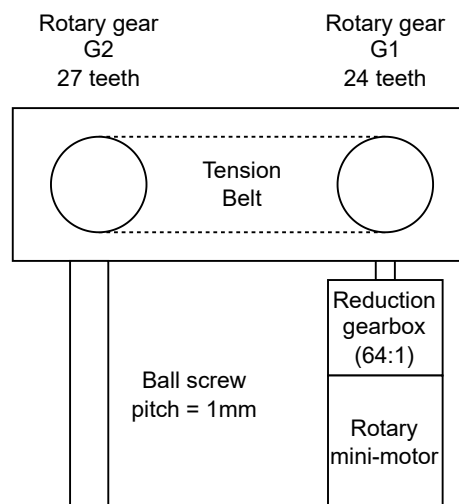


Figure 3.4: A Sketch of the Vertical Drive of the Probe Positioning System

For the vertical drive system sketch in Figure 3.4, the motor's shaft rotation is transferred to the gear G1 through a reduction gearbox of 64:1 ratio. The rotation is then transferred to the gear G2 which is connected rigidly to a ball screw with 1mm pitch. Given that the motor is equipped with an absolute encoder that provides 4096 increments per revolution, the relationship between the motor shaft rotation and the resultant linear displacement is given by Equation 3.1.

$$4096 \times 64 \times \frac{27}{24} \times 1 = 294912 \text{ increments/mm} \quad (3.1)$$

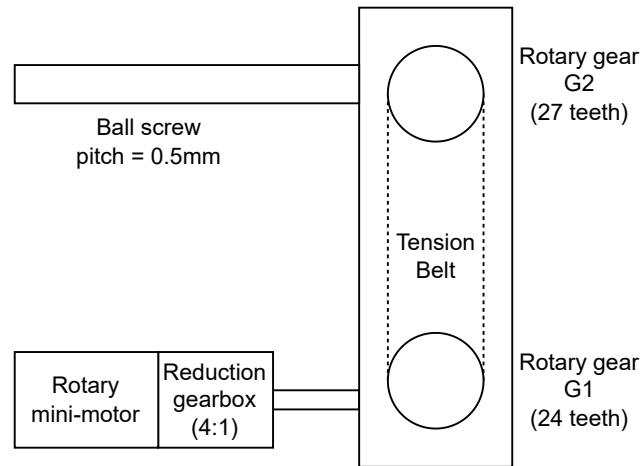


Figure 3.5: A Sketch of the Horizontal Drive of the Probe Positioning System

The horizontal drive system has the same mechanical components, however, with a different gearbox ratio of 4:1 and a ball screw with 0.5mm pitch. Similarly for the horizontal drive system the relationship is given by Equation 3.2.

$$4096 \times 4 \times \frac{27}{24} \times 0.5 = 9216 \text{ increments/mm} \quad (3.2)$$

The values obtained from Equations 3.1 and 3.2 are later used to translate the correction values of the probe position from mm to shaft rotations.

3.1.2 Magnetic Pole Adjustment System

The confidence obtained from the ARAMIS measurement bench with the tuning robot encouraged the development of the same concept on a smaller scale. The second subsystem of the μ MMB is the magnetic pole adjustment system which allows for height adjustments of individual magnets on the magnetic array that have this feature implemented such as the ones used in the ARAMIS undulators [7].

The adjustment is performed via two motorised screwdrivers that are based on the same BLDC mini motors family which allows for pole adjustment of both top and bottom array magnets simultaneously. The motorised screwdrivers assembly can

move vertically up and down to locate the height adjustment hex screw, and can engage and rotate each screw drive separately by using dedicated motors for each screw driver stage. The rotary movement of the engagement and the vertical stages is transferred from the motor shafts via the same setup used in the Probe positioning system for the horizontal and vertical degrees of adjustment. Figure 3.6 illustrates a 3D model of the designed magnetic pole adjustment system.

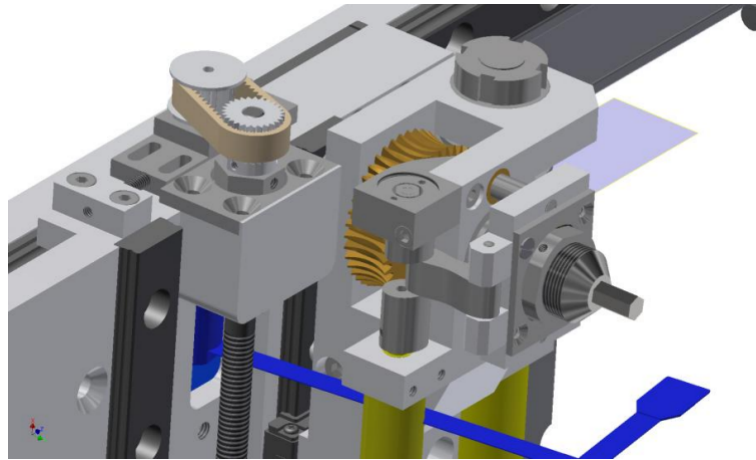


Figure 3.6: A 3D Model of the Magnetic Pole Adjustment System] [4]

3.1.3 Limitations of the Previously Implemented Mechanical System

The implemented μ MMB shown in Figure 3.7 achieved excellent performance in comparison to other benches used at PSI for magnetic measurement. The previous measurement system maximum absolute error was quantified to be 0.37

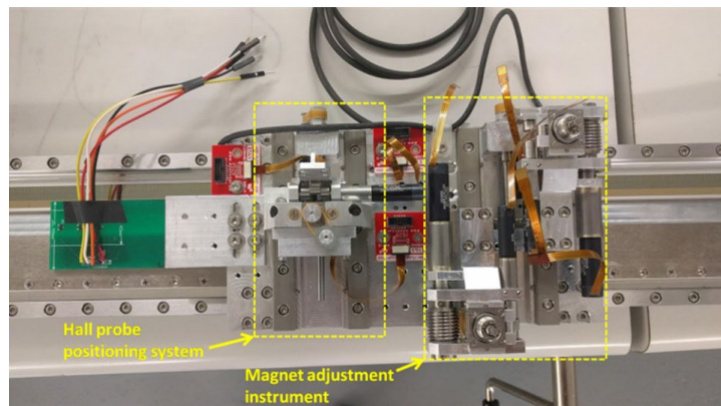


Figure 3.7: The Previously Implemented Mechanical μ MMB [4]

During the testing phase of the bench, the mechanical aspects were found to be weak and significantly limited the Hall probe positioning system [4]. The Hall probe holder is directly connected to the angle correction motor through a mechanical stage, the holder is then connected to a small plate that is part of the vertical and the horizontal correction stages. The holder was unable to support the weight of the

Hall probe lever and rendered the roll angle correction stage unusable. A quick fix to continue the testing phase was to fix the angle stage rigidly to the small platform such that the weight of the probe can be supported properly, however, this affected the horizontal correction stage as well and testing had to be carried out with only the vertical correction stage.

Furthermore, the magnetic pole adjustment system was not fully tested due to the lack of compatible undulator setup with an incorporated magnets height adjustment system. Therefore, the testing of this part of the bench was limited to preliminary tests of the driving motors and communication.

In addition, the mechanical bench and the electronics required for control were never tested inside an actual vacuum chamber to test the physical fit of the implemented bench in a narrow environment and its ability to perform the required tasks. This was also due to the absence of a suitable setup of an IVU for testing purposes.

3.2 Overview of the Previously Implemented Electronic System

The probe positioning system is based on the SAFALI system and is realised by utilising a laser source with an optical splitter to produce two laser beams. The laser beams are then aligned with two pinholes that are attached to the Hall probe holder to allow for narrower light beam to pass through. On the opposite side from the laser sources apparatus, two Position Sensitive Diodes (PSDs) that are used to detect the incident light position. The position of incident light is indicative of the Hall probe position and can be corrected accordingly. A similar system was previously used at PSI for the ARAMIS undulators optimisation procedures which proved to be a well-established and robust system.

Each PSDs outputs two data lines in analogue form for the horizontal and the vertical position of the incident light, the analogue data lines are connected to an Analogue to Digital Converter (ADC) Beckhoff PLC card which is connected to a Beckhoff PLC that applies a digital filter and outputs the position errors in the horizontal, vertical positions and the roll angle.

The 3 correction values are then transmitted to the main controller on the located next to the mechanical bench which is a Raspberry Pi Zero through a point-to-point ZigBee wireless link [21]. The Zigbee protocol provides robust wireless link for sensor data to be transmitted securely and is less prone for connection interruptions as is the case with basic wi-fi. It is also easy to integrate in such a system since it provides the ability to communicate with various devices using simple communication protocols such as serial in this case.

The correction received from the Beckhoff PLC are executed via actuating the 3 Hall probe stabilisation system accordingly. The motor drivers used are from Faulhaber [22] and are connected to the Raspberry Pi through a Controlled Area Network (CAN), specifically CANOpen according to the CAN in Automation standards CiA301 and CiA 402 standards [23, 24]. The master of the CANOpen network is the Raspberry Pi and the motor drives for all motors on the bench are separate nodes. The loop for the Hall probe positioning system is therefore closed and correction can be performed.

Magnetic data acquisition in the measurement procedure is performed by a Three-Axes Teslameter [5] that communicates with the Raspberry Pi through an isolated Universal Serial Bus (USB). The Teslameter is directly connected to a Heidenhain linear encoder such that every magnetic measurement is paired with an absolute encoder value for accurate field mapping. The data transferred over the USB includes the start and stop for the magnetic measurements and the current position of the bench in encoder counts. The magnetic measurement data is stored internally on the Teslameter and can be read after a current measurement is finished.

The Raspberry Pi can read the Heidenhain encoder directly via an EnDat master node that is developed such that the bench can operate without the Teslameter since the Heidenhain encoder is normally connected to the Teslameter during normal operation. The EnDat protocol [1] is implemented on dedicated hardware and the encoder position can be read by the Raspberry Pi through Serial Peripheral Interface (SPI).

The bench is operated through a Beckhoff PLC that is running the Windows operating system where a Graphical User Interface (GUI) was developed using python. The commands are transferred from the GUI to the on-board Raspberry Pi through a Transmission Control Protocol (TCP) communication link over Wi-Fi where all different aspects of the bench can be controlled including moving motors and start or stop measurement commands.

All the electronic system of the bench are implemented on two Printed Circuit Boards (PCBs) with 100mm x 40mm dimensions. The first PCB includes the Raspberry Pi board, ZigBee radio module, motion control circuitry, USB and SPI isolation circuitry and the EnDat protocol hardware. The second PCB has extra motion controllers for the rest of the bench's motors and an extension connector that connects to the first PCB. The second PCB also includes battery charging circuitry that operates the bench entirely from a suitable battery and eliminates the need for power cables to move along with the bench during measurements.

A block diagram of the previously implemented system is shown in Figure 3.8.

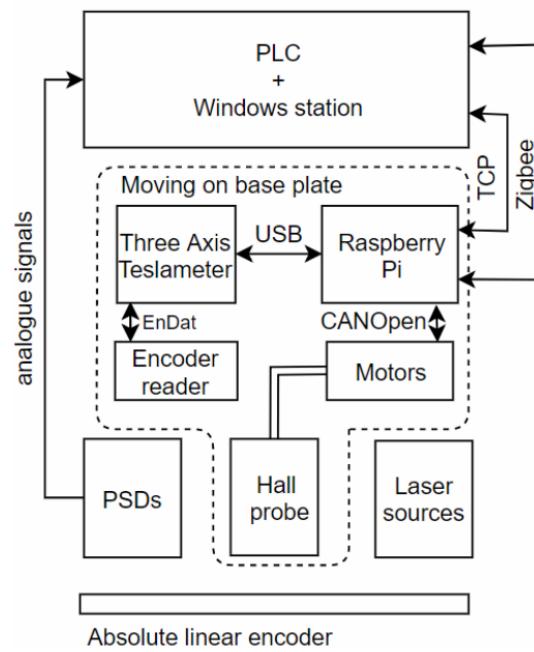


Figure 3.8: Block Diagram of the Previously Implemented Bench [4]

3.2.1 Limitations of the Previously Implemented Electronics System

The manufactured PCBs A and B shown in Figure 3.9 have 4 layers each and utilise both the top and bottom layers for components placement and with no clear fixation points to the mechanical bench. To avoid any unwanted connections due to the components situated in the bottom layer contacting the aluminium base plate, certain clearance is required between the based plate and the bottom layer. Also, no clear mounting mechanism for the Three-Axis Teslameter was considered in the implemented electronics which might be problematic during measurement of an IVU where all the electronics including the Teslameter must fit inside the vacuum chamber.

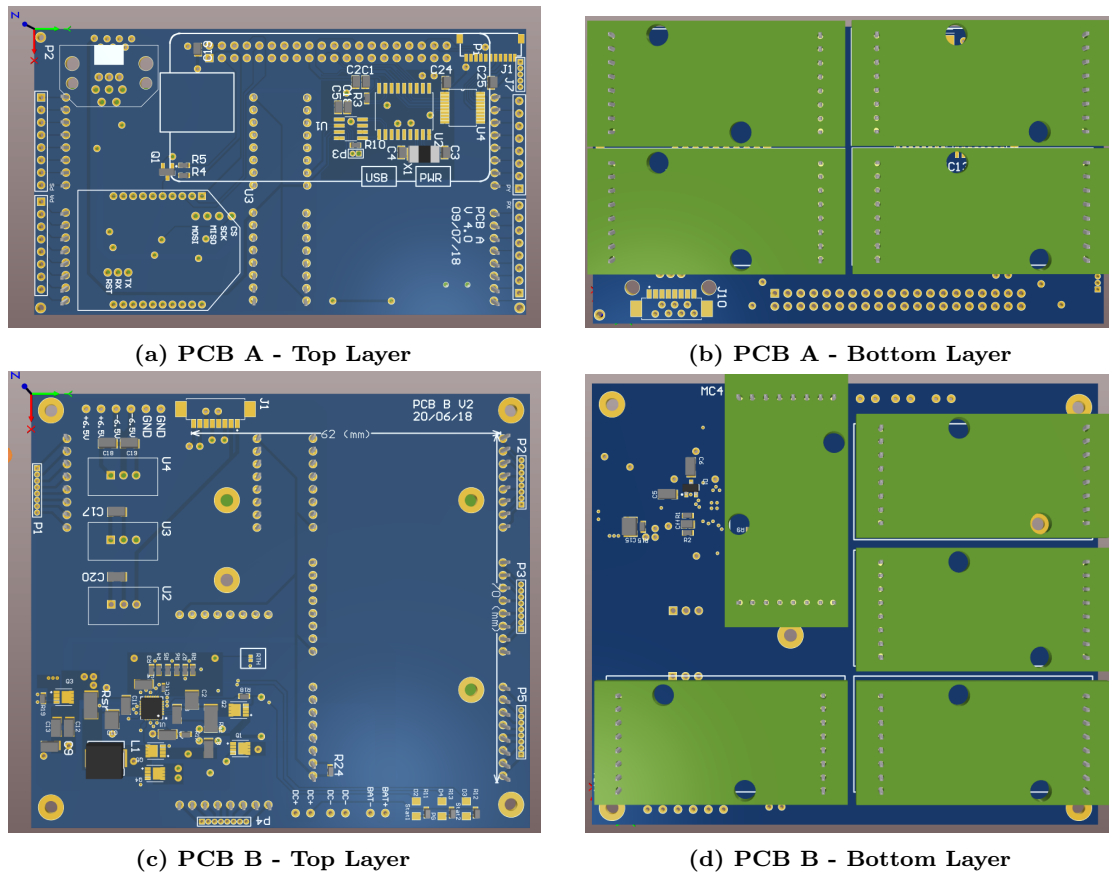


Figure 3.9: The Implemented PCBs for μ MMB

The power distribution for the on-board electronics on PCB A is dependent on voltage regulators located on PCB B and PCB B lacks a 12V regulator for the motor drives and instead, it relies on the input voltage from an external power supply to power the motor drives. The input voltage from the external power supply is routed to a $\pm 6.5V$ and 5V regulators for the Teslameter and the control electronics respectively, however, the motor drives are powered through a battery charging circuitry. This circuitry introduces voltage drops across several components and these must be catered for from the external power supply such that the correct voltage level reaches the motor drives which is 12V in this case. This makes the motor drives dependant on a voltage level from the external power supply to operate. This approach can be improved to eliminate this dependency.

3.3 Improvements on the Previously Implemented Bench

There were several sever mechanical limitations to the previously assembled bench discussed in Section 3.1.3, and also some minor drawbacks of the electronics systems and manufactured PCBs. The Hall probe holder lacks stiffness and strength to support the weight of the Hall probe lever which renders two out of the three correction stages

unusable. The mechanical team at the insertion group at PSI have designed a new holder with larger surface area and better mechanical strength to support the weight of the Hall probe lever. A 3D design of the old and the new holders are shown in Figure 3.10.

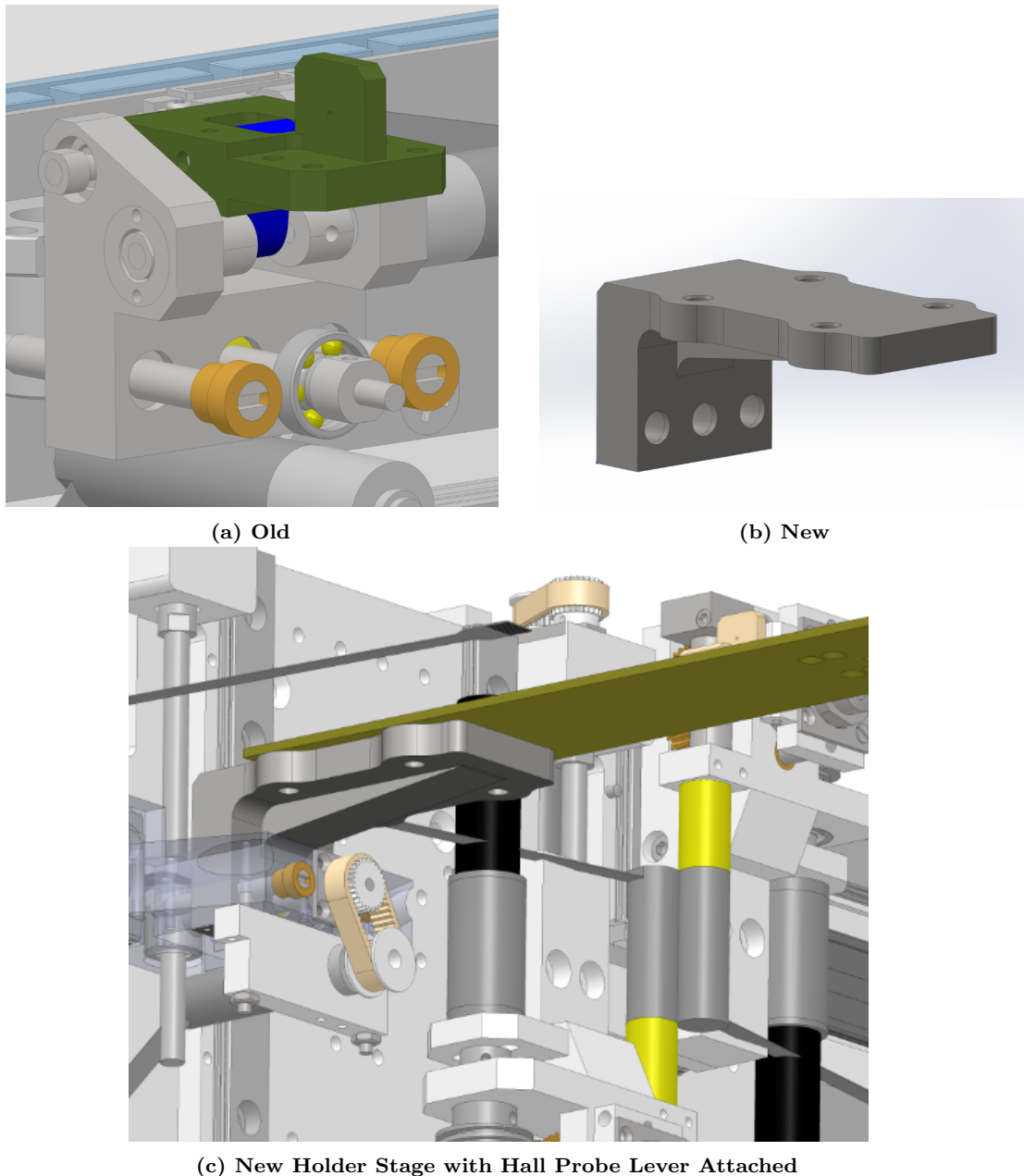


Figure 3.10: The Old and the New Hall Probe Holders

The new probe holder provides better support for the Hall probe lever, however, the roll angle correction stage is discarded as it is not possible to include a proper stage that caters for it in a new design due to some technical difficulties at the Insertion Devices Group at PSI. Long lead times from manufacturers and other higher priority projects, mainly the SLS2.0 upgrade, resulted in designing and manufacturing

of a fast solution to improve the mechanical stability.

The significance of errors caused by the roll angle in the magnetic measurement become apparent when the device under measurement is several meters long. Since the new undulator prototype is relatively short, the roll angle correction can be omitted without significant effects on the quality of the magnetic measurement.

The clearance inside the new vacuum chambers for the next generation of undulators at PSI is small and the usable vertical space above the top surface of the base plate of the bench is approximately 42mm. This limits the mounting options of the electronics on an extension plate adjacent to the main base plate. Also, the Teslameter's height is 41.9mm which makes it impossible to actually mount it comfortably with the available space in an extension plate that has the same thickness as the base plate. Figure 3.11 shows the space available inside the vacuum chamber for the new generation of undulators.

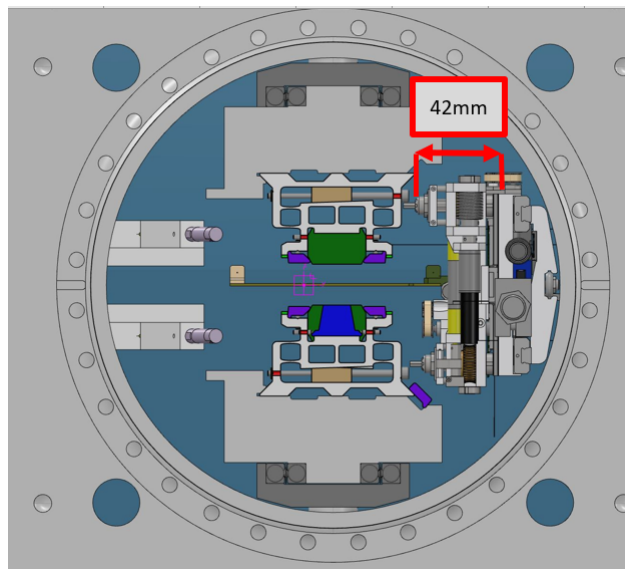


Figure 3.11: The Space Available Inside the New Vacuum Chamber

The base plate of the bench is 8mm thick and since it incorporates all the mechanical subsystems of the bench, it is required to have excellent stiffness and strength. Moreover, the electronics implemented for the bench do not require sturdy support to operate properly and can be attached differently to the mechanical bench. Hence, the implementation of the electronics was improved with some changes to the components used for the various tasks. The new implementation is based on 2 PCBs, one acts as the base plate and has all the electronics placed on the top layer with sockets to install other pieces of the system modularly and includes mounting points to attach the Teslameter.

The other PCB has all the communication and control components with pin headers on the sides which can be plugged into the base plate PCB. The base plate has 4

mounting points for frictionless linear bearing at each corner, similar to the ones used for the other base plate, such that it can be installed on the rail and can travel freely along the undulator with the mechanical bench.

This approach increases the available space inside the vacuum chamber by the thickness of the base aluminium plate, which is 8mm, and with 2mm spacers below the base plate, approximately 6mm of comfortably usable space is added assuming the base PCB thickness is negligible.

An improved power delivery approach with extra safety features was implemented on the base PCB where only one external DC power supply is needed to operate all the bench's components; separate 12V regulators for powering the motors that are independent from the external source were also added. The input voltage to the electronics can be supplied from a standard PLC power supply that can provide 18-30V.

A block diagram of the new implementation of the μ MMB is illustrated in Figure 3.12

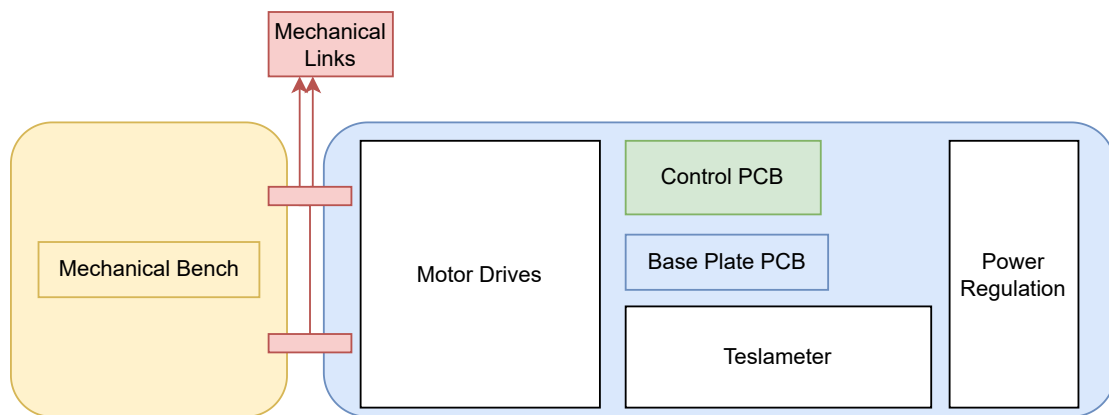


Figure 3.12: Block Diagram of the New Implementation of the μ MMB

Along the mentioned improvements, the software to operate the bench was revised with user friendliness in mind such that any individual who is interested in using the bench can perform measurement without the need to know the system components specifically. This is achieved by improving on the software implemented previously and designing a simple Graphical User Interface (GUI) local on a Programmable Logic Controller (PLC) running Windows operating system. The different components on the new PCBs and other improvements are explained in detail in Chapter 4

3.4 Motion Control Design and Performance

The bench is equipped with low profile linear motor from the manufacturer Airex and C10 series [25]. The choice of this motor was made by the mechanical engineers at the Insertion Devices Group at PSI primarily due to its compact size and low

profile compared to other industry solutions. The motor is of the BLDC type and is composed of two parts which are the iron-less core and the permanent magnetic array, the core has 3 phases internally and can be moved along the slotted permanent magnets array by exciting the phases accordingly with a suitable motor driver. This modularity in the motor composition provides flexibility in the length of the motor tracks as more permanent magnets arrays can be cascaded to increase the travel distance of the motor. Figure 3.13 shows the Airex C10 motor used.



Figure 3.13: Airex C10 Series Linear Motor [25]

The core of the linear motor is mounted on a groove located on the bottom side of the aluminium base plate of the bench and the permanent magnets array are fixed to the rails on the side of the vacuum chamber.

The main disadvantage of the linear motor is the lack of commutation system for the motor coils which are essential for the ability to drive the motor phases correctly, this was solved by introducing external Hall effect sensors to provide the necessary feedback to the motor drives for appropriate actuation. In typical rotary BLDC motors, the commutation feedback is provided from internal Hall effect sensors that are embedded inside the motor's chassis, however, this is not possible in this case as there is no direct access to the motor coils due to its design and from the motor's core installation place which is in a groove under the base plate.

A solution was previously implemented to address this issue by designing a custom PCB with 3 Hall sensors to be installed at a certain distance from the motor's core. Since the permanent magnet's array is constructed from identical permanent magnets, a feedback signal that is identical to the one that is obtained from the typical sensors can be obtained by placing the Hall sensors at a distance that is a multiple of the magnetic period length from the motor's coils; this approach assumes that the permanent magnets in the array are identical or have very low magnetic tolerance.

Figure 3.14 illustrates the commutation solution for the linear motor explained above.

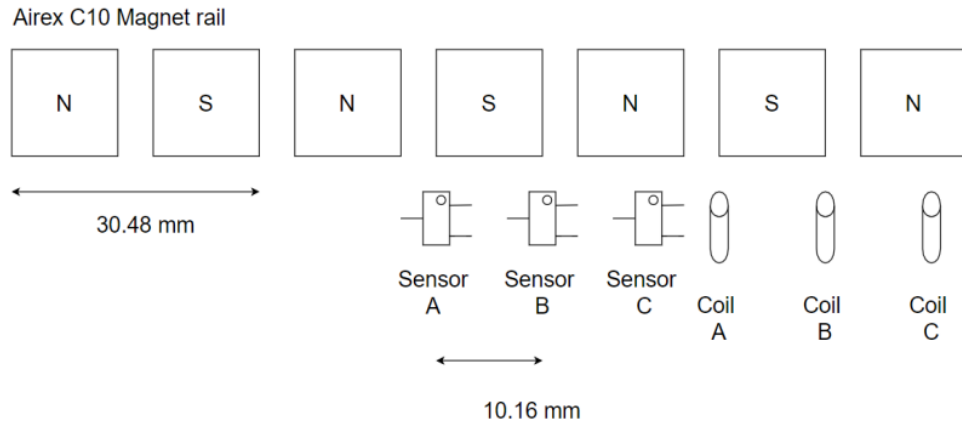


Figure 3.14: Linear Motor Commutation Solution [4]

The motor driver of choice is the (MCLM3002) from Faulhaber [22] which provides excellent performance and flexibility for its compact size. The choice of this motor driver was mainly due to the size and the ability to integrate multiple drives in a single data bus and also due to supply shortage of the newer more compact model the (MC 3001) [26] where an estimated delivery time was set for a year from the date of order placement which would have exceeded the time frame for this project. Hence, the older version of motion controller from Faulhaber was used.

The motion controller requires Hall analogue feedback signals to control the linear motor correctly and therefore a custom solution to provide the commutation signal was implemented. The magnetic period of the linear motor's rail was measured to be 30.48mm hence, for a typical BLDC motor consisting of 3 phases/coils, the distance between the Hall sensors should be $\frac{30.48}{3} = 10.16$ mm to achieve a 120° phase lag between the commutation signals electrically.

The Hall sensor used is the Silicon Labs Si7211 Magnetic Hall sensor [27] is supplied in a small 3-pin SOT23 surface mount package with excellent linearity and low noise. The sensor is powered with a dedicated 5V signal supplied from the motion controller and provides a signal of 2.5V when the magnetic field is near zero and near 5V and 0V when a large or low magnetic field is present respectively. A custom PCB was manufactured to house the required 3 commutation signals at the correct distance apart as shown in Figure 3.15. For correct commutation and smooth movement of the linear motor, it is essential for the Hall effect feedback sensors to be placed precisely at a relevant position such that the signals to the motion controller is identical to the one near the linear motor's coil. Since the physical position of the motor coils is not provided by the manufacturer, an experimental method was used to optimise the position of sensors to achieve the required functionality.

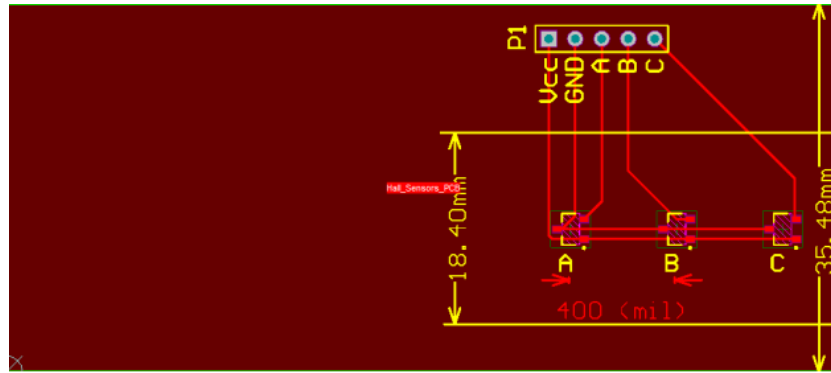


Figure 3.15: Custom PCB for the Hall Effect Sensors [4]

A suitable position was found where the signals from the Hall sensors are approximately aligned with the motor coils and 2 holes were drilled into the edge of the PCB. The PCB is then fixed to an aluminium extension piece at the edge of the mechanical bench via 2 countersunk hex bolts marked by the red circles in Figure 3.16.

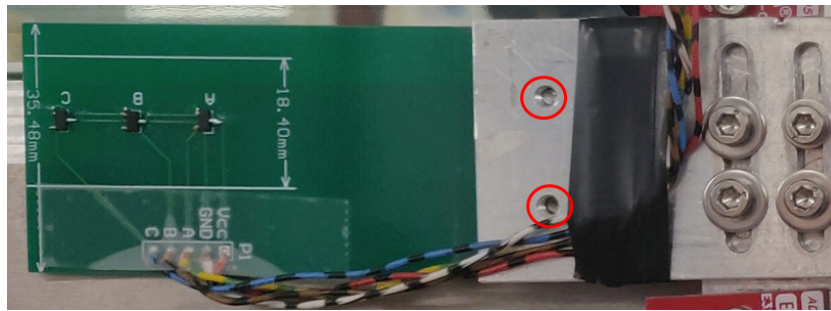


Figure 3.16: Custom Commutation PCB attached to the Bench

3.4.1 Linear Motor Performance

The MCLM3002 motion controller supports multiple operation modes such as position control where the user can specify a certain position and the controller would drive the motor to that position according to predefined internal parameter, or velocity mode where a velocity value is specified and the motion controller would maintain that velocity as long as a stop condition is not encountered. The linear motor is responsible of carrying the Hall probe sensor along the undulator at a constant velocity with little fluctuations from that value, therefore, the motion controller is operated in velocity mode.

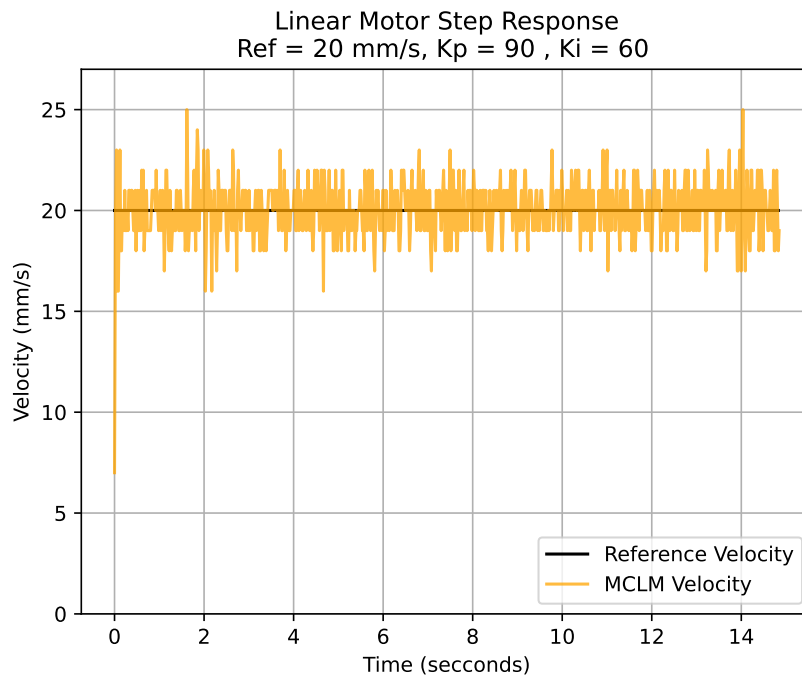
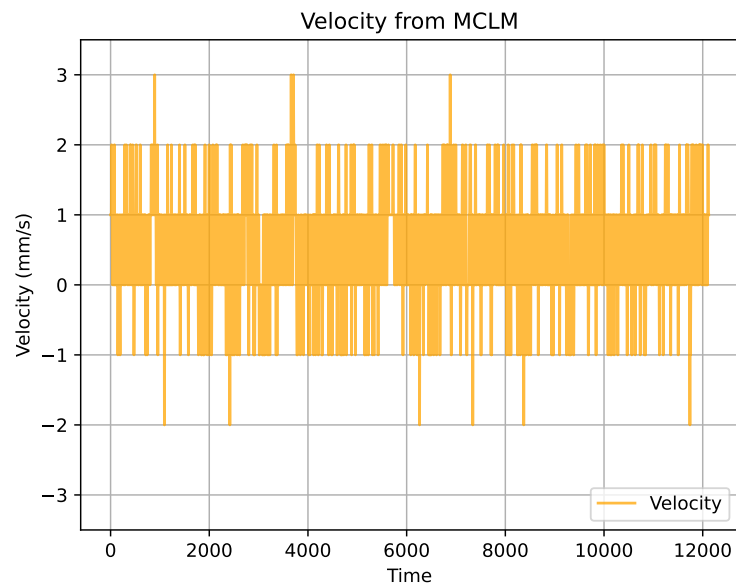


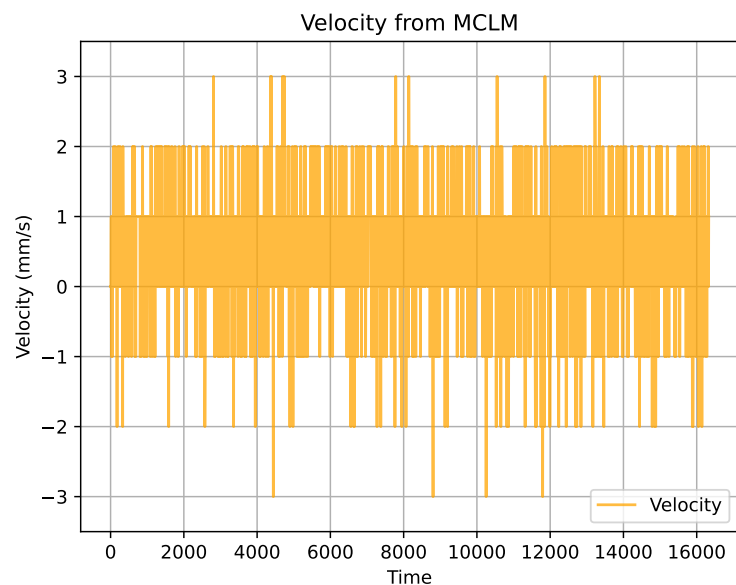
Figure 3.18: Initial Linear Motor Step Response - $K_p = 90$, $K_i = 60$

The velocity PI controller tuned parameters are performing 15% [4] worse than the previously implemented system with peak velocity values reaching up to 25mm/s; this could be due to various aspects such as the exact position of the commutation Hall effect sensors or changes in the motor coil parameters.

The value of the velocity was obtained directly from the motion controller and several tests were performed to verify the reported velocity values are accurate. The first test was to obtain the velocity value from the motion controller when the power to the motor is turned off i.e. the MCLM3002 is supplied with power however, the outputs to the motor coils are disabled. The obtained velocity measurement was noisy with peaks oscillating between ± 2 mm as shown in Figure 3.19a. Another test was performed where the target velocity was set to 0 mm/s and the outputs of the MCLM3002 were enabled i.e. the motor is actively powered to maintain a velocity of 0mm/s. The velocity plots are as shown in Figure 3.19b.



(a) Velocity Recorded from the Motion Controller When no Power was Supplied to the Motor



(b) Velocity Recorded from the Motion Controller When Velocity Target = 0mm/s

Figure 3.19: Ambient Noise Levels of the Velocity Values from the Motion Controller

From the results shown in Figure 3.19, it can be seen that the velocity values reported by the motion controller are digitally noisy in both cases when the motor is not supplied with power and when the motor is powered with target velocity of 0mm/s. As mentioned previously, the motion controller is capable of maintaining the target velocity to within ± 1 mm/s of the accuracy which is within the required specifications for this application, however, other sources could have contributed to

this digital noise such as the noise from the Hall effect sensors or the electronics and the controller design of the motion controller itself.

Further tests of the velocity controller were conducted and the optimum step response was noted when $K_P = 110$ and $K_i = 70$. The velocity step response with these gain values shown in Figure 3.20 illustrates the reference velocity of 20mm/s in black, the actual velocity from the motion controller shown in orange, and the average velocity in red where the average was taken with a moving average filter with a windows size of 3 values i.e. a low-pass filter was implemented to reduce the effect of the high frequency components of the velocity data signal received from the motion controller. The maximum, minimum and mean value from the averaged velocity plot are 22mm/s, 18.1mm/s and 20mm/s respectively.

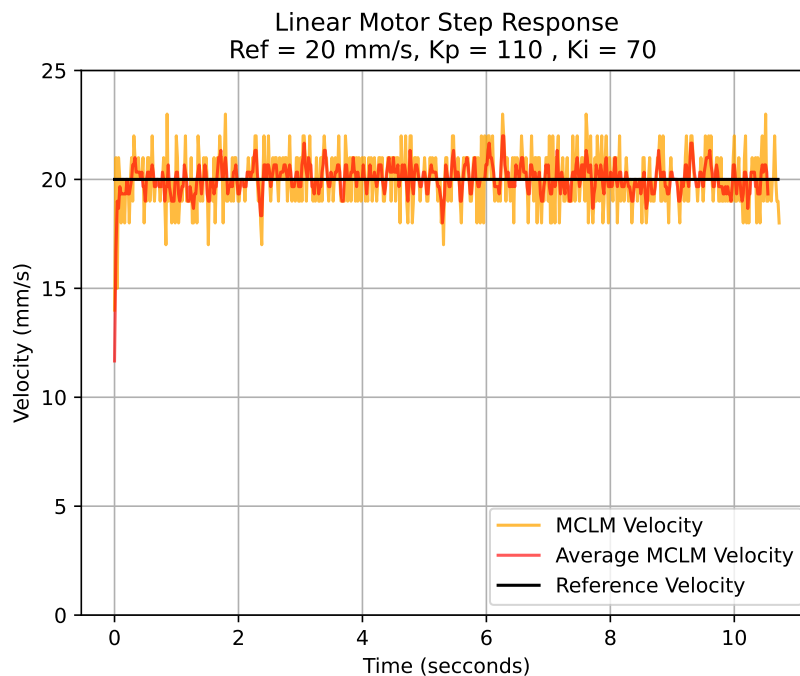


Figure 3.20: Linear Motor Velocity Step Response - $K_P = 110$, $K_i = 70$

3.4.2 Overview of the CAN Bus

The Controlled Area Network (CAN) was selected to implement the motion control systems for all the motors of the bench after the choice of the motion controllers was confirmed. The motors used for motion on the bench can be easily integrated in a system when such motion controllers are used where the provided performance, functionality and compactness is sublime. Also, the bench has 9 motors in total and each require a separate motion controller, this makes CAN an ideal choice as all motors can be actuated precisely using a single fast and efficient communication bus.

CAN is a robust and widely adopted communication protocol used in various industries for real-time data exchange between electronic devices within vehicles and other embedded systems. The bus was initially developed for automotive applications and has evolved into a versatile and reliable communication bus standard. Its design prioritizes efficiency, reliability, and high-speed data transmission, making it well-suited for applications where multiple electronic components need to communicate seamlessly. The CAN bus facilitates a decentralized network architecture, allowing devices to share information efficiently without relying on a central controller. Its applications extends beyond automotive contexts where it can be used in industrial automation, medical devices, and various other domains where reliable and real-time communication is essential.

The CAN bus consists of 2 differential data lines which are CAN-High and CAN-Low and are terminated with a common 120Ω resistor at an appropriate location in the implemented bus, and all devices or (nodes) are connected and can communicate through those 2 data lines. A single node can transmit data on the data lines, the message is received by all nodes, however, it is ignored by all nodes except the one with the correct identifier. Figure 3.21 illustrates a simplified block diagram of a CAN network with multiple nodes and the termination resistor and data lines.

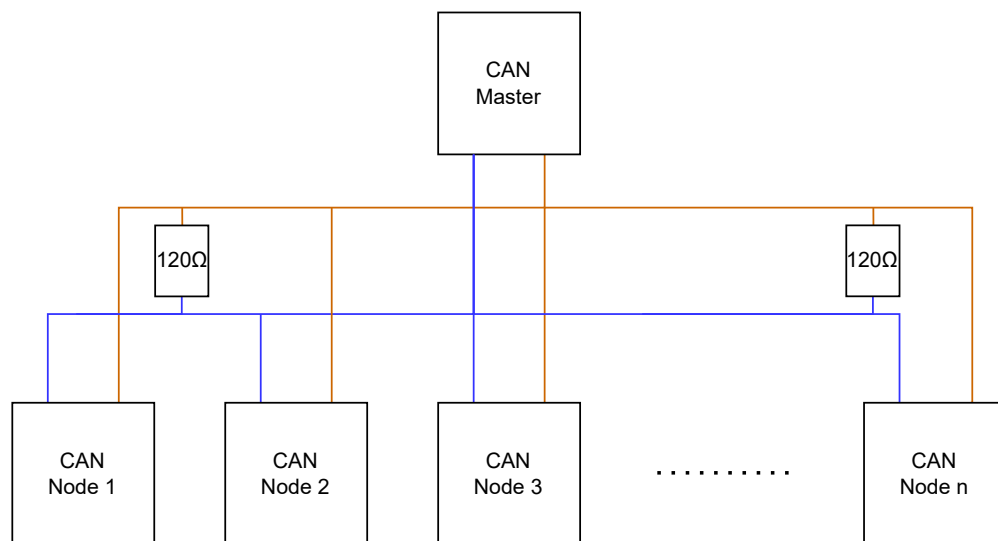


Figure 3.21: Block Diagram of a Generic CAN Network

The motion controllers used (MCLM3002 and MCBL3002) support CANopen bus which utilises the physical and data link layers of CAN to introduce a higher layer of framework to broaden the scope of communication capabilities. There are several standards that define the CAN communication usage in various applications such as CAN in Automation (CiA301) [23] which defines the CANopen application layer and the CiA402 [24] which outlines a standardised usage for the CANopen protocol for

drives and motion controllers. The number of nodes that can be connected to a CAN network is 127 nodes and the data transfer rates can reach up to 1Mb/s.

Each node connected to the CAN bus is distinguished by a unique value called the node ID which allows for the target node to receive the message and other nodes to ignore it. The CAN message follows a defined format that starts with a function code, followed by the node ID, Remote Transfer bit (RTR), data length specifier, and the actual data to be sent. A generic CAN message format is shown in Figure 3.22.

Function Code 4-bits	Node ID 7-bits	RTR 1-bit	Data Length 4-bits	Data up tp 8-bytes
-------------------------	-------------------	--------------	-----------------------	-----------------------

Figure 3.22: CAN Message Format

While standard CAN messages offer flexibility and general communication means, CANopen messages provide more structured and standardized approach for communication between nodes which incorporates specific predefined data structures for various purposes within a CANopen network. The data in a CANopen node is stored in the Object Dictionary (OD) which contains information about the monitoring and control parameters, configuration settings, and status information of nodes connected to the network. The information on the OD can be accessed and changed via Service Data Object (SDO) or Process Data Object (PDO). SDO is used in the implemented CANopen bus of the bench to communicate with the motion controllers and modify the OD the relevant OD parameters. PDO is less suitable for the task since most of the information carried on a PDO message is not required continuously which overwhelms the bus with extra data traffic that is not needed.

The motion controllers used in the bench specifies data exchange via SDO operations where the required parameter to be read or written to the OD is addressed by 16-bit index and an 8-bit sub-index which are embedded in an SDO message. A generic SDO message in a CANopen network is as shown in Figure 3.23.

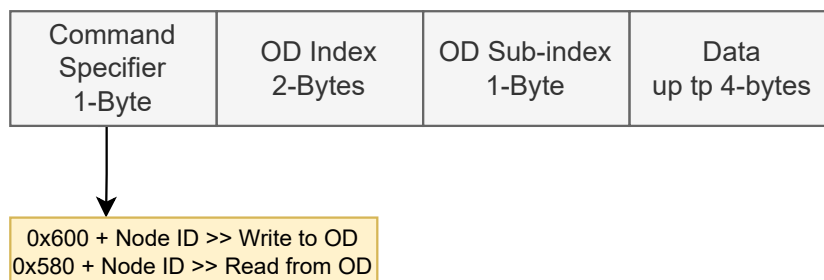


Figure 3.23: CANopen SDO Message Format for the Faulhaber Motion Controllers

The motorised screwdrivers and the Hall probe positioning systems are both actuated via 8 Faulhaber motors and the motors are driven via supported Faulhaber

motion controllers, hence, the CANopen bus consists of 8 nodes. The motion controllers are small in design which is an important aspect due to the space constraints in this project. A smaller version of motion controller from Faulhaber (MC3001) [26] was to be used, however, due to availability and long lead times from supply chain issues, the older version that was used in the previously implemented bench were used which are MCLM3002 for the linear motor, and the MCBL3002 for the BLDC servo motors [22]. The usage of the older Faulhaber motion controller performance is nearly identical to the newer MC3001 hence no performance impact was noted from using them.

The MCBL3002 and the MCLM3002 are supplied in a Through Hole package (TH) with dimensions of 47mm and 23mm, the TH package allows for integration into a PCB with an appropriate socket for simple and fast installation and repair. Figure 3.24 shows the size of the MCBL3002, and similarly the MCLM3002, next to 50 cent Euro coin as a comparison.

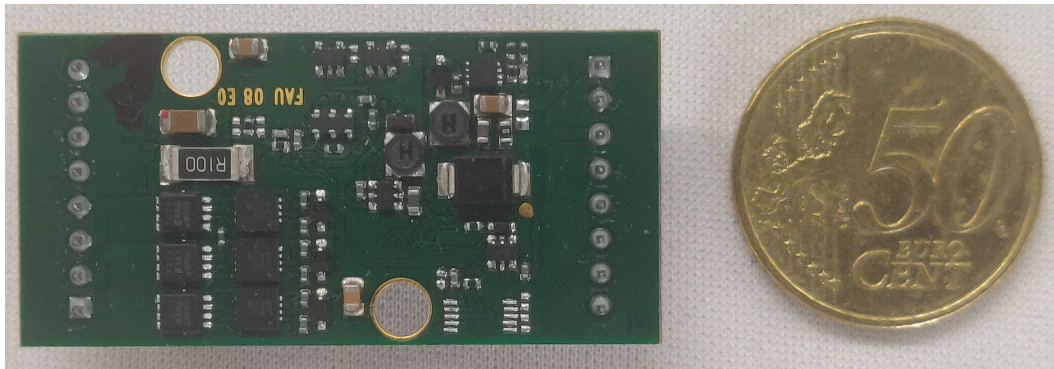


Figure 3.24: MCBL3002/MCLM3002 Motion Controller From Faulhaber

The motion controllers MCBL3002 are paired with the Faulhaber 0824B and 1024B BLDC servo motors which as mentioned previously are integrated in the design of the mechanical bench. The main advantage for these motors is the compact size where the package is cylindrical with 8mm and 10mm in diameter and 24.1mm and 28.1mm in length for the 0824B and 1024B motors respectively. 2 of the larger 1024B motors are used for each head of the motorised screwdriver which was done due to the extra torque needed for rotating the magnetic adjustment hex screws. Apart from the linear motor which is paired with the MCLM3002, the rest of the motors for other movement in the bench are the smaller 0824B and are paired with the MCBL3002. All motors are also equipped with single-turn absolute encoders with 4096 increments per shaft revolution; Faulhaber also support various compatible gearboxes which allows for the final assembly of the motor in combination with the gearbox and the absolute encoder to achieve excellent performance in position control of the probe

position assembly.

3.4.3 Implementation of the CAN Bus

The implemented CANopen network has the Raspberry Pi as the master node and the MCLM3002 and the 7 MCBL3002 as nodes which totals to 8 nodes. The master node on the Raspberry Pi is implemented through a combination of a standalone CAN controller Integrated Circuit (IC) and python software established by [Dalli et al.](#) and further improved for better functionality.

The CAN controller is the MCP25625 from Microchip [29] which is a standalone CAN controller with integrated transceiver that drives the differential CAN_High and CAN_Low signals and eliminates the reliance on a separate transceiver IC for a compact hardware design. The interface between the MCP25625 and the Raspberry Pi is through Serial Peripheral Interface (SPI); the Raspberry Pi's ARM System on Chip (SoC) has several on-board SPI controllers, however, only the main SPI module on the SoC is hardware capable and solely available for the SPI communication protocol. Therefore, the hardware SPI was used instead of the other auxiliary SPI where hardware of those are mostly shared with other communication protocols on the SoC. [30].

All motion controllers are initialised using the Faulhaber Motion Manager software and setup data is retained locally on the motion controller's memory. A block diagram of the implemented CANopen network with all nodes connected to the controller and transceiver IC is shown in Figure 3.25.

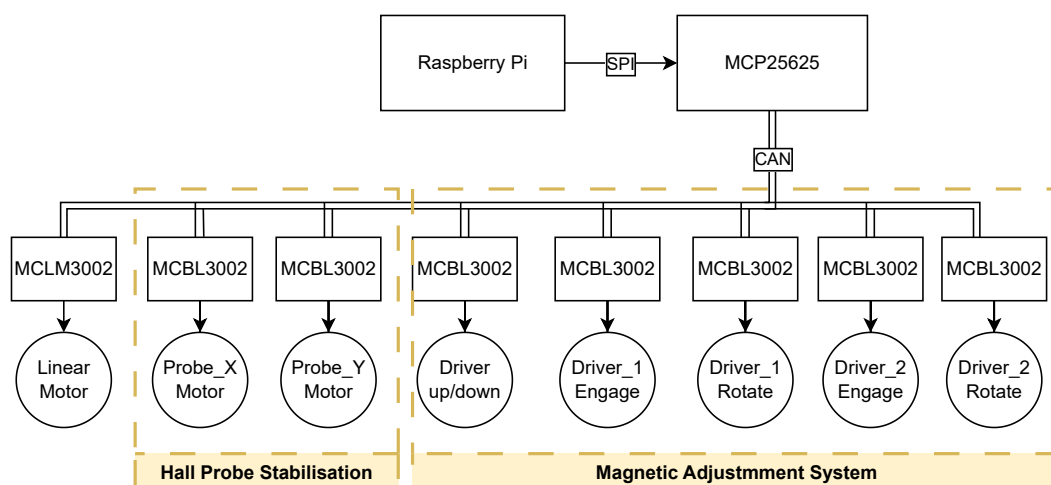


Figure 3.25: Block Diagram of the Implemented CANopen Bus

The function of each motor is as follows:

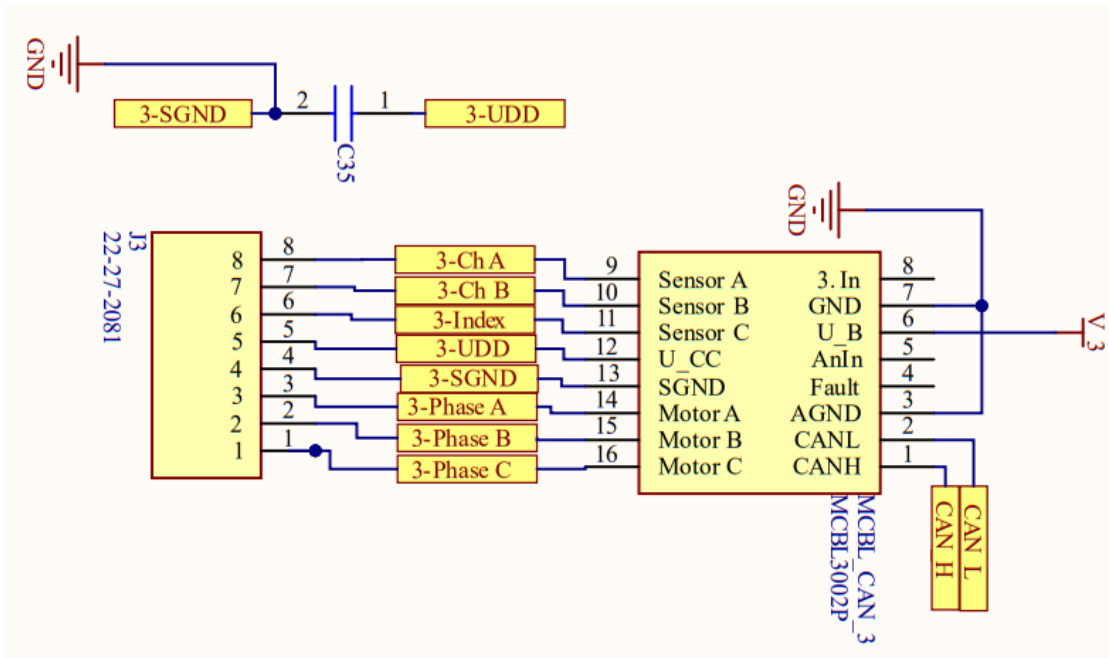


Figure 3.27: Schematics of a Motion Controller

The hardware of the CANopen bus is located on the Control PCB and the bus is extended to the base plate PCB via an edge pin headers that plug into a socket on the base plate PCB. This approach provides flexibility in the choice of the control hardware and future improvements are possible without the need to redesign all aspects of the bench. A custom component and footprint of the control PCB were created and integrated into the schematics of the base plate PCB. The schematics of the custom component is illustrated in Figure 3.28

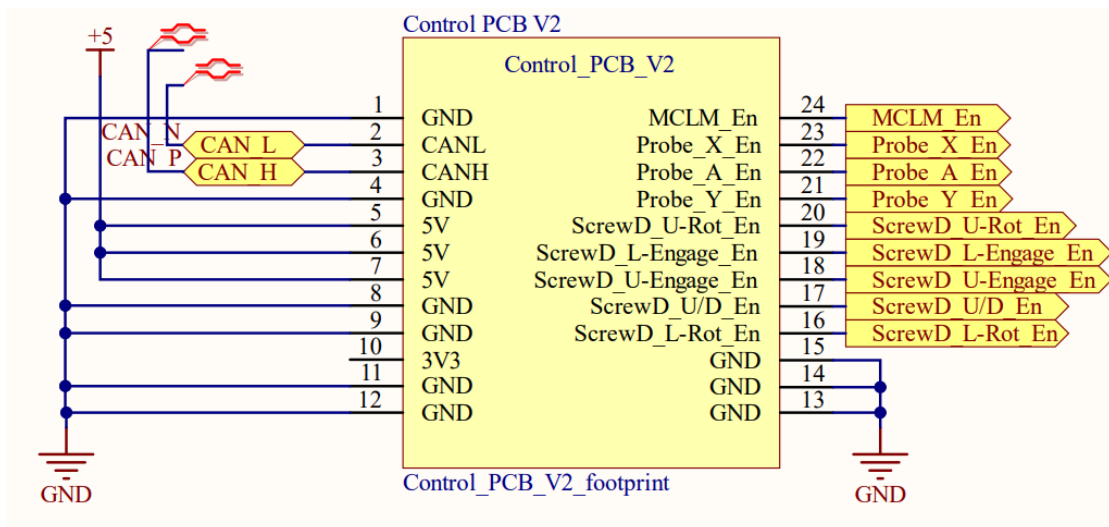


Figure 3.28: Custom Component Created of the Control PCB

3.4.3.1 Software of the CANopen Bus

The link between the MCP25625 and the SPI hardware on the Raspberry Pi is realised by an open-source kernel for linux operating systems called “SocketCAN” [31]. The SocketCAN kernel creates a CAN bus “can0” when the operating system is booting and links the MCP25625 CAN controller and the SPI module on the Raspberry Pi. The kernel utilises *py-can* Python package to interface to the “can0” bus created and allows for simple access to the CAN hardware (Controller and Transceiver) through Python software.

A local python module was implemented [4] and was further improved to increase the functionality of the CAN network and provide better control of the motion controllers and subsequently the motors. The module composed of one class “Motor” which has a single constructor that defines the node ID of the class instance or the created node. Adding a new motor node to the network is possible by creating multiple instances of the class and specifying the node ID. The two core methods of the Motor class are as follows:

send_can_msg(arbitration_id, data) Is used to send data over CAN to a pre-defined CAN node. Two parameters are passed to the method which the `arbitration_id` and `data`. The `arbitration_id` contains the CAN node id and the hex value to read (0x580) or write (0x600) to and from the OD respectively. The `data` parameter contains the index, sub-index of the object in the OD and up to 4-bytes of user data can be sent. For instance, to read an object from the OD, the format is: `send_can_msg(0x580+node_id, [CS, index_low_byte, index_high_byte, sub_index_byte, data_byte1, data_byte2, data_byte3, data_byte4])`. The Command Specifier (CS) indicates the number of valid bytes in the data sent in the CAN message.

read_od(index) Is used to read object data stored on the OD. A single parameter is passed to the method which is the index of the object in the OD and is composed from 3 bytes (index low byte, index high byte, sub-index byte) describing the location of the object. The method makes use of the `send_can_msg(arbitration_id, data)` method, however, with a change in the `arbitration_id` to mark a read command. For instance, to read an object data from the OD, `read_od(index)` is used and `index` is passed to the send method. The format of the send message is: `send_can_msg(0x600+node_id, [CS, index_low_byte, index_high_byte, sub_index_byte])` and the node which corresponds to the `can_id` replies with the data from the specified OD object. The Command Specifier (CS) indicates how many bytes are valid from the specified object in the OD.

Index Name	Index Low-Byte	Index High-Byte	Sub-index Byte
CONTROLWORD	0x40	0x60	0x00
STATUSWORD	0x41	0x60	0x00
OPMOD_SET	0x60	0x60	0x00
OPMOD_GET	0x61	0x60	0x00
POLARITY_SET	0x7E	0x60	0x00
ACTUAL_VEL	0x6C	0x60	0x00
TARGET_VEL	0xFF	0x60	0x00
ACTUAL_I	0x78	0x60	0x00
ACTUAL_POS	0x64	0x60	0x00
TARGET_POS	0x7A	0x60	0x00
VEL_P_GAIN	0x31	0x23	0x01
POS_D_GAIN	0x32	0x23	0x02
POS_P_GAIN	0x32	0x23	0x01
MIN_POS_LIM	0x7D	0x60	0x01
MAX_POS_LIM	0x7D	0x60	0x02
HOM_MET	0x98	0x60	0x00
HOUS_TEMP	0x23	0x23	0x01
INTER_TEMP	0x23	0x23	0x02

Table 3.1: List of Frequently used indices for OD Objects for the Faulhaber Motion Controllers MCLM3002 & MCBL3002

A list of object indices in the object dictionary are stored in constants to allow for easy access to the more frequently used objects and improves code readability for future users. Table 3.1 shows the indices of the frequently accessed objects in the Object Dictionary.

From the OD objects shown in Table 3.1, the CONTROLWORD and STATUSWORD are unique parameters that are defined by the Can in Automation CiA 402 standard, which are used to perform a change of state and to indicate the current state of the motion controller respectively. Both special objects are 1-byte and each bit specifies a specific state in the motion controller, bitwise procedures are performed on the byte received to obtain a particular operation. The control words, shown in Table 3.2 were hardcoded into the python module for code readability and ease of use.

Other methods implemented in python modules rely on the 2 core functions to achieve certain changes to the OD parameters and consequently the behaviour of the

State Change	HEX Code
Shutdown	0x07
Switch-on	0x06
Disable Voltage	0x00
Quick Stop	0x02
Disable Operation	0x07
Enable Operation	0x0F
Enable Relative Positioning	0x7F
Enable Absolute Positioning	0x3F
Enable Homing Start	0x1F

Table 3.2: CONTROLWORD Byte and the Corresponding STATUSWORD

motion controller and monitor errors and safety parameters such as over current and the temperature of the electronics onboard the motion controllers. The methods are easily reusable and allow the user to control every aspect of the motion controller via software which translates to full control over the motion systems of the bench. The next section provides an overview of the Hall probe positioning system implementation which utilises the implemented CANOpen bus to execute position correction.

3.4.4 Hall Probe Positioning System Controllers & Performance

The new mechanical Hall probe holder shown in Figure 3.10 provides better mechanical support of fibre glass lever and therefore, should improve the stability of the probe positioning system. The motion controllers used to control the probe positioning system are the MCBL3002 [22] from Faulhaber which are of the same family as the motion controller used for the linear motor. Similar to the MCLM3002, the MCBL3002 can operate in various modes as described below:

Position Mode The motion controller receives the target position from the master controller, in this case the Raspberry Pi, and the value is scaled accordingly to satisfy predefined parameters, the motor is then moved to the target position and actively maintains that position until a change of state condition is met. The target position could be defined in terms of relative or absolute position.

Velocity Mode Similar to the linear motor motion controller, the target velocity is set by the master and the controller actuates the motor accordingly to reach the set velocity value according to predefined acceleration and deceleration values. This mode is not relevant for the Hall probe positioning system.

Cyclic Synchronous Position Mode (CSP) Unlike the position mode, the target position values from the master are passed immediately to controller and motor is actuated as per the controller parameters. However, when a new position value is received, the new value is considered as the new target value immediately and overrides the older target position even if the older target position is not reached yet. This mode requires the target position to be specified only as an absolute value.

The CSP mode is the most suitable one for the application as the correction values sent by the Raspberry Pi are executed instantly without delays as opposed to the normal position mode. The position controller of the MCBL3002 is shown in Figure 3.29.

The MCBL3002 receives a reference position input that is firstly verified to be within the software defined limits and is multiplied by a factoring value which corresponds to the predefined gear ratio which was derived from the physical system connected to the shaft of the motors as per Figures 3.4 and 3.5. The current position of the motor shaft is obtained from the feedback signal provided by an absolute encoder (AES) installed within the body of the motor and the error is calculated internally; the position is controlled through the outer Proportional Derivative (PD) internal controller and the motor is actuated with a Proportional Integral (PI) velocity controller with ramp generation whose parameters are predefined during the controller initial setup. A current controller is also implemented internally to actively monitor the driving current of the motor and prevent any damage to the motor and the motion controller without affecting the controller's response while the current limit is not exceeded.

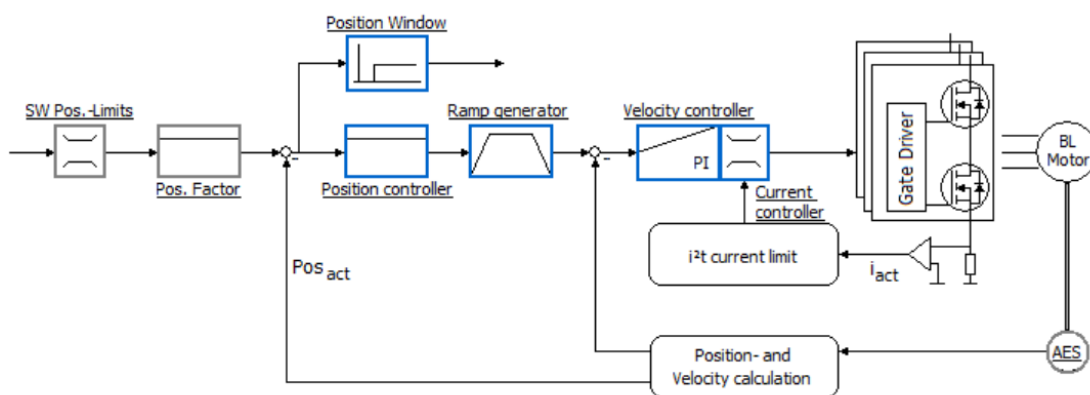


Figure 3.29: Block Diagram of the Position Controller of the MCBL3002 [28]

As previously defined, the task of the Hall probe stabilisation system is to align the probe holder to the centre of the undulator under measurement and actively corrects any deviation from that position during measurement where the Hall probe traverses

the length of the device under test. Apart from the mechanical issues faces with the previously implemented SAFALI system, the feedback mechanism performance was satisfactory and no alteration were performed in that aspect. A block diagram of the implemented SAFALI system is shown in Figure 3.30.

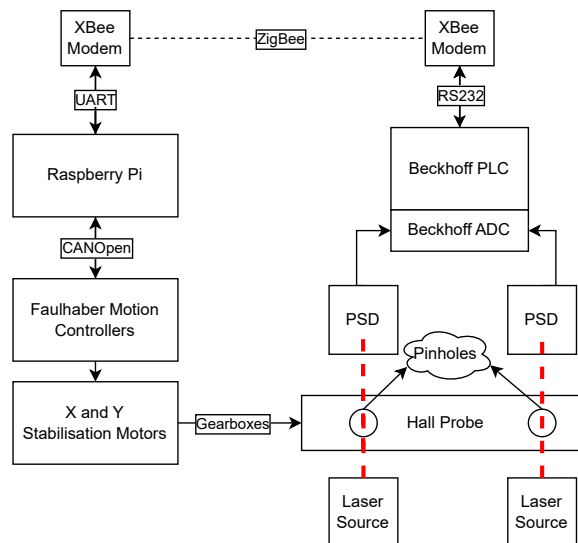


Figure 3.30: Block Diagram of the Implemented SAFALI System

3.4.4.1 PSDs Working Principle

The incident light from the laser source is detected by a pair of Two-Dimensional PSDs S5991-01 series from Hamamatsu [32] which translates the horizontal and vertical positions of the light spot to 2 analogue voltages. The PSDs are constructed with resistive layers placed onto a semiconductor substrate. The active area features a PN junction, which generates photocurrents when an incident light hits it. Electrodes positioned at opposite ends of the substrate facilitate the flow of the photocurrent and the magnitude of the current is inversely correlated with the distance between the light incident position and the respective electrode. Figure 3.31 illustrates a one-dimensional PSD where I_{X1} and I_{X2} represent the photocurrents induced at the output electrodes X_1 and X_2 , respectively.

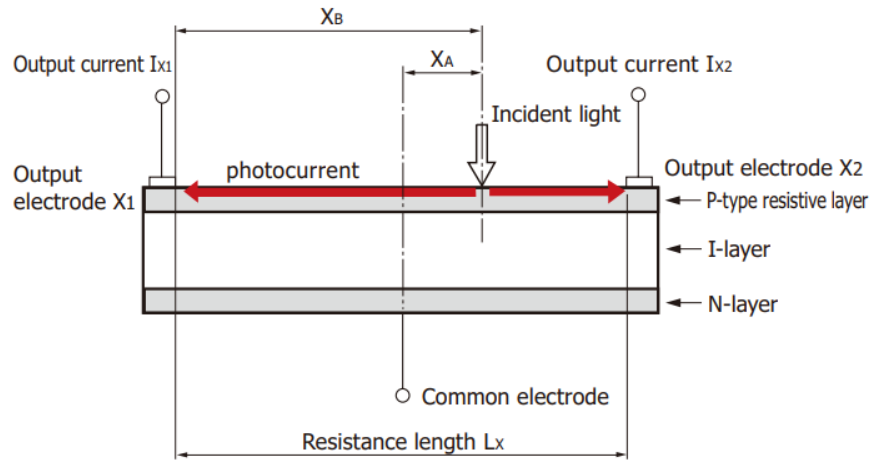


Figure 3.31: One-Dimensional PSD Cross-section [32]

Taking the centre of the PSD as the origin, from the data sheet, the current I_{X1} and I_{X2} are given by the relationships in Equations 3.3 and 3.4.

$$I_{X1} = \frac{\frac{L_X}{2} - X_A}{L_X} \times I_O \quad (3.3)$$

$$I_{X2} = \frac{\frac{L_X}{2} + X_A}{L_X} \times I_O \quad (3.4)$$

Where I_O is the summation of both photocurrents I_{X1} and I_{X2} . By rearranging equations 3.3 and 3.4, the distance X_A can be determined as shown in Equation 3.5.

$$X_A = \frac{L_X (I_{X2} - I_{X1})}{2 (I_{X2} + I_{X1})} \quad (3.5)$$

A two-dimensional PSD is constructed in a similar way with 2 stacked layers to provide 4 output electrodes where each 2 electrodes are dedicated for the detection of the incident light in both horizontal and vertical axes. A simplified diagram of the used two-dimensional PSD is shown in Figure 3.32.

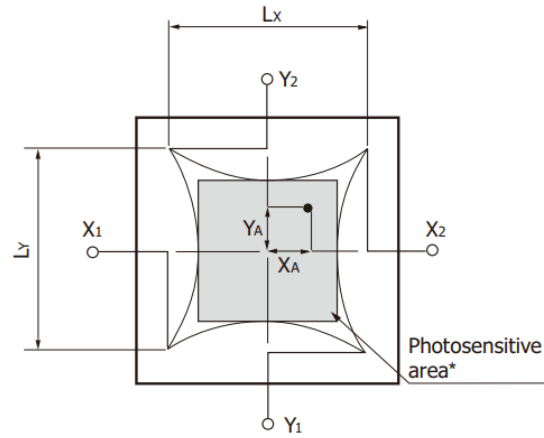


Figure 3.32: Simplified Diagram of the Two-Dimensional PSD [32]

By extension to the incident light position of a one-dimension PSD, the incident light position in a two-dimensions PSD in X and Y axes is given by Equations 3.6 and 3.7.

$$X_A = \frac{L_X}{2} \frac{(I_{X2} - I_{X1})}{(I_{X2} + I_{X1})} \quad (3.6)$$

$$Y_A = \frac{L_Y}{2} \frac{(I_{Y2} - I_{Y1})}{(I_{Y2} + I_{Y1})} \quad (3.7)$$

Where Y_A is the distance of the incident light from the centre of the PSD in the Y -axis, and I_{Y1} and I_{Y2} are the photocurrents generated by incident light in the Y axis. Figure 3.33 illustrates two cases where the incident light indicates the Hall probe holder is aligned and when a displacement error is present.

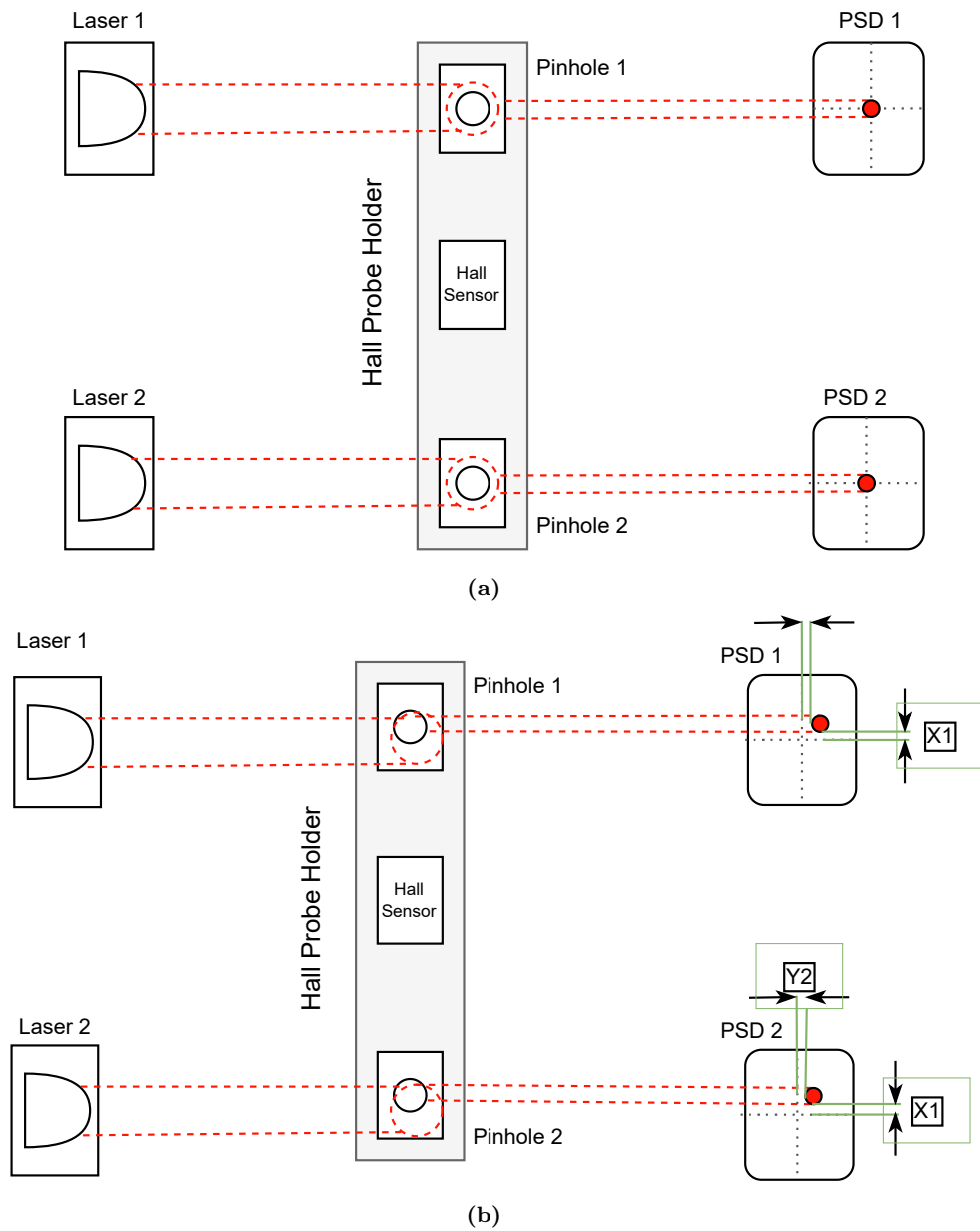


Figure 3.33: (a). Incident Light on the PSDs When Probe is Aligned
 (b). Incident Light on the PSDs When a Displacement error is Present in the Probe Holder Position

3.4.4.2 Position Feedback Loop Overview and Performance

The PSD signals are digitised using a Beckhoff EL3702 [33] 16-bit precision Analogue-to-Digital Converter (ADC) card at a sampling frequency of 1KHz. The ADC values are filtered with a moving average filter to reduce the noise from the PSDs and the position of the incident light from the laser beams is calculated locally on a Beckhoff PLC using Equations 3.8, 3.9 and 3.10 for the horizontal, vertical and roll angle respectively.

$$X = \frac{X_1 + X_2}{2} \quad (3.8)$$

$$Y = \frac{Y_1 + Y_2}{2} \quad (3.9)$$

$$\alpha = \tan^{-1} \left(\frac{Y_2 - Y_1}{X_2 - X_1} \right) \quad (3.10)$$

where,

- X_1 & Y_1 are the incident light position in x and y axes respectively from PSD 1
- X_2 & Y_2 are the incident light position in x and y axes respectively from PSD 2
- X & Y are the average position of the incident light in x and y axes respectively
- α is the roll angle of the Hall probe holder in degrees

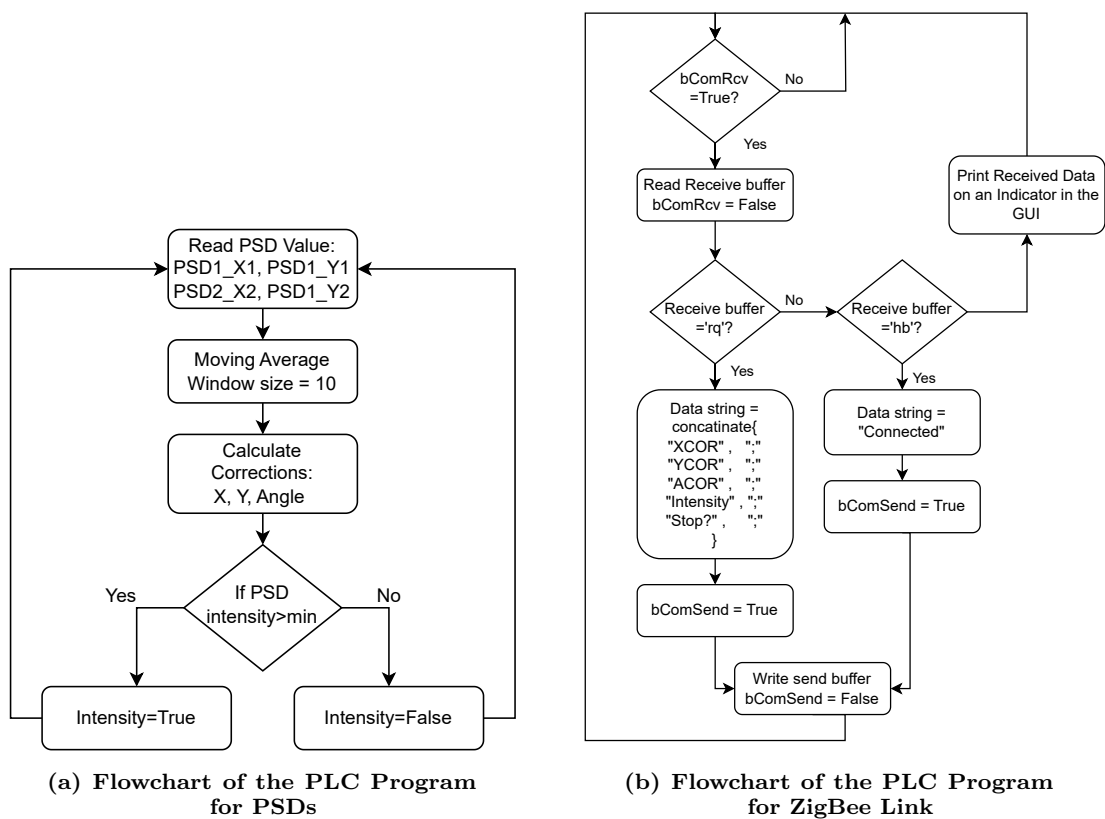


Figure 3.34: Flowchart of the PLC Programs Loops Running in Parallel

The correction values are continuously calculated according to the previously derived equations, as long as the PLC program is running and the Raspberry Pi can request correction data asynchronously via the ZigBee link by sending a predefined request character over the ZigBee link. The flowchart in Figure 3.34 explains the

PLC program sequences running in parallel for both the data acquisition of the PSD signals and loop that handles the ZigBee communication between the PLC and the Raspberry Pi.

The *bComRcv* flag is a special hardware flag that indicates the event of data received in the RS232 buffer and once this flag is True, the value in the buffer is read and the value is compared to the predefined values which are “*rq*” for correction data request and “*hb*” as a heartbeat. If “*hb*” is received, then the sting “*Connected*” is loaded into the hardware send buffer and a special hardware flag “*bComSend*” is set to trigger a send command on the RS232 card. On the other hand, if the value received is “*rq*”, the correction data is bundled as a long string and the same “*bComSend*” hardware flag is set and the data is sent over the RS232 to the ZigBee module. Finally, if the received character is not assigned to a defined process, then it is interpreted as a user feedback and the exact message is printed on an indicator on the GUI of the program. The correction data received by the Raspberry Pi is bundled as a long string of bytes separated by semicolon (;) along with other flag values that are integrated in the main program for other bench functions and an end of transmission predefined character byte. The bundled data format of the correction message from the PLC to the Raspberry Pi is shown in Figure 3.35.

X correction (in um) 6-bytes	;	Y correction (in um) 6-bytes	;	Angle correction (in mRad) 6-bytes	;	Intensity (Boolean) 1-byte	;	Stop Measurement Flag (Boolean) 1-Byte	;	Termination Character 1-Byte
------------------------------------	---	------------------------------------	---	--	---	----------------------------------	---	--	---	------------------------------------

Figure 3.35: Correction Message Bundled on the PLC to be Sent Over ZigBee

The ZigBee module used on the PLC side is the XBee S2C TH from Digi [34]. The ZigBee module allows for point-to-point data transfer wirelessly by receiving the data to be transmitted through serial interface, however, the PLC does not natively support serial interface in TTL levels. Hence, a custom PCB was designed and implemented to cater for the level shifting of signals and safely powering the ZigBee module and the complementary components. Figure 3.36 shows a block diagram of the correction data link between the PLC and the Raspberry Pi.

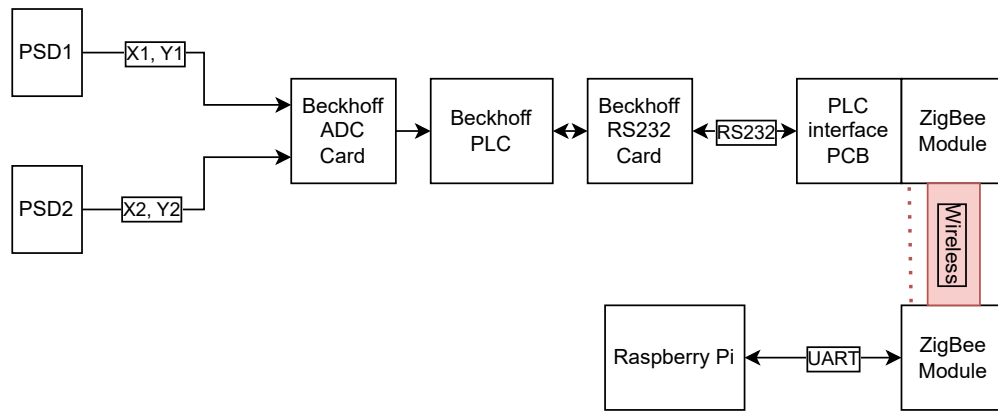


Figure 3.36: ZigBee Network Between the PLC and the Raspberry Pi

The PCB is powered from a two pole screw terminal block and the onboard voltage regulator used is the TPS70933DBVR [35] from Texas Instruments which is a low-dropout linear voltage regulator that is suitable for the task. The voltage regulator is powering both the ZigBee module and an RS232 driver, specifically the SN65C3221E [36] from Texas Instruments which handles the level shifting between TTL serial communication to the ZigBee module and RS232 voltage levels to the PLC while also providing protection against Electro Static Discharge (ESD). The ZigBee's reset pin is connected to a momentary push button for hard reset if necessary and the PCB contains a standard D-Type connector on the edge for a reliable connection between the PLC and RS232 driver. Schematics for the above mentioned electronics are shown in Figure 3.37.

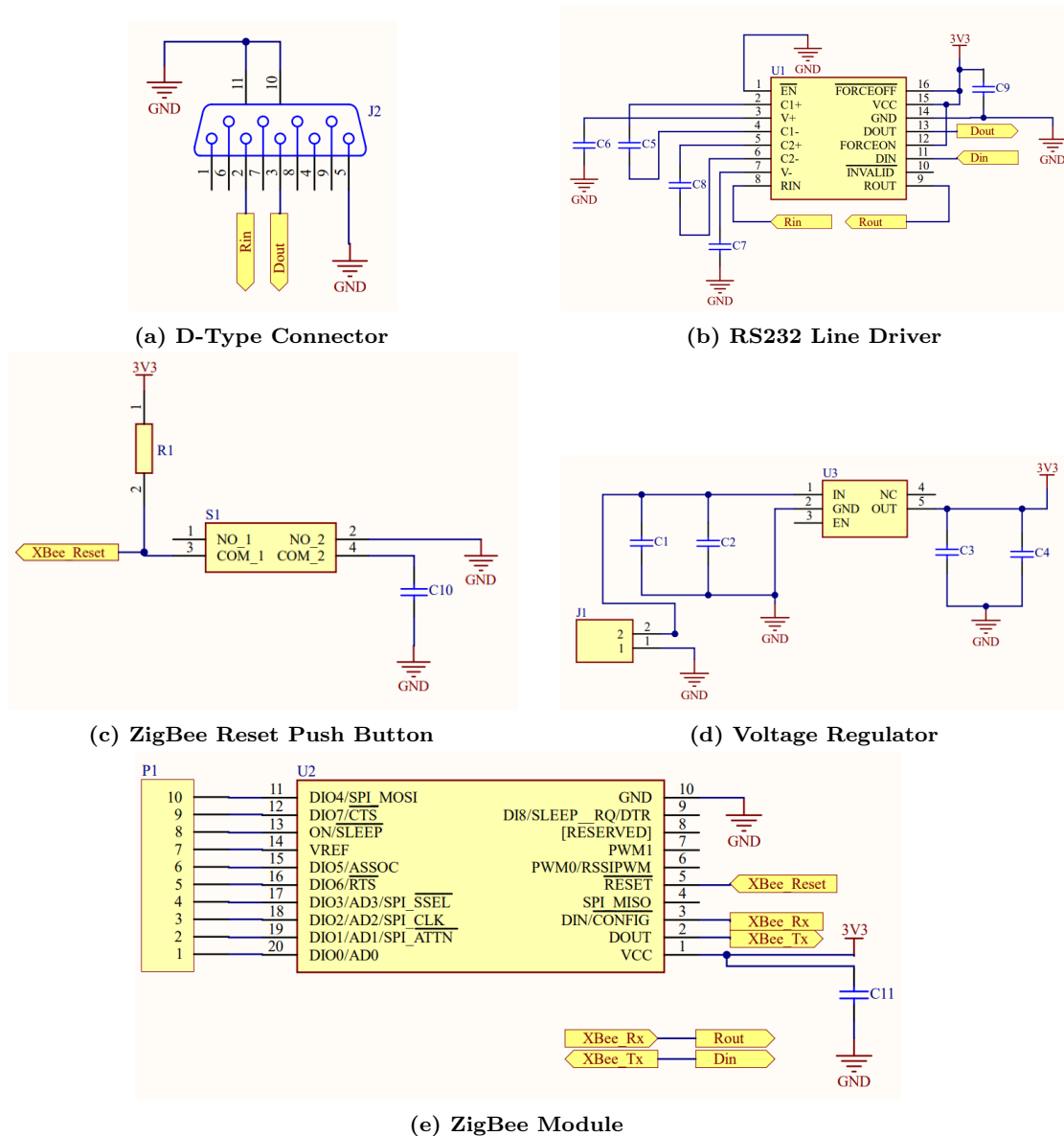


Figure 3.37: Schematics for the PLC Interface Circuitry

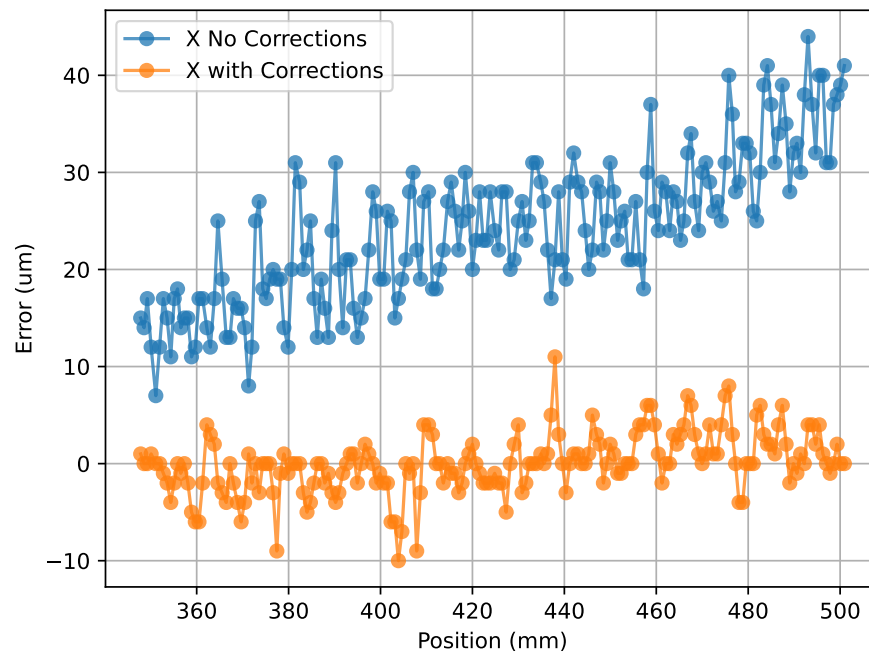
The ZigBee module on the Raspberry Pi end is the Xbee S2C from Digi which is the same one used on the PLC side, however, the package is SMD with an embedded PCB antenna in a compact package. This version of the module was preferred over the TH module due to the limitation of the space available for the electronics inside the vacuum chamber. Figure 3.38 shows the two ZigBee modules used.



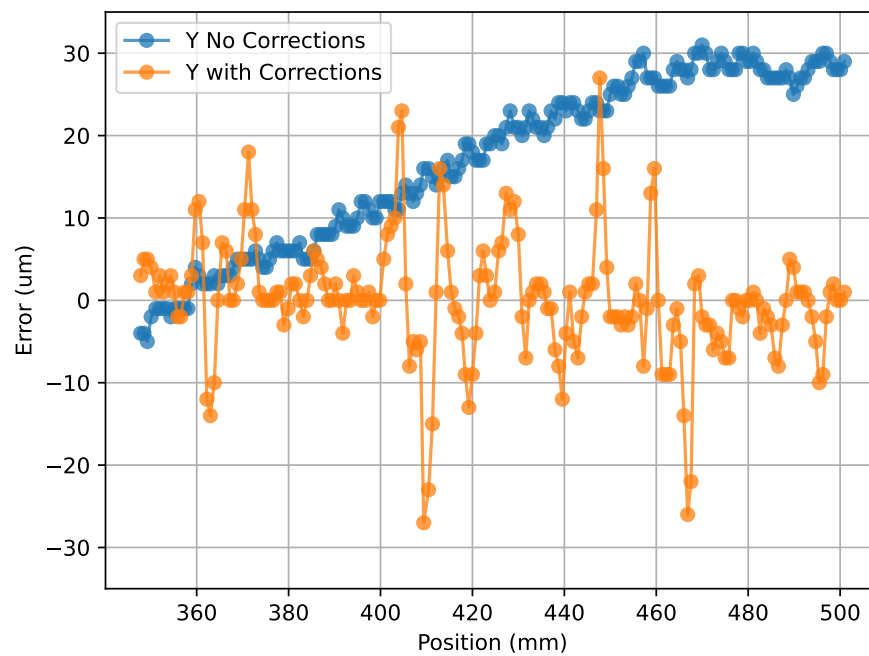
Figure 3.38: XBee S2C TH and XBee S2C SMD [34]

The corrections are then executed by sending the required movement commands over the implemented CANopen bus to the relevant motion controller to rectify the Hall probe holder position and by extension, the Hall probe sensor's position.

Due to the previously mentioned mechanical issues faced during the development of the bench, the Hall probe positioning system was tested only with a single stage of correction which is the y-axis. With the new Hall probe holder, the system can be tested with active position correction in both x and y axes. The test consisted of traversing the Hall probe along the rails once with the position correction loop inactive, and once with the loop active to highlight the magnitude of the Hall probe positional error in both cases. Figure 3.39 illustrates the positional errors of the Hall probe holder with and without the feedback system.



(a) Probe Positional System X-axis Performance



(b) Probe Positional System Y-axis Performance

Figure 3.39: The Closed-Loop vs Open-Loop Performance of the Hall Probe Positional System

The alignment procedure between the bench and the concrete blocks is done manually to the best of the available resources which inherently introduced slight

misalignments and parallelism errors between the different components. The laser and PSDs are installed on motorised apparatus which allow for the alignment procedure of the laser and PSD to be more accurate, stable and repeatable. Moreover, the table that houses the bench on its top is a mechanical “Breadboard” which is made from a large, extremely flat granite slab with several threaded insert embedded in it to fasten objects to it. The granite slab is then placed on a sturdy table with adjustable steel legs which were also used to align the test setup. The diagram in Figure 3.40 illustrates the test setup.

The position of the Hall probe when the correction loop is inactive drifts higher in magnitude the longer the bench is displaced. This is due to the accuracy of the alignment procedure between the table at which the bench is installed on and the positioning system lasers and PSDs concrete blocks on the side.

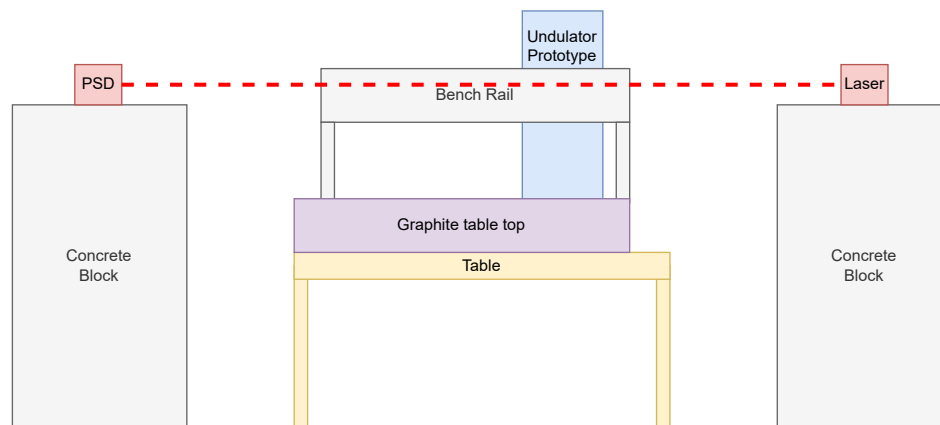


Figure 3.40: A Simplified Illustration of the Test Setup for the Hall Probe Positioning System

The positional errors of the Hall probe position in the x-axis is mainly within $\pm 10\mu\text{m}$ as shown in Figure 3.39a. On the other hand, the positional error in the y-axis is more than twice in magnitude in comparison to the x-axis. Moreover, the PSD errors in the y-axis are also worse when compared to the previously implemented bench shown in Figure 3.41.

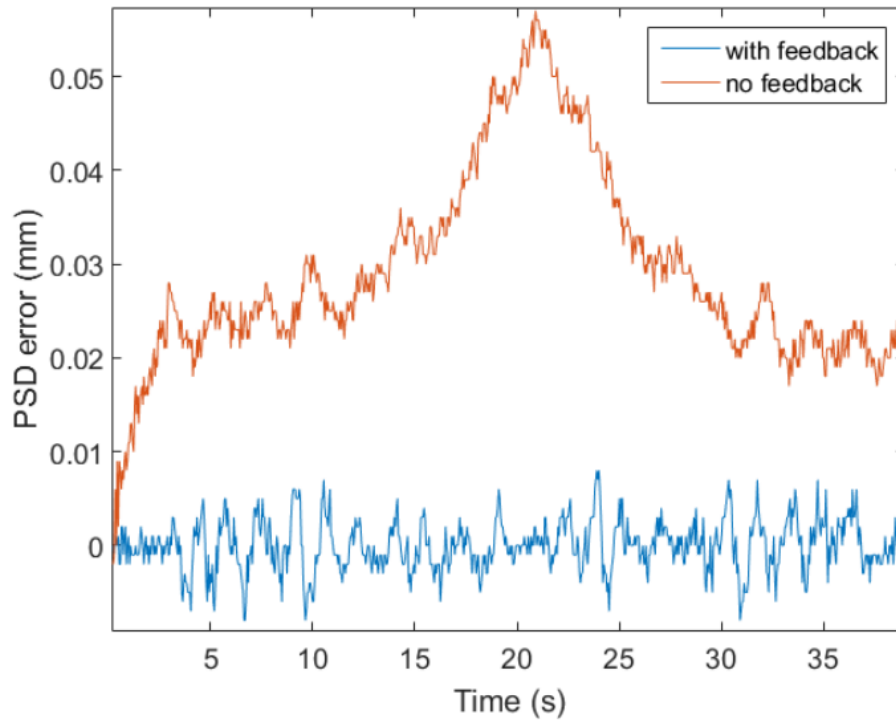


Figure 3.41: Stability of the Hall Probe Positioning System with and without Feedback [4]

When measuring an undulator, the vertical magnetic field, or the y-axis field of the device, is significantly susceptible to the slightest changes in that direction and a certain limit to position variations in the y-axis for an accurate measurement is required. This is not the case for the horizontal magnetic field, or the x-axis, of the undulator where the gradient of the magnetic field along x-axis is significantly lower than the y-axis in general.

During the evaluation process of the probe positioning system, it was noted that any slight corrections in the x-axis affects the probe's position in the y-axis momentarily by aggressive vibrations at the base of the fibre glass holder and these vibrations are further amplified at the tip. These vibrations are due to the physical nature of the designed mechanical bench holder and the mechanical system and the type of linear bearings used not being fully compatible with the new probe holder.

Therefore, to mitigate the vibrations and gain more stability in the y-axis position, the x-axis correction stage was omitted and the system was retested to quantify the stability gained in the feedback system. Figure 3.42 shows the closed-loop response for the Hall probe positioning system with y-axis corrections only.

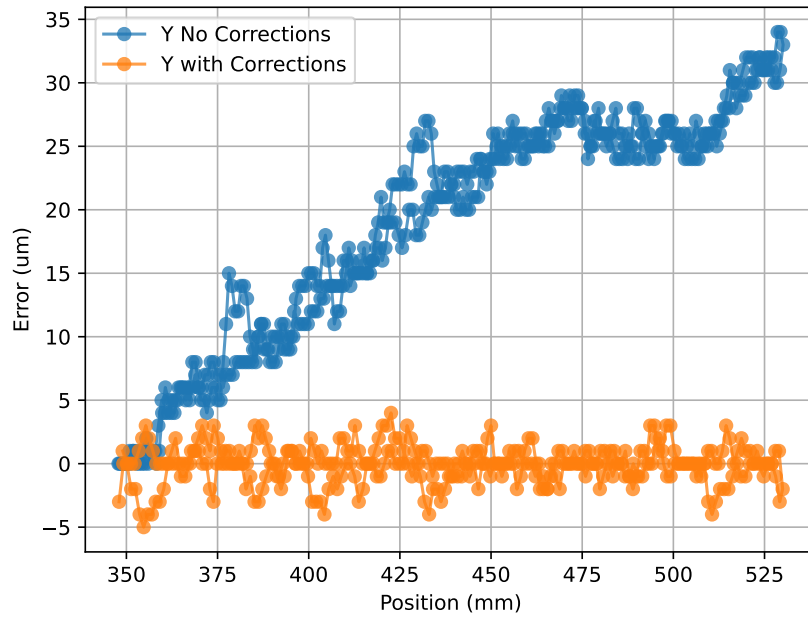


Figure 3.42: Probe Positional System Y-axis Performance - X-axis Correction is Disabled

The stability of the Hall probe position in the y-axis was improved significantly when compared to previous test conditions where the position was actively corrected in both x and y axes which confirms that the source of excessive vibration in the probe holder is the x-axis correction mechanical stage. Therefore, all further tests were performed without the x-axis correction for its effect on the stability of probe's position in the y-axis.

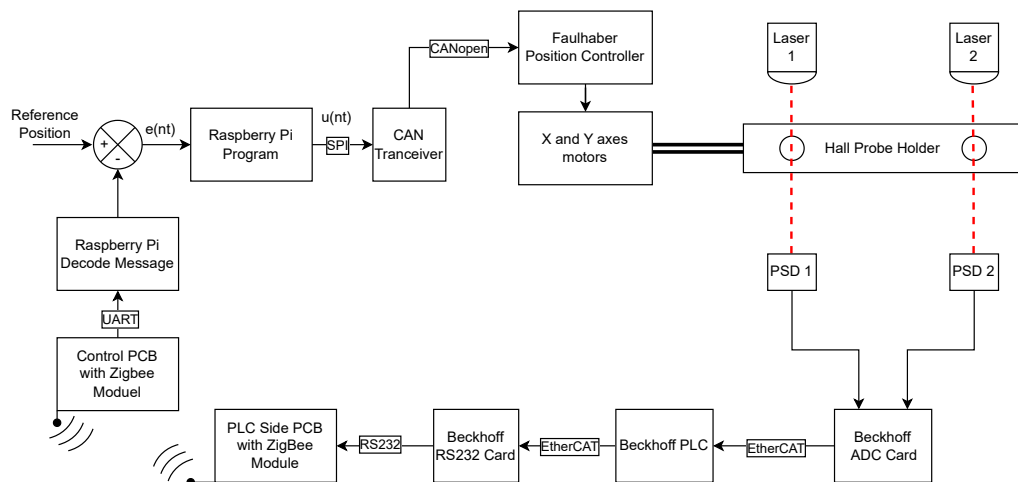


Figure 3.43: The Complete Feedback Loop of the Hall Probe Positioning System

The complete feedback loop for the Hall probe positioning system is shown in Figure 3.43 where $e(nt)$ is the error in probe position as a discrete time function and $u(nt)$ is the correction values communicated to Faulhaber motion controllers over CANopen.

The sampling frequency of the PSD feedback loop was measured during the Probe positional system stability tests. On average, the feedback loop sampling time is 106ms with 160ms and 101.9ms maximum and minimum sampling times respectively which corresponds to a mean, minimum and maximum sampling frequency of 9.4Hz, 6.25Hz and 9.8Hz respectively. The deviation in sampling frequency of the control loop is due to its nature, the wireless feedback link through the ZigBee network may introduce delays when transmitting data due to several factors such as signal strength, collisions and external interference sources from the environment around the bench which are inherent properties in any wireless communication system.

The sampling frequency of the feedback loop is however sufficient for the bench's purpose as the measuring velocity is usually set to 10mm/s which corresponds to approximately 10 probe position corrections every 10mm of displacement. The histogram in Figure 3.44 illustrates the distribution of the sampling time of the feedback loop.

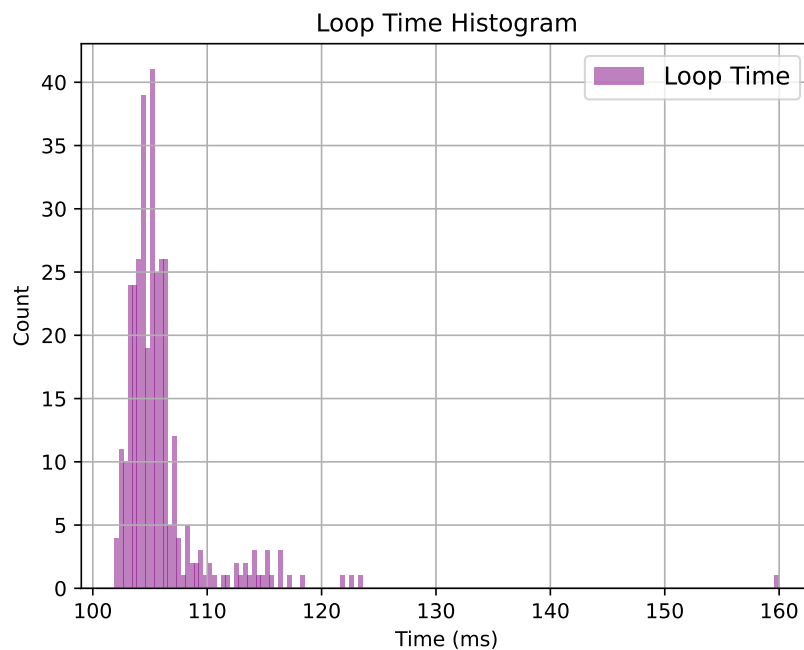


Figure 3.44: Feedback Loop Sampling Time Distribution

3.5 Chapter Summary

In this chapter, an overview of the μ MMB was given with the basic structure and the motivation and importance of the miniature mechanical design. The previously implemented bench was described in detail including the two main mechanical systems assemblies which are the Hall probe positioning system and the magnetic pole adjustment system, the limitations highlighted during the previous development period were also visited and justified, and the improvements on both the mechanical and electronic aspects of the bench were mentioned.

Finally, the commissioning process was carried out on the linear motor and the performance was tuned accordingly to a satisfactory level, while the Hall probe positioning system with the new holder was assembled and tested to quantify the performance of the feedback system as a whole.

Following the revision of the previous bench, several improvements to the bench's subsystems were planned. A summary of the work performed and improvements planned for implementation on the system are as listed below:

- Commission the measurement system after it has been out of order for 4 years.
- Improve on the Printed Circuit Board (PCB) design such that subsystems of the bench are grouped accordingly and can fit and travel freely along the mechanical bench inside a narrow vacuum chamber. This is done by using components with smaller footprints and Integrated Circuits (IC) that group the functionality of several ICs in one.
- Redesign and manufacture new PCBs to achieve the previous point.
- The lack of strength in the Hall probe holder was improved by the new stage which provides better physical support for the Hall probe sensor. The new stage requires testing and validation to evaluate the performance improvement on the overall measurement system.
- The power delivery to the bench's subsystems is planned to be improved such that a single power input is required while the different voltage levels needed for the subsystems are generated on-board.
- The user interface is to be improved by implementing a GUI on a PLC. This will allow the user to control the measurement bench without prior knowledge to the bench's subsystems.

In the next chapter, the rest of the electronic system on the bench is explained thoroughly and the improved implementation is also presented with the new PCB designs.

Chapter 4

Communication, Software & PCBs

In this chapter, the communication links between the different electronic modules is explained and the final implementation of the improved electronic systems is presented.

The μ MMB interfaces with a 3-axes Teslameter over an isolated USB link to trigger measurements and read measurement files to be saved locally on the on-board SD-card of the Raspberry Pi. In addition, a stand-alone EnDat communication link is required to interface with the EnDat absolute encoder which is used to indicate the position of the bench along an undulator; this is important for when the bench is operated in the absence of the 3-axes Teslameter.

The new power delivery system is presented along with the battery charging circuitry which could optionally power the bench from an on-board battery to eliminate the need for power cables inside the vacuum chamber during operation.

Moreover, the initialisation of the bench and the different software routines which allows the bench to perform various actions are briefly illustrated with a Graphical User Interface (GUI) implemented on the Beckhoff PLC via the ZigBee link between the PLC and the Raspberry Pi. The different manufactured PCBs are shown where a base PCB is fixed to the linear rails on the side of the vacuum chamber, and other system components plug into via dedicated sockets.

4.1 USB Connection to the Teslameter

The 3-axes Teslameter instrument [5] utilises 3 digital TTL signals which allows control over magnetic measurement when the Teslameter is intended to be used as a stand-alone instrument. The signals used are *Start/Stop*, *Busy* and *Error* where each signal can be interfaced via small connector on the side of the instrument. In this mode, the instrument starts a magnetic measurement when the *Start/Stop* signal is set high (5V) and stops the measurement when a falling edge is detected when

the signal is driven low or (0V); the *Busy* and *Error* signals indicate whether the instrument is busy acquiring magnetic data for a measurement event or is in an error state due to initialisation or hardware issue respectively. The magnetic measurement data is stored on an internal SD card where the naming of the measurement files follows an incremental integer convention starting from the number 1 and increases by 1 for each measurement file.

Operating the device using the 3 TTL signals has the limitation that the instrument's acquisition frequency among other parameters cannot be changed, and the measurement data file can only be extracted from the SD card by physically removing it from the instrument and the data files are copied manually to an external storage unit.

The Teslameter also supports operation over Universal Serial Bus (USB) which allows for a more versatile operation of the instrument where multiple setup operations and parameters can be accessed and changed easily. Also, the data files from measurement to be transferred directly to the device connected to it over the USB link and the files can be given meaningful titles making them more distinguishable. Another benefit from using USB as the primary communication bus is that error messages can provide more information about the type of error encountered internally in the instrument if an error occurs whereas in the TTL mode, the *Error* signal is pulled high when an error occurs which doesn't provide any detail about the error source.

Moreover, the Teslameter is interfaced directly with a Heidenhain absolute linear encoder through an M12 circular connector which is utilised to pair each magnetic measurement data point to an absolute encoder value; it is of utmost importance that every magnetic data point is paired with a position value from the absolute encoder to allow for accurate field mapping of the device under measurement. Hence, the USB mode of communication was preferred over the TTL mode for the operation it's versatility, reliability and robustness.

4.1.1 Overview of USB Link

The Raspberry Pi is the master of the USB link and sends a byte character to the Telsameter to achieve certain functions, Table 4.1 shows the different characters that can be communicated to the instrument and the response received for each command.

Raspberry Pi Commands		
Command Description	Character (ASCII/Decimal)	Teslameter Reply (ASCII/Decimal)
Change acquisition frequency to 1KHz	C/67	B/66

Change acquisition frequency to 2KHz	D/68	B/66
Change acquisition frequency to 4KHz	E/69	B/66
Change acquisition frequency to 8KHz	F/70	B/66
Heidenhain encoder position during measurement	G/71	Current encoder position (4-Bytes)
Heidenhain encoder position outside measurement	g/103	Current encoder position (4-Bytes)
Start magnetic field and encoder measurement procedure	I/73	I/73
Start memory acquisition	M/77	M/77
Stop magnetic field and encoder measurement procedure	J/74	J/74
Start transfer process of measurement data	K/75	Size of the measurement data(in Bytes)
Request 512 Bytes bulk transfer of calibrated magnetic field measurement data	S/83	Bulk data packet
Request 512 Bytes bulk transfer of uncalibrated magnetic field measurement data	s/115	Bulk data packet
Request Error code	*/42	2-bits error code

Table 4.1: Command List Implemented in the 3-axes Teslameter Instrument

Upon receiving the character “S” or “s”, which from Table 3.2 corresponds to a request of 512 Bytes bulk data transfer, the 3-axes Teslameter responds with 512 Bytes of data chunks that are 20-Bytes each in a predefined format as shown in Figure 4.1 and values are then decoded by the recipient device accordingly.

The X-field, Y-field and Z-field points indicate the magnetic field value at one point in space in the horizontal, vertical and longitudinal axes respectively. The 10-bit ambient temperature value is obtained from an internal temperature sensor inside the Teslameter’s package and the value is used in the internal calibration algorithm while the PT100 temperature value is obtained from the PT100 sensor integrated into the Hall probe sensor package [37].

X-Field Point (4-Bytes)	Y-Field Point (4-Bytes)	Z-Field Point (4-Bytes)	Ambient Temperature 10-bits	PT100 Temperature 22-bits	Encoder Value (4-Bytes)
----------------------------	----------------------------	----------------------------	-----------------------------------	---------------------------------	----------------------------

Figure 4.1: Chunk of Data Received from the Teslameter (20-Bytes)

The values in the data chunks are converted to more convenient format by the recipient device, the 10-bits ambient temperature value can be converted to degrees Celsius by multiplying with 0.0625; the PT100 and magnetic field values can be converted to degrees Celsius and Tesla as shown in Equations 4.1 and 4.2 respectively.

$$\text{PT100}(^{\circ}\text{C}) = (100(22\text{-bit value} \times 10^{-6}) - 3) + 22 \quad (4.1)$$

$$\text{Magnetic Field Value (T)} = (32\text{-bit value} \times 10^{-6}) - 3 \quad (4.2)$$

4.1.2 Implementation of the USB Link

The USB controller hardware is present in the Raspberry Pi Zero board and is interfaced to a micro-USB port located on the PCB. To ensure signal integrity of the Teslameter and to avoid introducing external noise source, a USB isolation circuit was implemented. On the control PCB, a micro-USB port is used to interface to the micro-USB port from the Raspberry Pi via male-to-male micro-USB cable. The USB isolation circuitry is realised via USB digital isolator, specifically the ADUM4160 from Analog Devices [38] and an isolated DC-DC converter, namely the ADUM5000 [39] also manufactured by Analog Devices to isolate the supply to each USB side from the main 5V rails of the control PCB. The schematics of the USB isolation circuitry is shown in Figure 4.2.

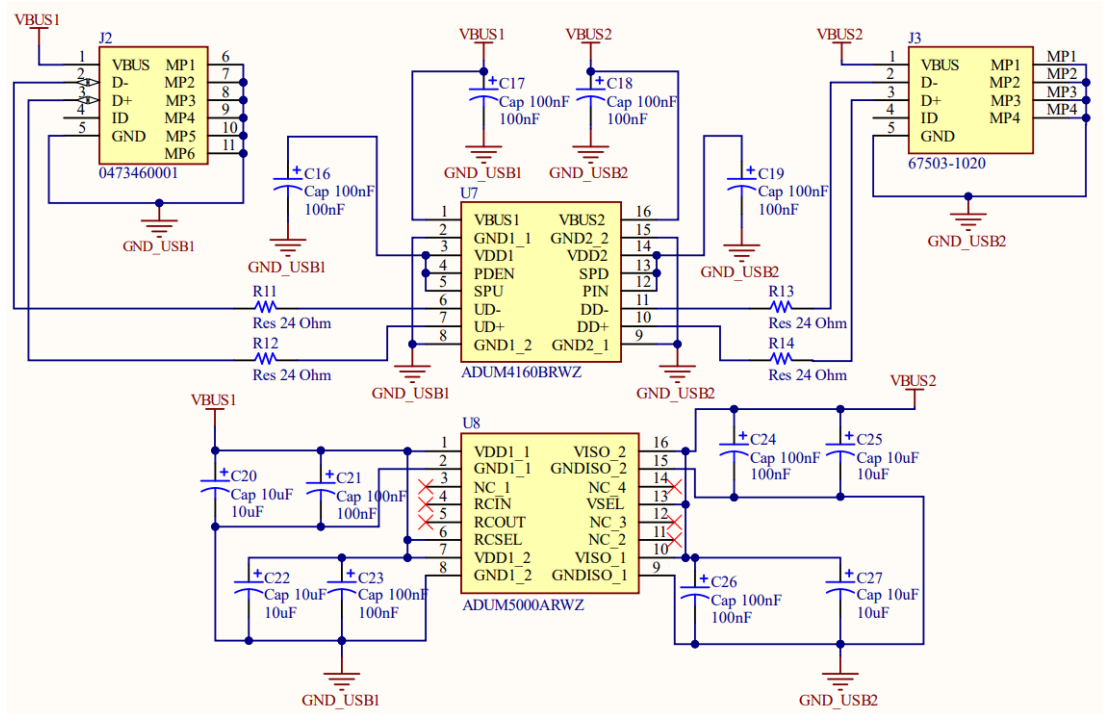


Figure 4.2: USB Isolation Schematics

A Python module titled *USBController.py* was previously developed which handles the initialisation and data transfer of the USB link between the Raspberry Pi and the Tesla. The module was built around the *PyUSB* package [40] which provides direct access to the USB controller hardware on-board of the Raspberry Pi. The module can operate on any device that is capable of executing Python scripts such as a PLC with Windows operating system which makes the module versatile by being independent from the controller's hardware whether it is a PLC or a computer running a Linux based operating system.

The *USBController.py* consists of a single class named *USBController*, with the predefined character commands shown in Table 4.1 and other relevant parameters. The methods for the declared class to communicate with the Tesla are:

`__init__()` is the default initialisation function in Python classes and performs the initial setup of the USB bus when a *USBController* object is created. First, the endpoint device is located through predefined VendorID and productID via utilising the tools built into the PyUSB package. A *ValueError* is raised if the device is not located

`send(msg)` is a generic send function that transmits a command character to the Tesla and is used to request the 512-Bytes data packets. If an error occurs in the transmission, a *ValueError* is raised.

send_cmd(cmd) is used to send the single character commands to the Teslameter and checks whether the correct acknowledgment was received after the command is transmitted. An error is raised if the incorrect acknowledgment is detected.

read_encoder(bMeasurement) is used to read the 32-bits value of the Heidenhain encoder from the Teslameter according to the *bMeasurement* boolean variable. A distinction is made using the *bMeasurement* flag as there are two memory locations where the Teslameter stores the encoder value in; this was done to prioritise pairing the encoder position with a magnetic field point over transmitting it over USB. Bit shift operation is performed on the 32-bit encoder position received to reflect the current value of the encoder counts.

read_error_code() is used to read error code from the Teslameter. A received “0” indicates no errors occurred, and any other value received is compared to a lookup table to decode the type of error. An error message is printed on the Console program to alert the user.

read_data(bRaw, bWrite) this method is used to receive the most recent measurement stored in the Teslameter’s internal memory bank, converts the data to .csv format, and saves the values received according to the value of the boolean flag *bWrite*. If *bWrite* is False, the values are returned to variable used to call the method in the program or is ignored if no variable was assigned. The boolean flag *bRaw* indicates whether the raw or the internally calibrated magnetic field values are transmitted by the Teslameter.

read_data_light_binary(bRaw, f, v, i) this method performs a similar task to the *read_data(bRaw, bWrite)* method with few distinctions. Both raw and calibrated magnetic field values can be obtained from the Teslameter, however, this method saves the values in binary file format (*.Bin*) and is used in the main magnetic measurement routine due to its fast execution time. Variables *f*, *v* and *i* indicate the acquisition frequency of the instrument, the velocity of the measurement performed and the current iteration of the measurement if multiple measurements were requested in the main program of the bench.

4.2 EnDat Communication Link

The encoder used to detect the longitudinal position of the bench is the *LIC411* [41] which is an absolute linear encoder reading head from Heidenhain. The reading head acquires the position data optically from a separate strip and the combination of the reading head and the strip dictates the accuracy and precision of the position values obtained from the encoder. The interface to the encoder is through EnDat [1]

bus which is a serial, digital bidirectional interface for position encoder developed by Heidenhain. An overview of the signals and basic components in the EnDat interface is shown in Figure 4.3

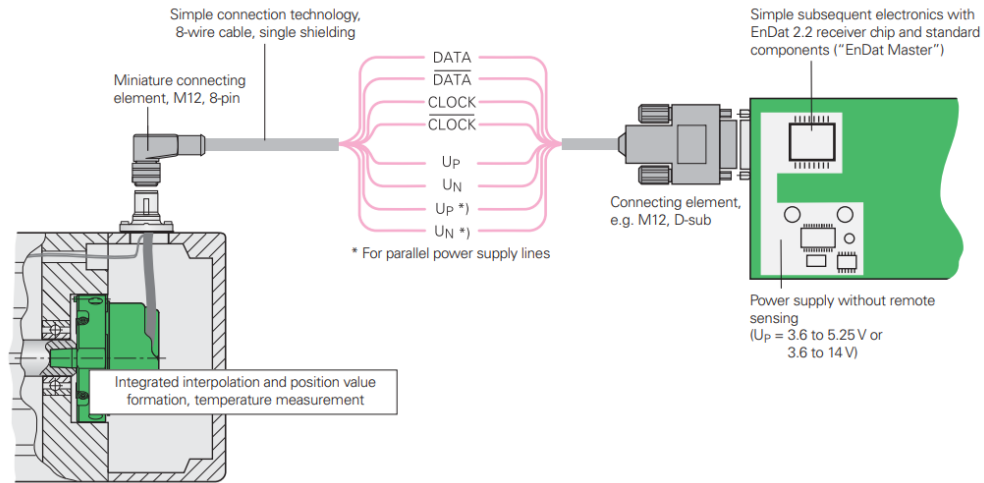


Figure 4.3: Overview of the Signals and Components of the EnDat Interface

The data transmission between an EnDat master implemented on a PLC or an embedded system and the target encoder is defined through dedicated parameters named *Mode Commands* which are constructed of 6-bits. The mode is communicated to the from the master device to the encoder to define the data format to be sent by the encoder; the 6-bit commands are divided into 3-bits to define the mode command followed by the inverted version of the same 3-bits mode command, this is done to as a precautionary procedure to add redundancy to the mode command. Table 4.2 illustrate the mode commands for EnDat communication protocol.

No.	Mode Command	Mode Bits					
		$M2$	$M1$	$M0$	$\overline{M2}$	$\overline{M1}$	$\overline{M0}$
1	Encoder Send Position Values	0	0	0	1	1	1
2	Selection of memory area	0	0	1	1	1	0
3	Encoder receive parameters	0	1	1	1	0	0
4	Encoder send parameters	1	0	0	0	1	1
5	Encoder receive reset	1	0	1	0	1	0
6	Encoder send test values	0	1	0	1	0	1
7	Encoder receive test command	1	1	0	0	0	1

Table 4.2: EnDat Mode Command Set as Defined by the Standard [1]

Once the mode command is sent by the master, the corresponding reply is transmitted by the encoder as a sequence of bits transmitted according to a clock

signal provided by the master (i.e. 1 bit per clock cycle) and a Cyclic Redundancy Check (CRC) is attached to the data. An example of encoder position read operation including the clock, data and frame format is illustrated in Figure 4.4.

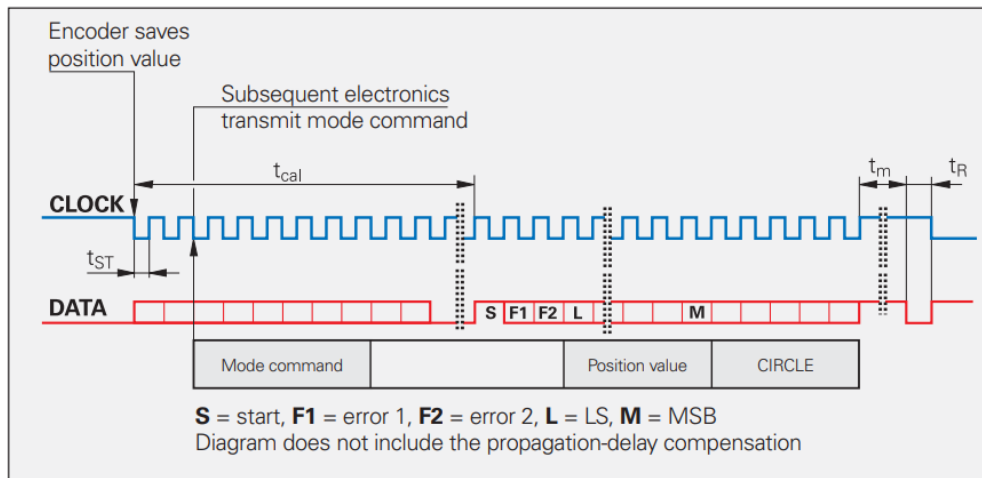


Figure 4.4: EnDat2.2 Data Transmission of Position Values and Timing Diagram

Internal parameters stored in the encoder can be accessed by the master via sending mode command *Selection of memory Area* to the encoder along with Memory Range Select (MRS) code to specify the address of the required parameter to be obtained. Following that, the encoder is instructed to send the parameter data defined by the MRS by sending mode command *Encoder send parameters* at which the encoder replies with the data as per the clock signal supplied by the master.

Initialisation process of the encoder by the master of the EnDat interface is shown in Figure 4.5 as per the recommendation of the implementation guide [42] provided by the manufacturer. Upon starting the system, the master sends a reset mode command to perform a local reset on the encoder, this is followed by mode command *Selection of memory area* with the MRS corresponding to the memory location of the error registers and any errors are cleared if any are found. The error registers are then read to check for any errors that occurred after the error register is cleared. Three other parameters are also read and following that, the mode command is changed to *Encoder send position values* such that the encoder is set to continuously read and store the encoder position where it is available upon request.

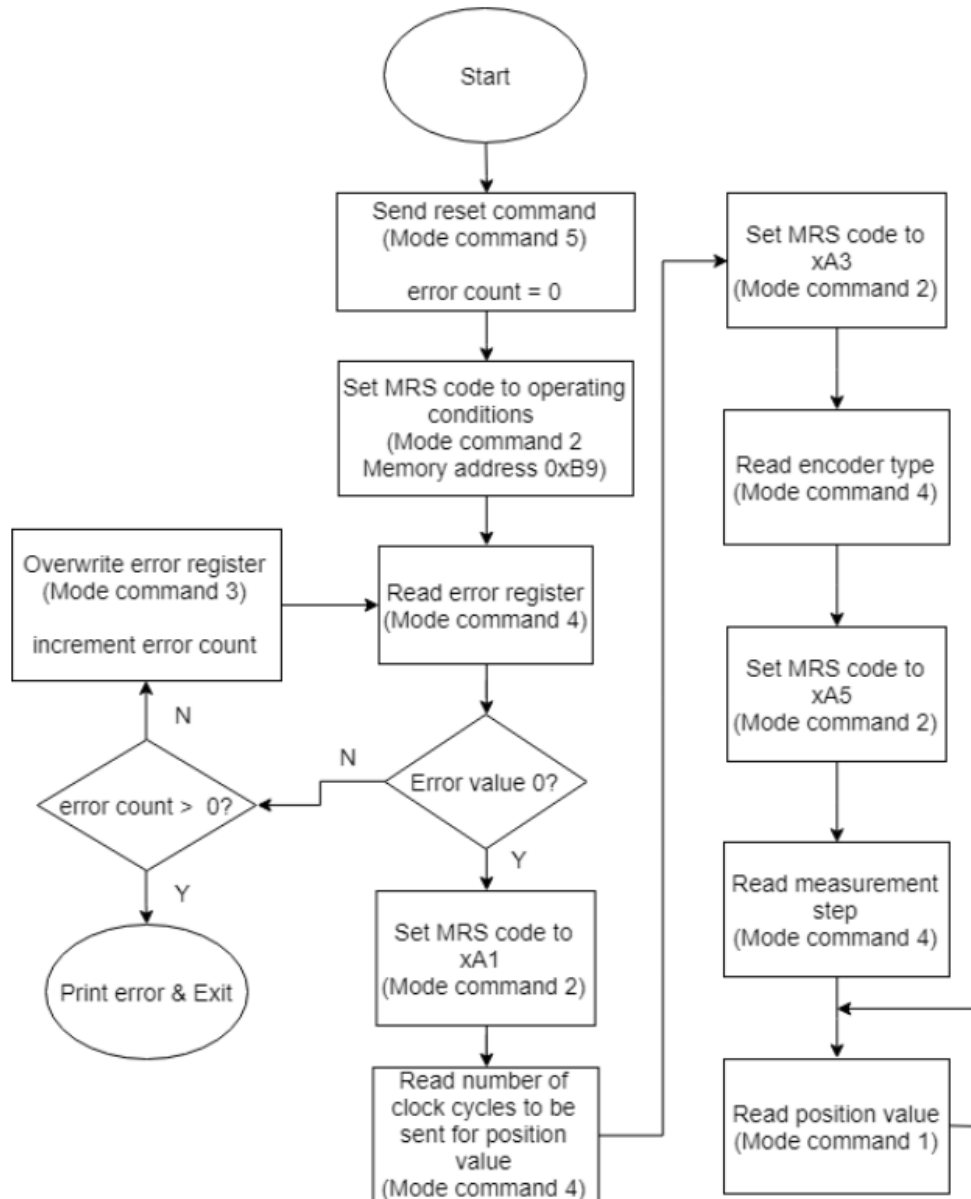


Figure 4.5: EnDat Interface Initialisation Process [4]

4.2.1 Implementation of EnDat

In normal operation of the μ MMB, the linear encoder head is interfaced to the Teslameter for magnetic data points to be paired with a physical encoder position during measurement. However, in the case of operating the bench in the absence of the Teslameter, a separate EnDat interface was previously developed [4] to allow for position data to be read by the Raspberry Pi through SPI bus.

The Pi has several SPI modules in the SoC, however, only the main SPI peripheral fully supports the protocol purely in hardware. The main SPI peripheral (or SPI1) is also assigned to interface with the CAN controller, and it is critical to have SPI1 purely dedicated to the CAN bus as it is the main communication bus to the 9 motion

controllers. Hence, a slight change was made in implementation of the EnDat by using a separate SPI controller on the Raspberry Pi (SPI2) which is also called auxiliary SPI as the hardware is generic and is shared with another serial interface (UART) on the SoC package [30]. This way, SPI1 is purely dedicated to the CAN bus and the auxiliary SPI2 can be used when needed for the EnDat interface.

The EnDat master is implemented in on a dedicated microcontroller, namely the ATmega328p [43]. The interface was developed in C programming language to perform the process illustrated in Figure 4.5. The encode position can be sent to the the Raspberry Pi asynchronously via SPI request, the request triggers an internal interrupt flag and the ATmega and the encoder value is sent to the Pi via SPI.

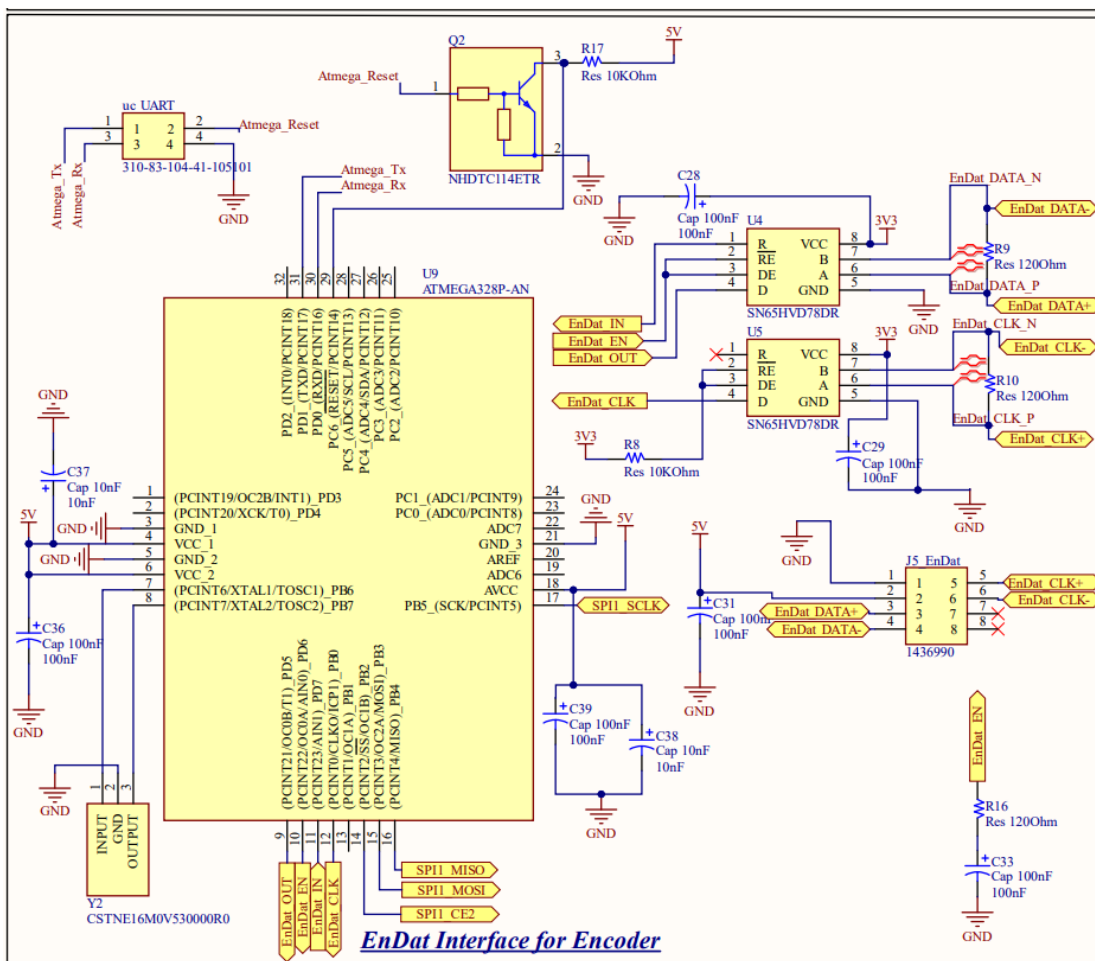


Figure 4.6: Schematics of the EnDat Interface Circuitry and Connector

The hardware layer for the EnDat interfaced is based on the hardware layer of RS485 protocol, therefore, two MAX485 RS485 transceivers from Maxim Integrated [44] were used, one is used transfer data and the other is used to transfer the clock signal differentially from the Heidenhain linear encoder to the EnDat master the ATmega328. The signals are carried via 8-pin M12 connector which interfaces with the shielded cable from the encode to carry power, ground, data and clock signals.

The SPI bus lines Master-Out-Slave-In (MOSI), Master-In-Slave-Out (MISO), Chip Select (CS) between the Raspberry Pi and the ATmega328 are implemented on a PCB where the PCB contains most of the communication and control electronics. Schematics of the implemented electronics system is shown in Figure 4.6, a 120Ω resistor is used as a terminating resistor as is advised by the data sheet along with decoupling capacitors for optimum power delivery to the ICs. The main clock to the ATmega328 is supplied through a 16MHz ceramic clock oscillator [45] with integrated load capacitors for compact design.

A Bipolar Junction Transistor (BJT) was used to drive a reset signal from the Raspberry Pi to the reset pin of the ATmega328 to allow for rest of the master EnDat through the main bench software implemented on the Raspberry Pi. The performance of the implemented EnDat interface was tested previously and was performing within acceptable limits for the bench, with 4MHz SPI clock, the 6-byte encoder position can be retrieved in approximately $510\mu\text{s}$

4.3 Printed Circuit Boards

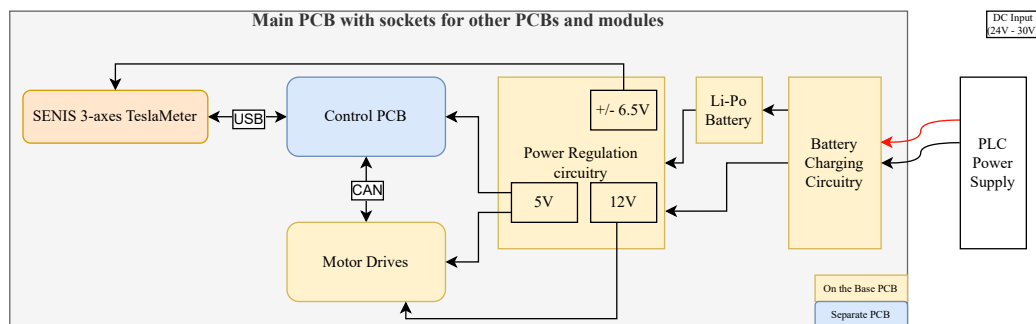


Figure 4.7: Block Diagram of the Electronic System

The implementation of the μMMB is focused on modularity, accessibility and ease of repair in case of a hardware fault. This is done by implementing three Printed Circuit Boards (PCBs) to house all the electronics and subsystems of the bench. The PCBs are:

PLC Side PCB: This PCB is located next to the PLC station outside the main bench assembly and handles the interface between the RS232 from the PLC and the ZigBee module on the PLC side.

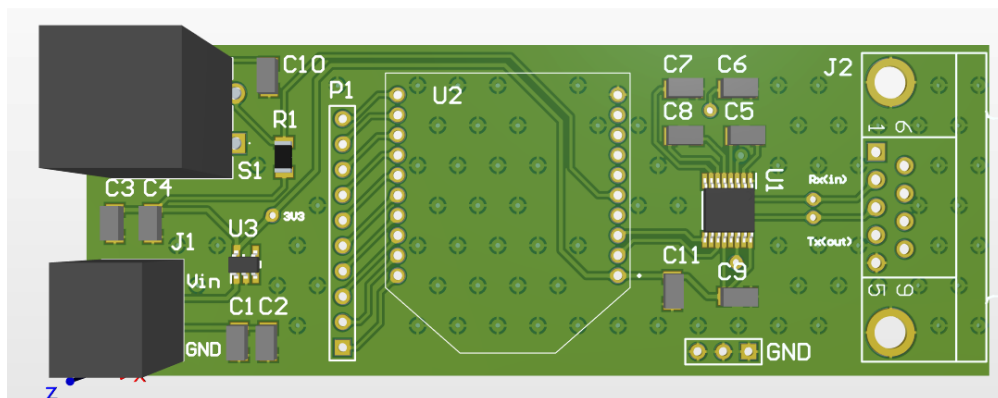
Base PCB: This PCB contains some electronic systems and ties the other system components such as the Teslameter and motion controllers together via slotted sockets and screws where they can be plugged and screwed in place respectively.

Control PCB: This PCB houses all the control electronics and communication circuitry necessary for the bench to operate. This PCB has a small footprint and is slotted into the Base PCB to connect to the motion controllers.

4.3.1 PLC side PCB

This PCB facilitate the communication between the PLC and the ZigBee module on the PLC side. An RS232 interface IC was used to translate the RS232 voltage levels from the Beckhoff RS232 card to a serial signal between 0 and 3.3V. The RS232 interface IC and the ZigBee module are powered from a low-noise Low-Dropout (LDO) 3.3V linear regulator that change the DC input from a generic PLC DC power supply between 15V and 30V to 3.3V. A reset push button for the ZigBee module which can be utilised to hard reset the module when a soft reset is not sufficient.

The manufactured PCB is 90mm by 33mm and is composed of 2-layers, both the top and the bottom layers are utilised as ground planes to increase the mass and surface area of the ground plane to mitigate the risk of noise interference from external sources in the operating environment. A 3D render and the actual manufactured PCB are shown in Figure 4.8. The power is supplied through a 2-pole terminal block and the connection to the RS232 PLC card is supplied through a D-type 9 connector.



(a) 3D Version



(b) Manufactured and Assembled

Figure 4.8: The 3D Version and the Manufactured Version of the PLC Side PCB

4.3.2 Base PCB

This PCB contains screw terminal and large pads to supply all the different components of the bench with power through several on-board DC-DC regulators all supplied from a single external PLC DC power supply. Optionally, power can be supplied to the different bench components from a single 4S Lithium-Polymer (LI-Po) battery that can be attached adjacent to the bench. This PCB also incorporates a battery charging IC for the ability to charge the battery from the PLC power supply input without the need to remove the battery and using an external charger. The battery charger used is the BQ24610 [46] from Texas Instruments which is a standalone battery charger with various safety features such as short circuit protection, over voltage protection for both input and battery voltage and others.

Due to the space limitation inside a vacuum chamber, this PCB was designed to act as a base plate that houses all the electronics including the Teslameter on-board and travels adjacent to the mechanical bench via the same frictionless linear bearings used for the mechanical bench that are located at each corner of the PCB (4 in total). Surface mount sockets were placed such that the control PCB and motion controller modules can be plugged into base PCB; this approach allows for different electronic controller to be utilised in the future to drive the motors of the bench and simplifies repair time for motion controllers as every module can be unplugged and tested separately and can be easily replaced in case of permanent damage.

The PCB dimensions are 490mm by 10mm which are strictly dictated by the vertical available space inside the vacuum chamber which is the 10mm width, The length, width, and height of the Teslameter is 154mm, 50mm and 42mm respectively, hence, for the instrument to fit inside the vacuum chamber and travel along with the bench, extra length in the base PCB is needed which justifies the length of 495mm of the base PCB. The designed and manufactured base PCB is shown in Figure 4.10.

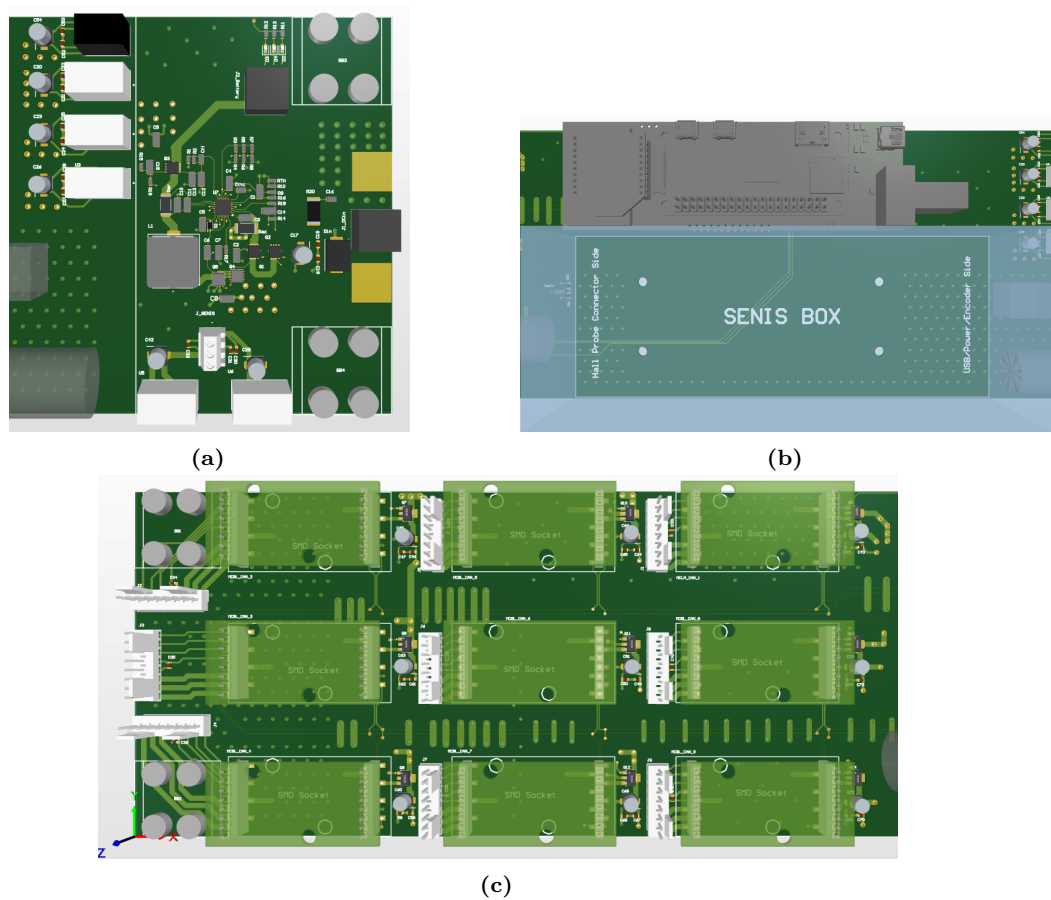


Figure 4.9: Base PCB Component Segmentation
 (a). Power Input, Battery Charging and Power Regulation Segment
 (b). Middle Segment of the Base PCB with the Control PCB (top grey PCB) and the Teslameter (bottom blue box)
 (c). Motion Controllers Segment

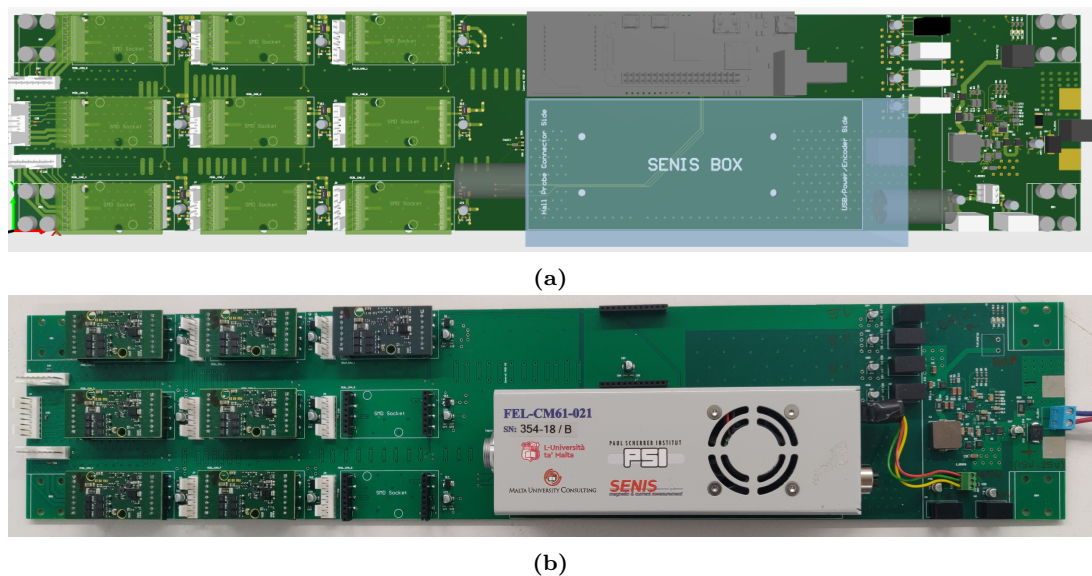


Figure 4.10: The 3D and Manufactured Base PCB
 (a). Designed Base PCB
 (b). Manufactured and Assembled Base PCB

4.3.2.1 Power Delivery and Regulators

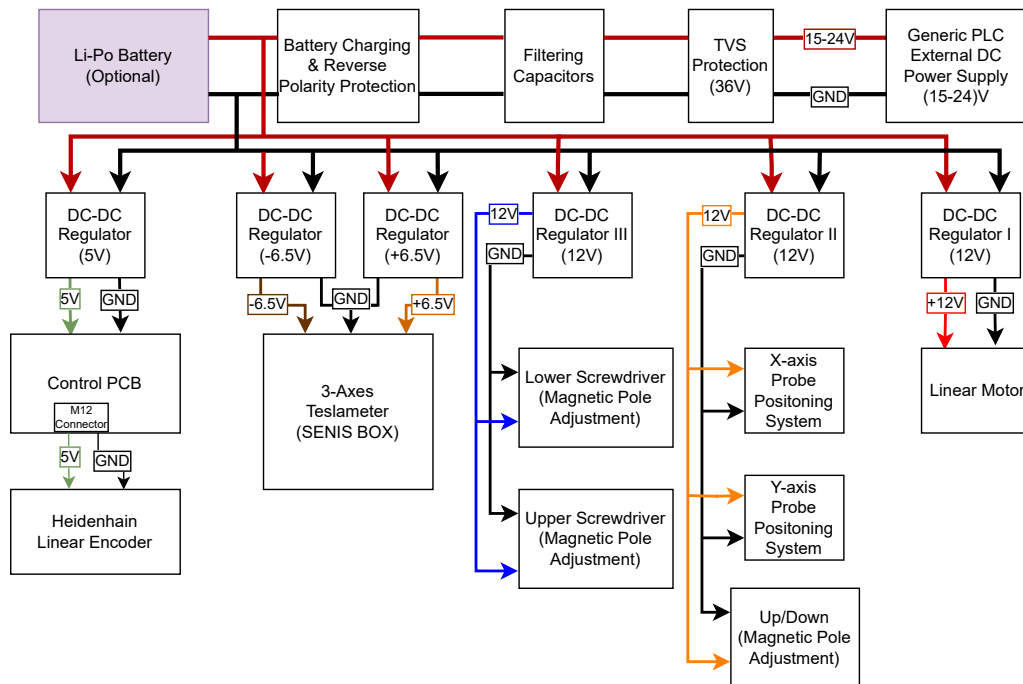


Figure 4.11: The Power Delivery Block Diagram of the μ MMB

Figure 4.11 illustrates the power delivery system of the bench. This approach removes reliance on an external power supply to power the motion controllers, Teslameter and other electronics by creating the voltage levels required with dedicated DC-to-DC voltage regulators.

The μ MMB is powered through an external PLC power supply as the main power input with voltage levels between 15V and 24V, the input is protected from voltage surges and transient changes via a Transient Voltage Suppressor (TVS) Diode, namely the SMC3K36CAHM3 [47] from Vishay General Semiconductors. Decoupling electrolytic and ceramic capacitor are also used for power filtering and to increase the stability of the input voltage. Optionally, the bench can also be powered through a 4S Li-Po battery that can be connected to the system through a 2-pole screw terminal block. A stand-alone battery charger circuitry is implemented on the base PCB to handle the charging process of the Li-Po battery if the battery option is utilised. The battery charger used is the BQ24610 [46] from Texas Instruments. The schematics of battery charging circuitry is included the Appendix 6.4.

In the absence of a battery in the system, the battery charger circuitry can be bypassed automatically, and the input voltage is fed directly into the different DC-DC voltage regulators to produce the different voltage levels needed. In total, three 12V regulators are used to power the motion controllers, specifically the TSR 2-24120 [48]

from Traco Power, one of the 12V regulators is responsible of solely powering the linear motor motion controller as it requires more power than the smaller Faulhaber motors and is continuously being used since it is the main motor translating the bench longitudinally.

A 5V regulator is used to power the Control PCB and it's subsystems such as the Heidenhain encoder accordingly. The regulator used is the TSRN 1-2450 [49] also supplied from Traco power. Finally, dual rail supply is needed to power the Teslameter, hence two TSR 2-2465 [50] were utilised to create the required $\pm 6.5V$. Power to the Teslameter is supplied from a 3-pole screw terminal and a short copper wire that is terminated with a male connector to plug into the power port of the instrument.

4.3.3 Control PCB

This PCB contains all the electronic system required to communicate with the different sub-systems and the control electronics including the Raspberry Pi main controller. The manufactured PCB dimension are 38mm by 120mm and is 4-layers where the top and bottom layers were used for component placement and routing layers, the second layer used as a solid ground plane, and the third layer is used as a 3.3V supply along with few tracks for the 5V electronics. The electronics systems of the control PCB are:

Raspberry Pi Zero W: The Raspberry Pi is plugged to a surface mount 40-pin socket located on the top layer.

Surface-mount ZigBee module: The ZigBee radio module is soldered on the top layer of the control PCB, PCB cut-outs were done to all layers underneath the antenna of the module for optimum antenna performance as advised by the data sheet of the product [34].

CAN controller/transceiver circuitry: The hardware of the CANopen bus is realised via the MCP25625 CAN controller and transceiver [29] which is placed on the top layer along with decoupling capacitors and other complementary components.

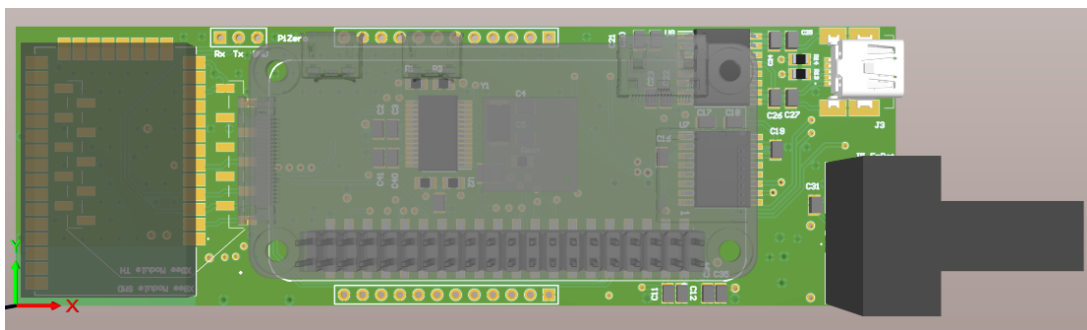
USB isolation circuitry: The USB isolation circuitry is composed of the ADUM5000 [39] and the ADUM4160 [38] which are an isolated DC-DC converter and USB isolation IC respectively. The Raspberry Pi interfaces to primary side of the isolation circuitry via short micro-UB to micro-USB cable from the USB port of the Pi to a micro-USB port located on the bottom layer of the control PCB. The Teslameter interfaces with the secondary side of the isolation circuitry via mini-USB to mini-USB cable to a mini-USB port located on the top layer of the control PCB.

EnDat interface circuitry: The Atmega328 along with the pair of RS485 transceivers are located on the bottom layer of the PCB. The M12 circular connector footprint is large however; it is through hole. Therefore, it was placed on the top layer where there is more available space while signals are routed to the connector using the bottom layer.

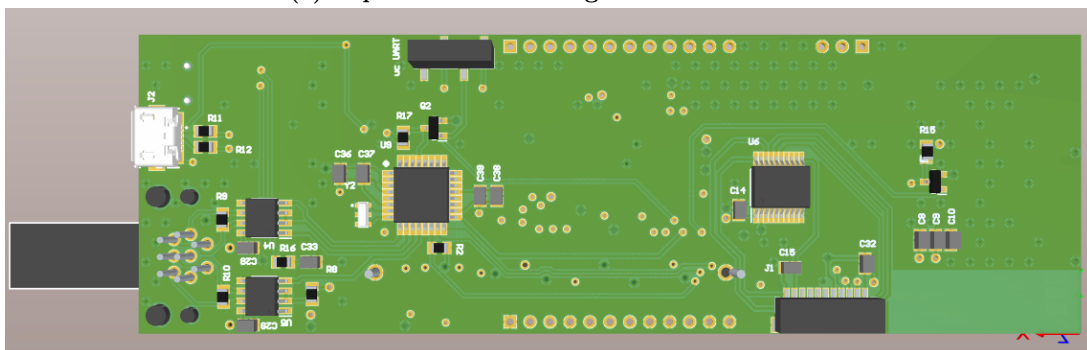
SPI isolation circuitry: The ADUM3151 [51] is an SPI isolation IC which was included in the electronic system as an optional choice for debugging the Teslameter. The SPI isolator and a miniature 8-pin female connector are placed on the bottom layer and can interface with an identical connector on the Teslameter to pass the SPI debug data and GPIO signals from the Raspberry Pi for the option to optionally operate the Teslameter in the previously mentioned TTL mode.

Edge pin connectors: Two 12-pin connector are placed on each long end of the control PCB to interface with the base PCB and connect the 5V power lines, CAN_H, CAN_L and several other digital signals to components placed on the base PCB.

The designed and manufactured control PCB is shown in Figures 4.12 and 4.13

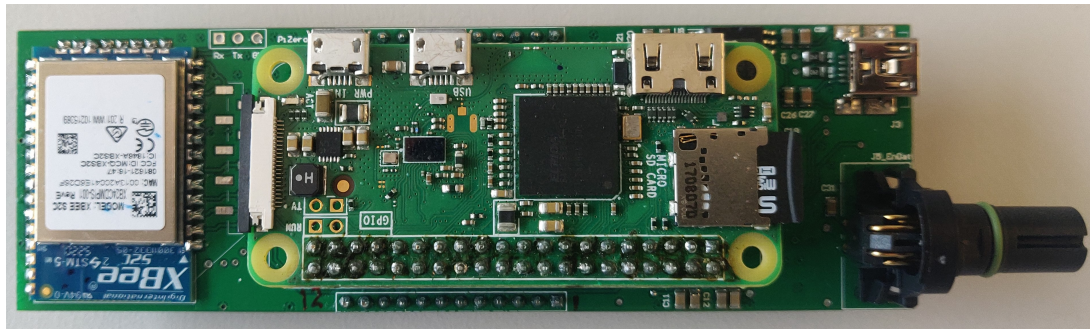


(a) Top View of the Designed Control PCB

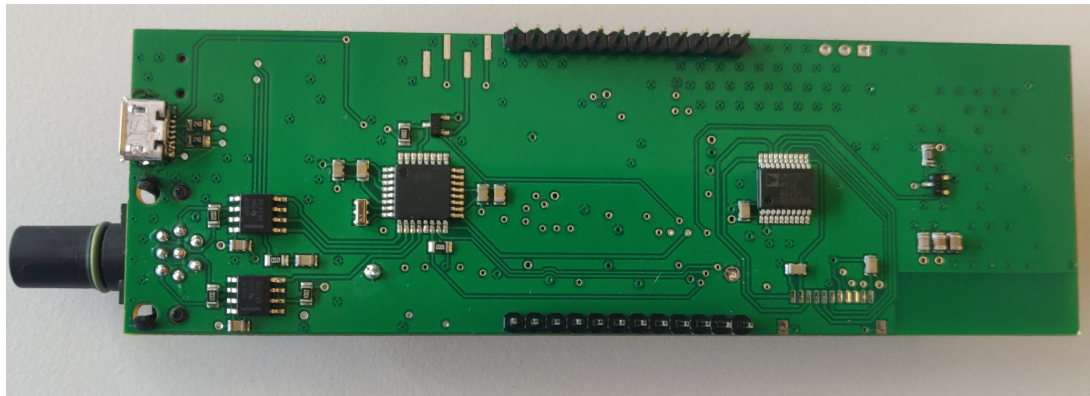


(b) Bottom View of the Designed Control PCB

Figure 4.12: The 3D Version of the Designed Base PCB



(a) Top View of the Manufactured Control PCB



(b) Bottom View of the Manufactured Control PCB

Figure 4.13: The 3D Version of the Designed Base PCB

4.4 Main μ MMB Program Flow

A flowchart of the main loop of the program is illustrated in Figure 4.14. The main program is constructed in a Python module *Bench* with one main class named *Measurement*. The class is initialised at the start of the main program script, several methods private to the class were implemented to perform the initialisation routines for the several bench components. The μ MMB initialisation process consists of the following steps:

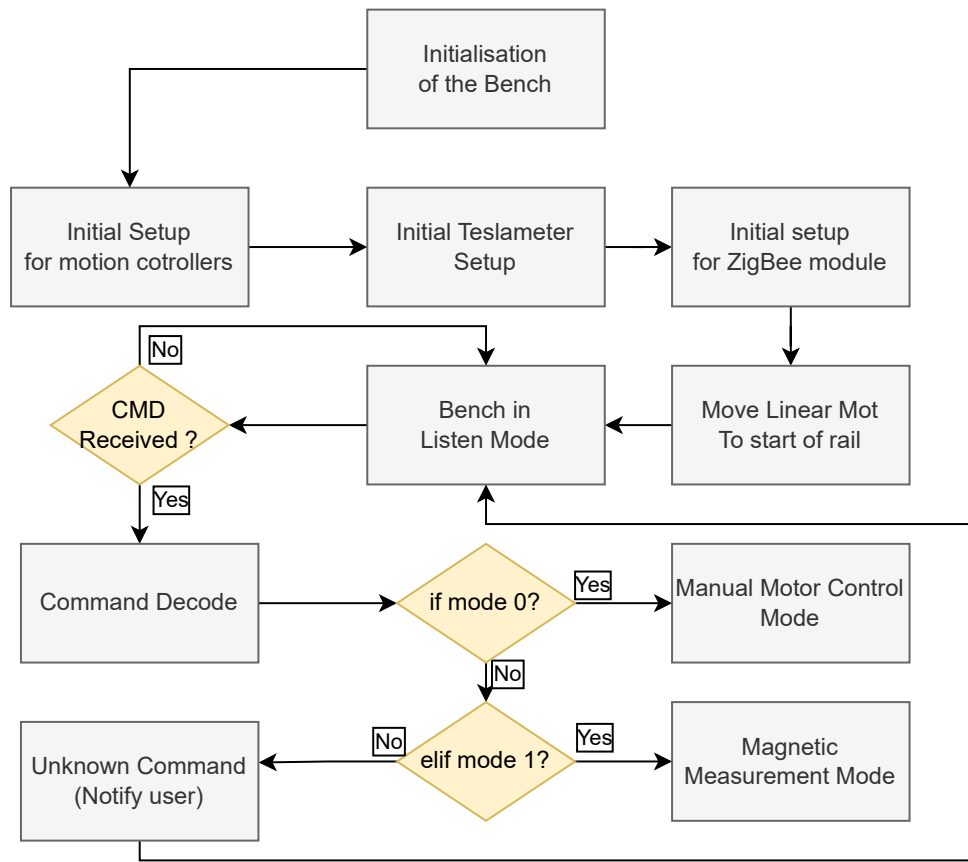


Figure 4.14: Main Loop of the μ MMB Program

Motion Controllers Initialisation: The 9 motion controllers of the bench are initialised and assigned a CAN_id each according to predefined id stored in the controllers. The probe positioning system initialisation consists of setting the upper/lower travel limits of each the horizontal and vertical stages, setting the controllers to *CSP* mode, and homing the motor to the lowest possible physical position for each stage. The homing procedure of the motors assumes that each stage of the probe positioning system is at the lowest possible physical position, this is done as a soft homing technique due to the lack of homing sensors integrated into the bench's structure.

Teslameter Setup: The USB connection to the instrument is initialised and the measurement frequency is set to 1KHz by default. In the absence of the instrument, an error is raised and the script goes through the end routine.

ZigBee Module Setup: Initially, a reset pulse is sent to the ZigBee module reset pin, following the reset, the serial connection is established and several parametric checks are performed such as serial connection test, voltage level at the

power pins of the module, and a connection test to the PLC side ZigBee module by a predefined heartbeat command.

Following the initialisation procedures, the linear motor, and consequently the bench, is moved to the start of the rail and the bench goes into *listen mode* where the ZigBee module is polled periodically to check if any instructions were received from the user operating the bench from the PLC station.

The bench remains in *listen mode* until the python script is terminated or instructions are received from the user. Custom commands formats were developed for the bench which are to be integrated into the Graphical-User-Interface (GUI) using indicators and active buttons. The commands format defines the behaviour of the bench and instruct the system accordingly, the operating modes are *Manual Motor Control Mode* and *Measurement Mode*.

Manual Mode Command Format from PLC										
0	;	CAN_id of motor	;	Distance to be travelled (in mm)	;	Asolute position = 1 Relative position = 0	;	Velocity (mm/s) linear motor only	;	\r

(a) Command Format for Manual Mode

Measurement Mode Command Format from PLC														
1	;	NC	;	Measurement Velocity (mm/s)	;	Start Position (absolute pos in mm)	;	Stop Position (absolute pos in mm)	;	Start now (start = 1)	;	Reptions (integer value)	;	\r

(b) Command Format for Measurement Mode

Figure 4.15: PLC Commands to Operate the Bench over the ZigBee Wireless Link

Manual Motor Control Mode: In this mode, the position of any motor defined at the initialisation stage can be altered. This is an especially useful feature to allow the user to properly align the pinholes on the Hall probe holder to the laser source and PSD path easily by integrating the command format to a button on the GUI. The command format for this mode is shown in Figure 4.15a, the motor to be jogged is defined with its CAN_id, and the distance specified in the command is passed to the motion controller with either a relative movement or an absolute position. the movement can be interrupted by sending any character from the PLC as a safety precaution.

Measurement Mode: In this mode, the bench performs a magnetic measurement by defining the velocity, start and stop positions, and how many iterations of measurement to perform in the received command. The command format for this mode is shown in Figure 4.15b, the measurement routine is executed once the command is fully received with full parameters. The bench is moved to the specified start position which is always an absolute position and is obtained from the Heidenhain encoder through the Teslameter USB interface.

Once the start position is reached, 50 corrections to the Hall probe positioning system are performed to ensure proper alignment with the lasers, magnetic measurement and data acquisition is triggered on the Teslameter then the bench travels to the specified end position in the specified velocity while actively correcting the Hall probe position. The bench is stopped upon reaching the stop position or when a stop measurement flag is received in the ZigBee correction frame, the measurement data is obtained from the Teslameter via USB and labelled accordingly, the label on each measurement contains a timestamp, the measurement order, acquisition frequency and velocity used to obtain the measurement as a reference for data analysis. The bench returns to *Listen Mode* and awaits further commands from the user if no repetition value was specified. A flow chart of the measurement routine is as shown in Figure 4.16.

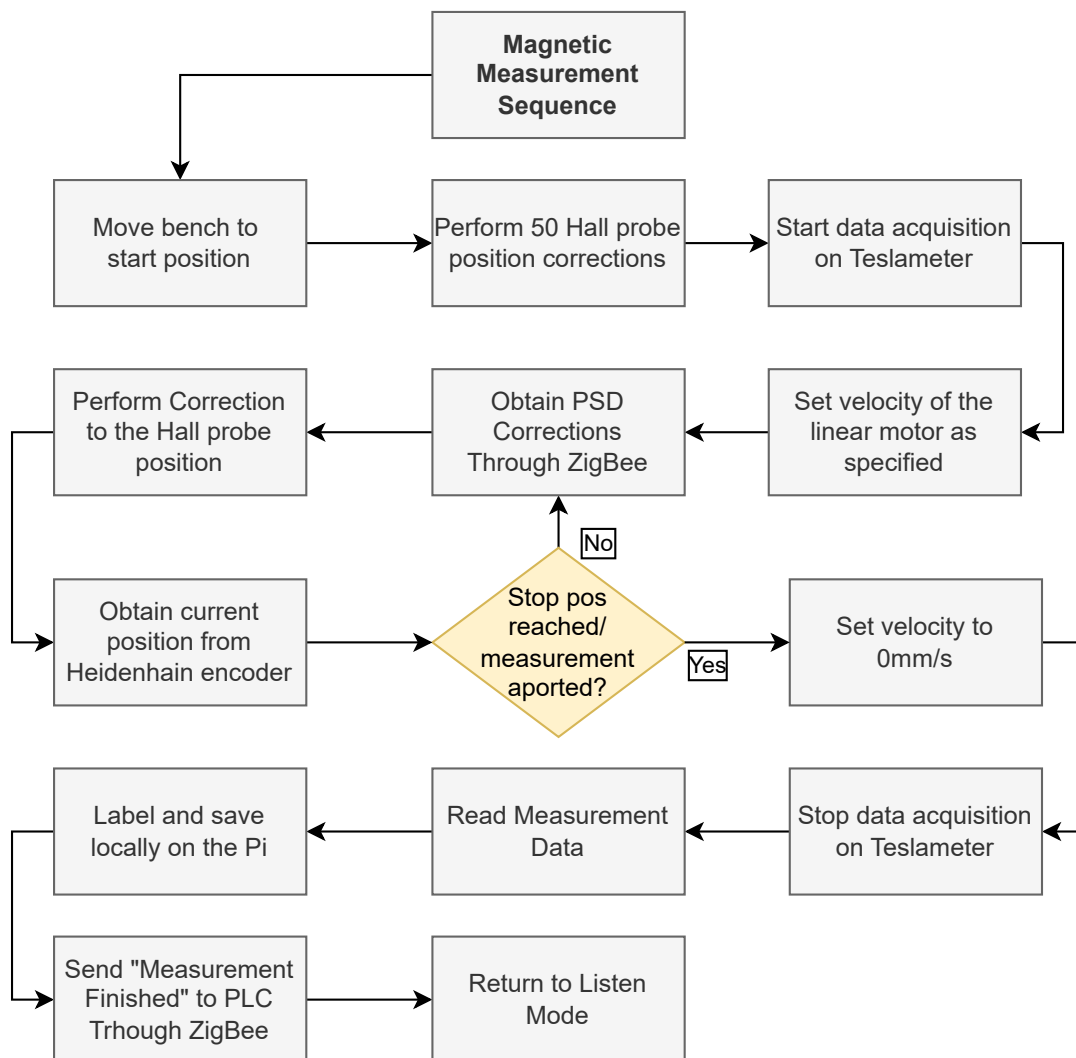


Figure 4.16: Flowchart of the Magnetic Measurement Mode

4.5 Chapter Summary

In this chapter, the USB link to the Teslameter was defined and the electronic hardware used to realise the bus is described. The interface to the Heidenhain encoder is explained along with the electronics involved to achieve the EnDat interface to the encoder in the absence of the Teslametr instrument.

The overall structure of the electronic system was illustrated in terms of the Printed Circuit Boards (PCBs) manufactured and how the different modules in the system were connected. Moreover, the power delivery system implemented on the base PCB was described and the different regulators to generate the required voltage levels for the different parts of the system were briefed.

Furthermore, the main software structure of the μ MMB is illustrated including the main two modes of operation which are *Manual Motor Control Mode* and the *Magnetic Measurement Mode* with a brief explanation to the routines performed in each mode.

In the next chapter, the described implemented system is tested to evaluate its performance in comparison to the previous version of the bench and the Teslameter as a stand-alone instrument. Also, the bench is used to characterise a prototype undulator with magnetic force compensation and the results are presented accordingly.

Chapter 5

Magnetic Measurements of the New Undulator

The test setup of the undulator prototype and magnetic measurement campaign using the implemented μ MMB is described. The performed tests are explained, and the results are presented and compared to the previously implemented version of the bench and the Teslameter as a stand-alone instrument. The prototype undulator with the force compensation magnets is characterised using the developed measurement system and the effect of the extra magnets on the field enhancing magnets is studied.

5.1 Measurement Setup

A 3D model of the μ MMB attached next to the prototype new undulator is illustrated in Figure 5.1.

Due to delays in the serial production of the new generation of undulators for the SLS2.0 upgrade, the first prototypes of the vacuum chambers with the integrated rails were delayed and could not be prepared for the testing phase of the bench. This resulted in the prototyped magnets to be assembled in an existing U-shaped frame with a custom bracket to allow the characterisation of the force compensation magnets without the vacuum chamber. Furthermore, the electronics of the bench were assembled on the base PCB and were placed in the proximity of the mechanical bench since the length of the rail where the bench is attached is not long enough to mount the PCB. The actual test setup is shown in Figure 5.2.

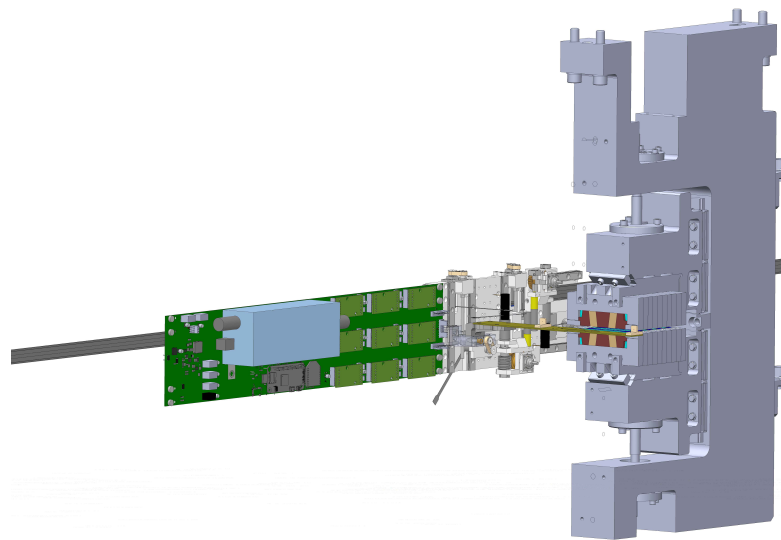


Figure 5.1: 3D Model of the Test Setup

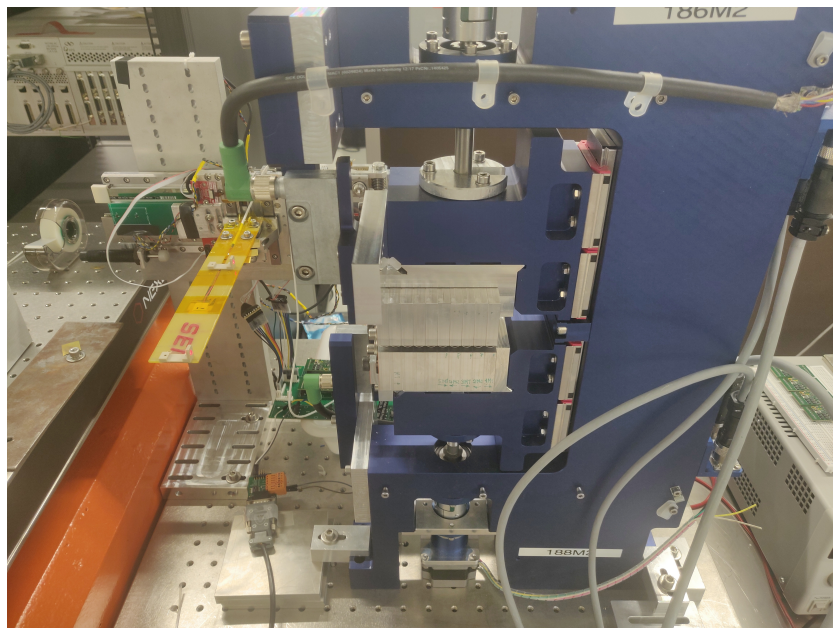


Figure 5.2: Actual Test Setup Used to Characterise the new Undulator Prototype

The bench is attached to the rail via hex bolts that screw into frictionless linear bearings at each corner of the bench. The rail is then attached to two L-shaped brackets, ensuring the bench's orientation aligns with its position when mounted on the vacuum chamber's rails. The undulator and the μ MMB assembly are fixed to a graphite table-top with mounting holes where hex bolts and aluminium spacers were used to firmly connect both setups to the slab. The slab is then placed on a rigid aluminium table with height adjustable feet to help in the alignment procedure of the

test setup. The block diagram in Figure 5.3 illustrates the full test setup including the lasers, PSDs, undulator, and the bench according to the described test apparatus.

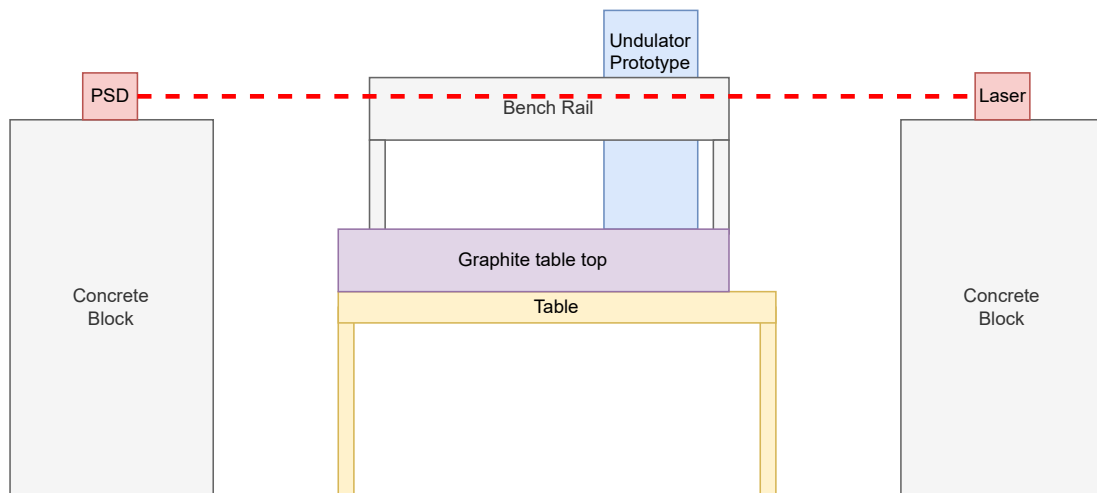


Figure 5.3: Illustration of the Test Setup

It is imperative that the different components of the measurement setup are aligned to the best scenario possible to minimise errors in the probe position due to parallelism errors or misalignment. The alignment procedure is as follows:

- i. The concrete block that has the lasers and PSDs assemblies are roughly aligned within an acceptable error margin.
- ii. The lasers and PSDs positions can be adjusted horizontally and vertically via 2 motorised stages. The motors are used to properly align the laser beams and PSDs positions via the motorised stages through a PLC program on the main Beckhoff PLC.
- iii. The table with the undulator and the measurement bench is then installed in the path of the laser such that the laser beams pass through the pinholes on the Hall probe holder. This is done by manually moving the holder using the Hall probe positioning system, the position of the incident light on the PSD from the laser passing through the pinholes is then considered as the reference point of the Hall probe positioning system control loop.
- iv. Parallelism between the laser beams and the bench setup is then optimised manually through a trial and error procedure to an acceptable level which concludes the alignment procedure.

Any further alignment errors in the test setup due to imperfections in the test setup such that in the table surface or the linear rails are to be compensated via the Hall probe positioning system while the bench travels along the test undulator during

measurement. The alignment procedure is carried out prior to any tests to ensure optimal performance of the bench.

5.2 Test Plan

Several tests were performed to characterise the prototype undulator and benchmark the μ MMB performance, the quality of the magnetic measurements is compared to the performances of the previously implemented system and the Teslameter as a stand-alone instrument. The tests performed are illustrated in the test matrix in Figure 5.4

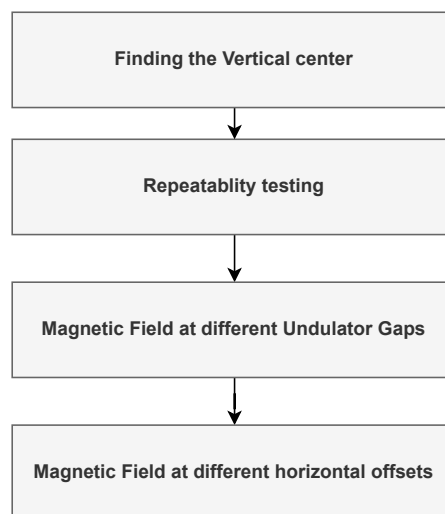


Figure 5.4: Serial Test Matrix to Evaluate the Bench's Performance and Characterise the Prototype Undulator

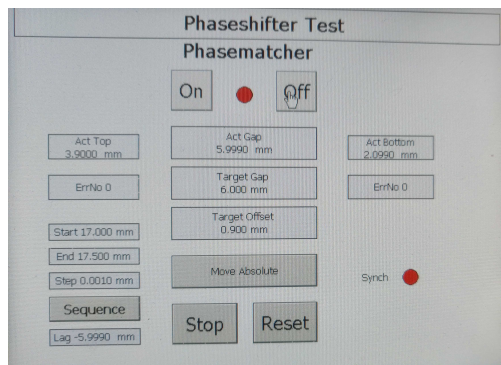
The prototype undulator is a planar undulator which means that there are 2 magnet arrays where one is installed at the top part of the frame and the other in the opposite bottom part of the frame. Each array consists of 10 magnets magnetised in a way to create a planar sinusoidal magnetic field at the centre of the device.

The magnet arrays are installed to the top part of the frame via custom designed bracket that binds the magnets together and is fitted into slots located at the top and bottom parts of the frame. Each of the magnet arrays can be displaced vertically to create a variable gap device. This is done by a stepper motor system that can be controlled via a GUI implemented on a touch screen Human Machine Interface (HMI) device.

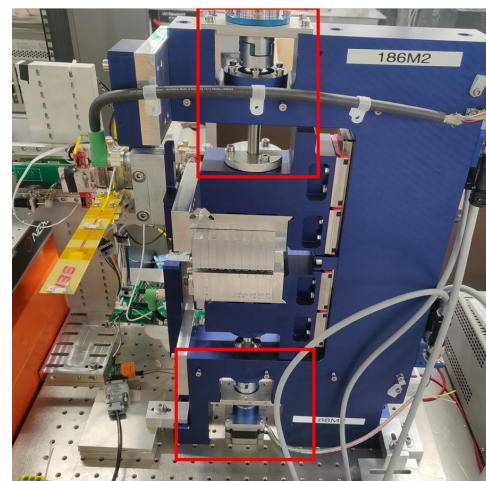
The stepper motor stage for each array allows the user to vary the gap to perform relevant testing, and can introduce an offset to both arrays to keep the gap constant

while varying the position of the undulator with respect to the Hall probe sensor. This feature is particularly important to be able to perform magnetic measurements at the vertical centre of the device since in this test setup, the position of the Hall probe sensor, and by extension the Hall probe holder, is dictated by the initial alignment procedure of the laser beams and the PSDs.

In other words, when the laser and the PSD positions are fixed, the SAFALI base Hall probe positioning system adjusts the Hall probe holder position to be in line with of the laser beam and in order to perform measurements at different vertical positions, the undulator arrays must be translated up or down accordingly by the same displacement. The described HMI and the motorised variable gap system is highlighted in red in Figure 5.5a and 5.5b respectively.



(a) The Human Machine Interface Used to Change Gap & Vertical Offset



(b) Stepper Motors (highlighted in red) for Variable Gap Operation & Positional Offset

Figure 5.5: The Variable Gap U-Frame (blue frame) & and the Accompanied HMI

To vary the gap of the prototype undulator from the HMI, the value *Target Gap* can be set to the desired gap followed by a touch input to *Move Absolute* button on the HMI to execute the command.

Moreover, to translate the magnets arrays vertically while keeping the gap constant, the value *Target Offset* is varied accordingly followed by a touch input to *Move Absolute* button similar to the gap change procedure to execute the offset. The offset is then applied differentially to the upper and lower stepper motors to achieve that offset whilst maintaining a constant gap, which effectively translates the undulator up and down as required.

5.2.1 Finding the Vertical Centre

In a previous chapter, it was mentioned that the vertical magnetic field (or y-field) in an undulator is extremely sensitive to the slightest changes in the vertical position

of the sensing element, specifically to this case, the y-field is extremely sensitive to the position of the Hall probe sensor during measurement. Typically, magnetic measurements where the position of the Hall probe is within few μm from the true vertical centre of the undulator is accurate and deemed acceptable.

Hence, most measurement systems utilise components with manufacturing precision and low tolerances, and Hall probe positioning systems similar to this bench's SAFALI based system.

The vertical magnetic field (y-field) on the other hand is not affected by small position errors in the horizontal sensing element. Hence, it is a standard practice to estimate the horizontal centre of the undulator using less accurate means such as finding the horizontal centre using gauge blocks or a Vernier Calliper. A Vernier Calliper was used in this case to find the horizontal centre of the undulator under test.

There are several ways to find the true vertical centre of an undulator, a practical approach was used in this measurement campaign. The relationship between the Root-Mean-Square (RMS) y-field and the vertical position of the Hall probe sensor is quadratic, which translates to a parabolic curve on an RMS y-field vs gap graph. Therefore, several magnetic measurements were performed at different offsets to construct the parabolic curve.

At each vertical offset, 3 measurements were performed and the peaks, or the amplitude of the sinusoidal magnetic field, were extracted from the y-field profile and are averaged to a single value to result in a single field value from each measurement file. The average value from each of the 3 measurements performed are then averaged and the RMS value is calculated which is then plotted against the corresponding relative offset at which the measurements was performed.

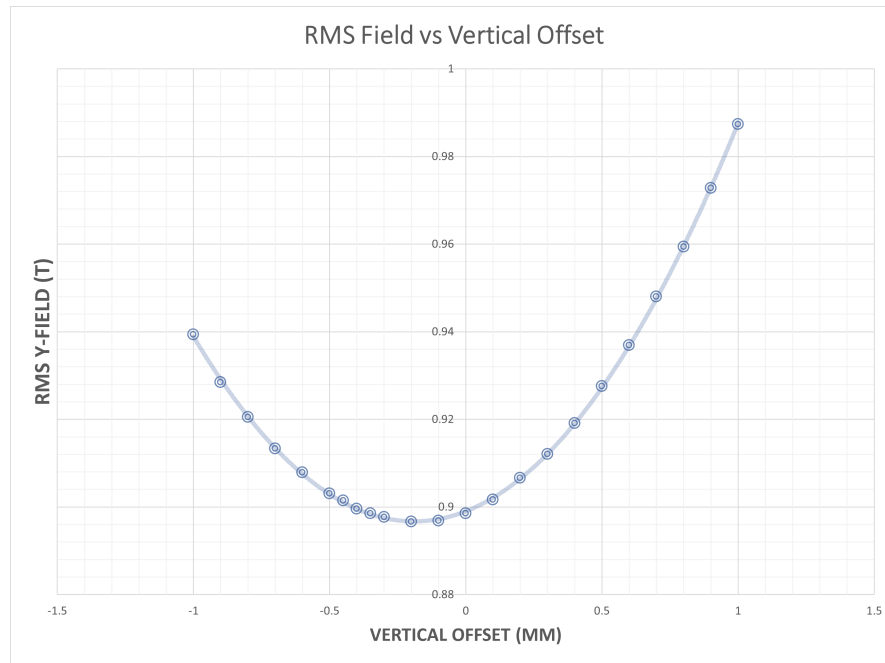


Figure 5.6: RMS Vertical Magnetic Field vs Relative Offset

The constructed parabolic curve is illustrated in Figure 5.6. The equation of the parabolic curve was estimated using a 2^{nd} order polynomial fit. The extracted equation is given by Equation 5.1.

$$y = 0.0642x^2 + 0.0243x + 0.899 \quad (5.1)$$

$$\frac{dy}{dx} = 0.1284x + 0.0243$$

$$0 = 0.1284x + 0.0243$$

$$\therefore x = -0.189 \quad \text{when} \quad \frac{dy}{dx} = 0 \quad (5.2)$$

Where y is the RMS field value the x is the vertical offset of the magnets in mm. The minimum of Equation 5.1 indicates the vertical centre of the undulator. The minimum is obtained by differentiating Equation 5.1 and finding the offset value where the rate of change is 0. The minimum RMS field occurs when the vertical offset on the undulator is -0.189mm .

The vertical alignment is complete given that other components of the measurement setup are kept at the same constant position and magnetic measurements can be performed.

5.2.2 Repeatability Testing

The magnetic data acquisition is performed by the 3-axes Teslameter, hence, the absolute limit to the errors of any measurement is dictated by that acquisition instrument. In this section, the performance of the bench is benchmarked to quantify the magnitude of errors introduced by the bench components such as the Hall probe positioning system. The performance of the current bench is compared to the previously implemented bench and to the Teslameter as a stand-alone instrument. To obtain comparable results, the same procedure for repeatability analysis used during the development of the Teslameter were performed. The Hall probe was attached to the bench via small hex screws to the new Hall probe holder piece, the bench is then instructed to perform 110 consecutive measurements at a constant velocity of 10mm/s and an acquisition frequency of 1KHz on the Teslameter. The first 10 measurements are not included in the repeatability analysis to allow for the Teslameter, the Hall probe, and the rest of the bench's electronics to reach a steady state temperature and to reduce the effects on the magnetic measurements due to temperature drifts. The specified period to reach the temperature stability of the Teslameter is 15 minutes which corresponded to 10 measurement sweeps of 1 minute and 30 seconds each.

The errors introduced by the bench in an ideal scenario should be negligible, however, the Hall probe positioning system introduces errors due to the variations in the probe location with respect to the vertical centre of the undulator being tested.

A typical magnetic measurement is as shown in Figure 5.7 that illustrates the three field components plotted against the physical position obtained from the Heidenhain encoder.

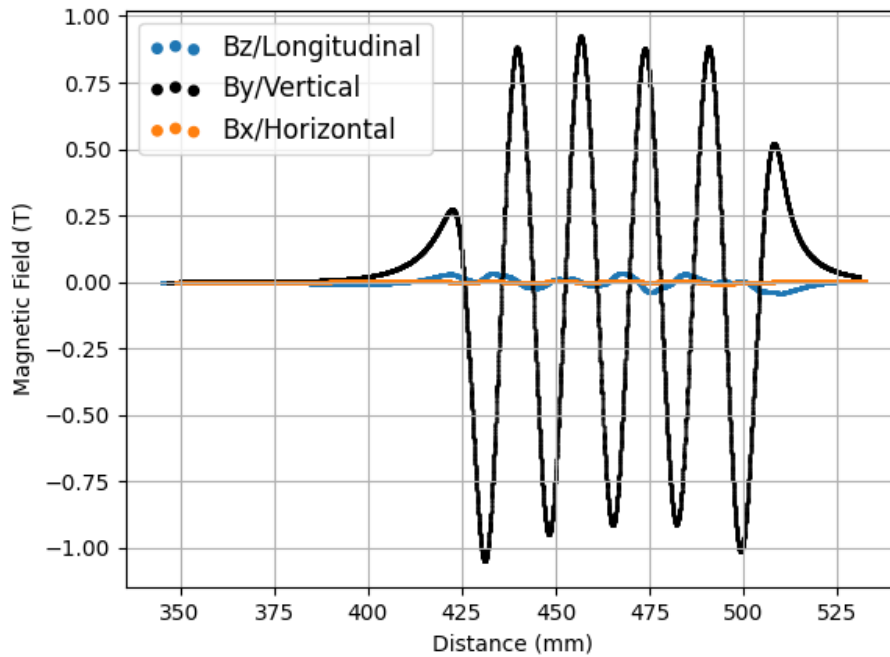


Figure 5.7: Typical Magnetic Measurement Performed at a gap of 6mm and a Velocity of 10mm/s

The last magnetic measurement of the included set, or the 110-th measurement, is used as the reference measurement at which the other measurements are compared to at each physical position along the device. However, each magnetic measurement performed is not at predefined physical locations along the device which results in magnetic data points at different physical locations and different measurements cannot be compared directly to the reference measurement to quantify the errors. This was resolved by interpolating all magnetic points to the positions of the reference measurement to obtain a set of magnetic measurement at mutual discrete positions. The magnetic measurement values were interpolated linearly as results obtained from higher order interpolations were comparable. A visual illustration of the interpolation process is shown in Figure 5.8.

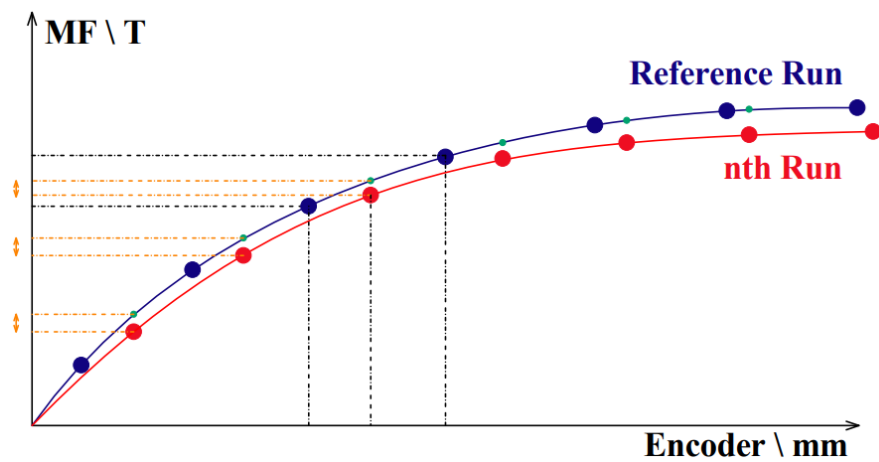


Figure 5.8: An Illustration of the Linear Interpolation on a Reference Magnetic Measurement [5]

The errors are then calculated as percentage errors of each measurement in comparison to the reference measurement over the peak magnetic field value of the reference measurement. The errors obtained from the 100 measurements are illustrated in Figure 5.9 and the maximum, mean and standard deviation are plotted at each position as shown in Figure 5.10 to further clarify the worst-case percentage errors at each position.

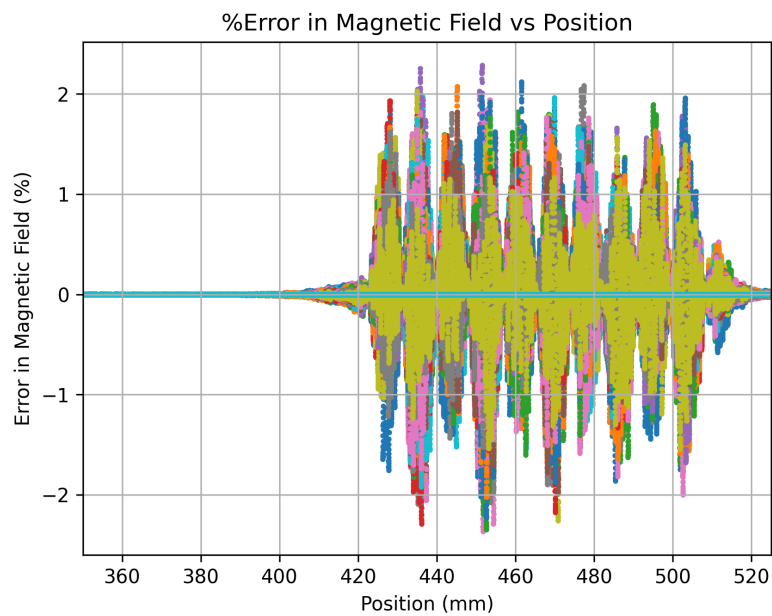


Figure 5.9: The Superimposed Percentage Errors from the 100 Magnetic Measurements at each Position

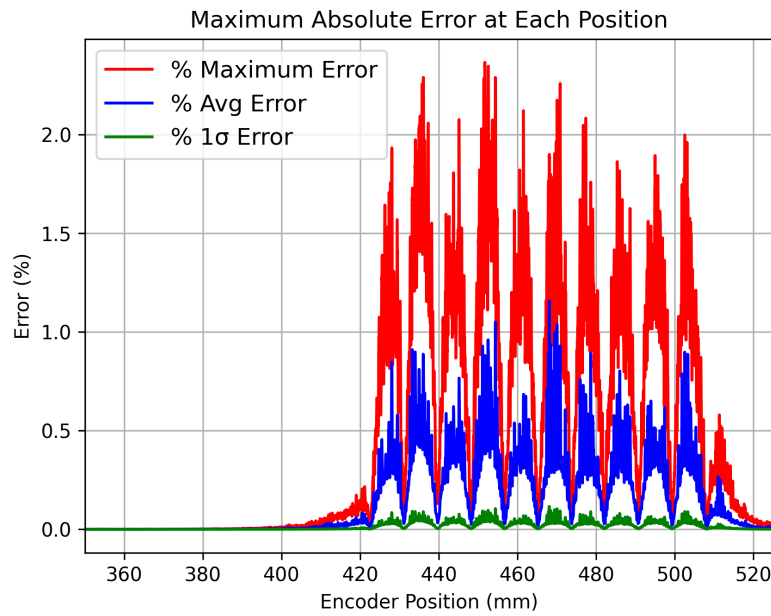


Figure 5.10: The Maximum, Mean, and Standard Deviation of the 100 Magnetic Measurements at each Position

The percentage errors obtained with the current bench was compared to the previously implemented version of the bench in addition to the Teslameter instrument as a stand-alone component. The comparison is summarised in Table 5.1. The maximum error across all positions obtained from the current version of the bench repeatability analysis is 2.278% while the maximum standard deviation is 0.113%. It is expected for the current bench setup to introduce errors to the magnetic data acquisition system (Teslameter), however, the maximum error value is considerably higher than that recorded during the test phase of the previously implemented version of the bench. To understand the sources of the higher error levels, further investigations were performed.

	Current Bench	Previous Bench	3-axes Teslameter
Max Absolute Error	2.278%	0.37%	0.28%
Max Std. Deviation	0.113%	0.09%	0.06%

Table 5.1: Performance Comparison Between Current Bench, Previously Implemented Bench, and the Teslameter as a Stand-alone Instrument

5.2.2.1 Sources of Error Investigation

As mentioned in Chapter 3 in Section 3.4.4.2, the x-axis degree of correction in the Hall probe positioning system was omitted from the control loop due to the excessive vibrations introduced by the mechanics of the stage which negatively affected the vertical position of the probe during measurement.

During every measurement of the total 100 measurements, the position of the Hall probe holder from the position feedback loop is logged and a text file is saved to the Raspberry Pi for post-test analysis. During the 100 measurements, the position of the probe in the x and y are plotted as shown in Figure 5.11. The probe position in the y -axis is actively corrected and the position of the Hall probe holder was maintained within $\pm 11\mu\text{m}$.

On average, the Hall probe remained within $\pm 7\mu\text{m}$ of the vertical centre of the undulator, and the higher value of $\pm 11\mu\text{m}$ occurred only twice across all the 100 measurements, hence, it can be safely assumed that the Hall probe position was maintained within $\pm 7\mu\text{m}$. This result is not conclusive, and the source of the error could not be identified using the Hall probe position data.



Figure 5.11: The Errors of the Hall Probe Position During the 100 Magnetic Measurements at each Position

It is inherent to the system that the probe is attached from its base to the mechanical stage while the sensor is several centimetres away from the fixation point. This causes the Hall probe sensor to react aggressively to any small vibrations that might occur at the fixation point due to the leverage effect of the assembly. Therefore, the effect of small vibrations at the base of the Hall probe at the holder was investigated.

To highlight the source of the amplified vibrations in the Hall probe holder, the 2 different sources of vibrations, which are the linear motor and the probe positioning system correction stages, were isolated and few measurements were performed. Once the measurements were obtained, analysis in the frequency domain was done to further

understand the vibration effect using the Fast Fourier Transform (FFT) algorithm [52].

With the 2 vibration sources mentioned, the following conditions for each measurements were performed to highlight the vibration source affecting the accuracy of the magnetic measurement.

Condition 1: The linear motor is disabled, and no power is supplied to the three phases of the motor. Also, the probe positioning system feedback loop is not activated i.e. no active corrections to the position of the probe holder are performed.

Condition 2: The linear motor is still disabled with no power to the phases, and the correction loop of the Hall probe positioning system is active. This was performed to obtain the noise level introduced by the positioning system, mainly from the laser and PSD setup since the linear motor is disabled and no linear movement is performed.

Condition 3: The linear motor is powered and actively maintains a velocity of 0mm/s and the correction loop of the Hall probe is not active. The result from this test gives an indication of the noise levels introduced by the linear motor assembly.

Condition 4: Both the linear motor and the probe position correction loop are powered and enabled i.e. the liner motor is powered and actively maintains 0mm/s velocity, and the position of the Hall probe holder is being actively corrected.

To further clarify the test conditions, the measurements performed as explained in the four different conditions were stationary magnetic measurement with identical period of measurement to ensure similar magnetic data points were gathered at each measurement condition such that the FFT analysis is comparable in terms of frequency spectrum density. The FFT analysis from the different test conditions are illustrated in Figure 5.12, a typical measurement data was included in the analysis for comparison.

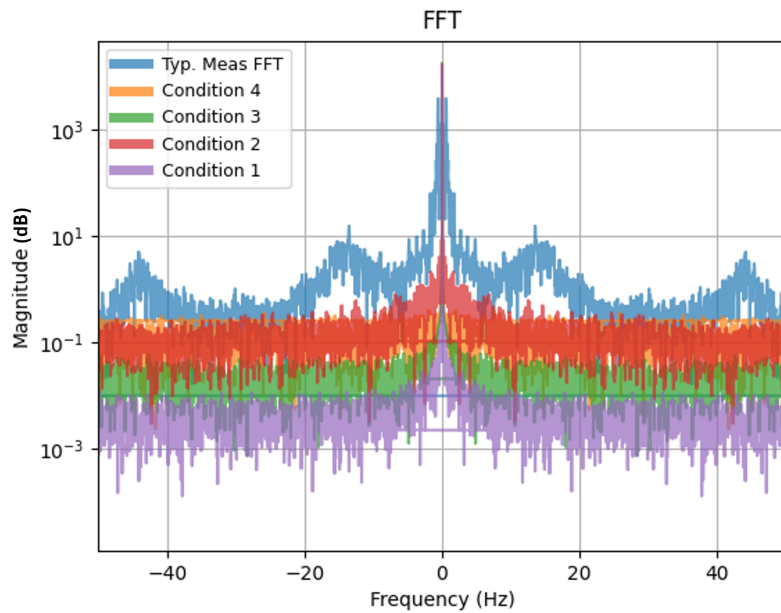


Figure 5.12: The FFT Analysis for the Four Test Conditions Including FFT From a Typical Magnetic Measurement

From the FFT plotted in Figure 5.12, it can be seen that the noise floor gradually increases when the linear motor and the probe stabilisation are enabled i.e. the linear motor is powered and the motion controller is actively maintaining a velocity of 0mm/s, and the probe stabilisation is enabled and actively correcting the position of the Hall probe holder.

Comparing the four different test conditions to a typical FFT obtained from a typical measurement where the probe positioning correction loop is enabled and the linear motor is traversing the bench along the undulator, frequency components other than that of the undulator magnetic field are present at approximately 13.5Hz and 44.1Hz. With reference to Section 3.4.1, the velocity of the linear motor was tuned to be within approximately ± 2 mm/s of the set reference. The accuracy in this case is limited by the performance of the motion controller among other sources of errors discussed in Chapter 3.

Furthermore, and with reference to results presented in Section 3.4.4.2, the new mechanical stage for the Hall probe positioning system provides a rigid mechanical support for the Hall probe holder. However, this introduced a new problem where any slight corrections in the horizontal axis led to excessive oscillations at the tip of the in the vertical direction. The excessive vibrations is partially due to the mechanical design of the probe holder stage where the linear bearings used to allow for horizontal movement, are used as both guiding dowels and linear bearings.

In addition, the type of bearings used is not tight fitted into the slot on the new probe holder which allows for the small vibrations from the movement of the linear motor

to be transferred from the base of the bench to the probe holder, and consequently to the Hall probe sensor itself. This is also amplified by the lever effect of fixing the Hall probe from one end while the other end is suspended in air with no mechanical support. Due to time limitations and availability issues due to long lead times from manufacturers, designing and manufacturing a new probe holder with improved stability was not possible, instead the older linear bearings were used with the new stage as an alternative solution.

Figure 5.13 highlights the slots on the new probe holder stage where the linear bearings are interfaced to the holder.

From the above, it can be deduced that the mechanical fit of the new probe holder stage, along with the inherent vibrations of the linear motor are the source of the noise peaks shown in Figure 5.12. This consequently degrades the repeatability of the bench when compared to the previous version of the test setup. Although it is concluded that the source of the vibrations is the movement of the linear motor, it is not an indication that the linear motor is not suitable for the application, but it is a mechanical design issue that needs reconsideration in future versions of the bench.

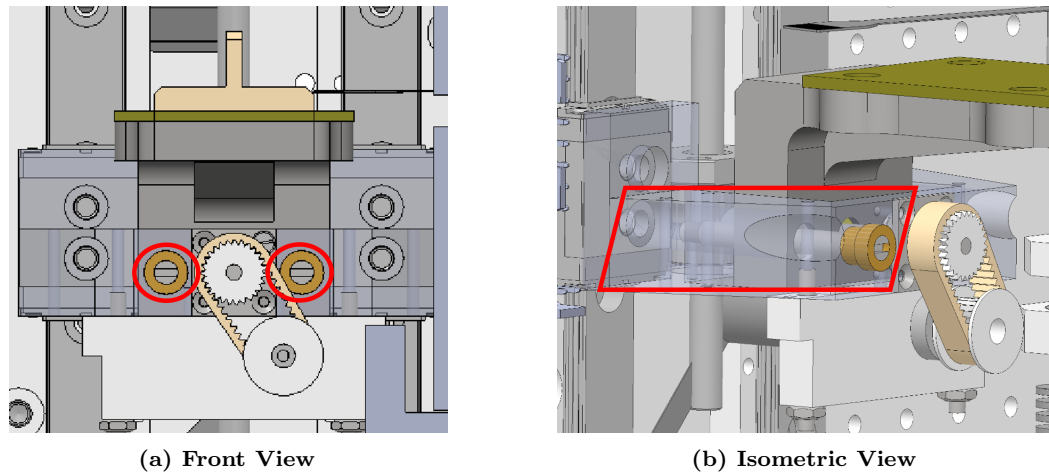


Figure 5.13: The New Probe Holder Stage - Linear Bearings Slot Highlighted in Red

5.2.3 Magnetic Measurement at Different Gaps

The main parameter of an undulator is the K-Value which is also referred to as the undulator strength. The K-Value dictates the wavelength of the photons emitted by the electron beam due to magnetic field profile of the insertion device. Equation 5.3 defines the relationship between the wavelength of the generated light and the parameter K where λ is the wavelength of the generated light, λ_u is the undulator period length and γ is the relativistic Lorentz factor. All parameters in the equation apart from K are not controllable, therefore, the ability to tune the generated photons

is possible by varying the strength of the undulator (K).

$$\lambda = \frac{\lambda_u}{2\gamma^2} \left(1 + \frac{K^2}{2}\right) \quad (5.3)$$

$$K = \frac{e}{2\pi m_e c} \lambda_u B_0 \quad (5.4)$$

The parameter K is defined by Equation 5.4. Apart from B_0 , all other parameters are constants either by the physical design of the undulator, or by their physical definition. Hence, to change the parameter K, the strength of the magnetic field B_0 must be varied accordingly. The strength of the magnetic field can be mainly by using stronger magnets or by operating at very small gaps (few mm range) and in a variable gap undulator, such as the one under test, the gap is changed accordingly to obtain the desired K value.

During the optimisation procedure of a variable gap undulator, the value of the parameter K is characterised over the range of operational gaps to obtain a lookup table of gap values that corresponds to the desired undulator strength K. In this section, multiple measurements were performed to obtain all possible K values that can be realised over the range of the operational gaps. The procedure of the magnetic measurement is identical to the one explained in Section 5.2.2, the operational gap was changed using the Graphical User Interface illustrated previously in Figure 5.5.

The operational gap range is between 4.5mm and 9.5mm, three magnetic measurements were performed at 11 different gaps in incremental steps of 0.5mm. From each of the 3 measurements, the vertical magnetic field values were extracted to be averaged to obtain a single average peak value at each gap. The K is then calculated with the averaged magnetic field value according to Equation 5.4. Figure 5.14 shows a plot of the gap in mm vs the K value across the operational gap range of the prototype undulator.

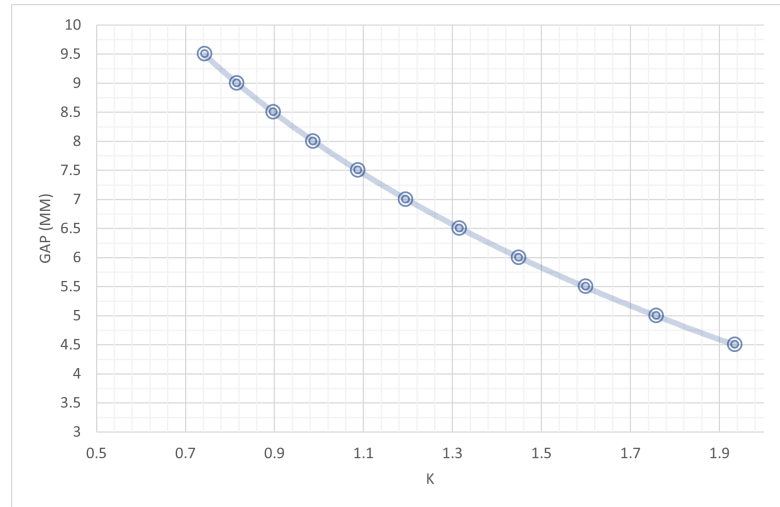


Figure 5.14: Measurements Results of the Gap vs K correlation for 11 Different Gaps

With the obtained relationship between gap and K, a user can select the desired k value by operating the undulator in the corresponding gap value.

5.2.4 Magnetic Field at Different Horizontal Offsets

In an undulator, the attraction forces between the magnet arrays leads to bulky frame design and powerful locomotion systems to be implemented to support the mechanical stresses and tunable devices. The attraction force also contributes to deformation in the supporting structure of the undulator which translates to inhomogeneity in the magnetic field map and extra complexity in the optimisation process. The prototype undulator under test is equipped with repelling permanent magnets adjacent to the main magnets which compensate the attraction forces between the magnets arrays and reduce the mechanical load and deformation in the supporting structure.

Although the benefits are apparent from such approach, it is essential to study the effect of the force compensation magnets on the magnets that define the magnetic field profile of the device. Therefore, in this section, several magnetic measurement were done to study and quantify the effect of the side magnets on the main undulator field.

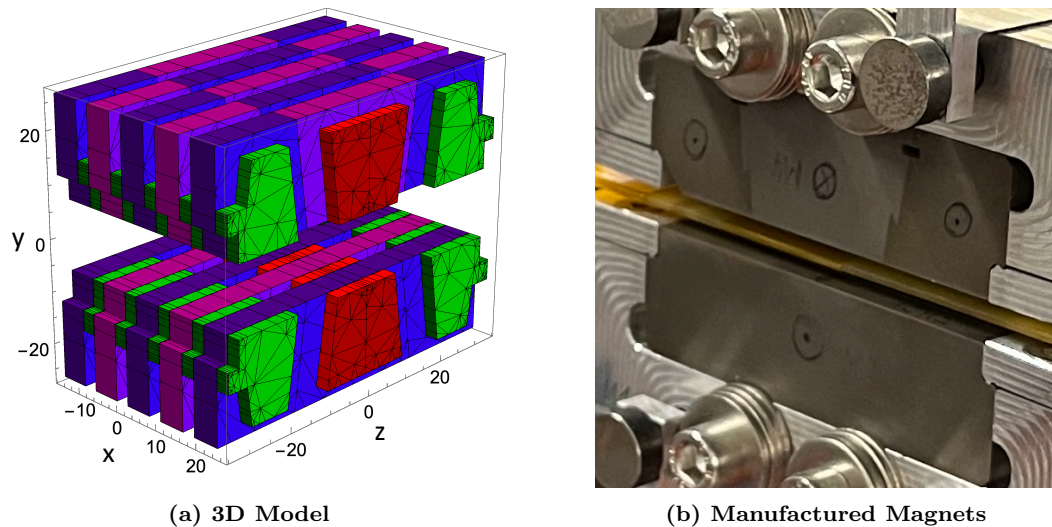


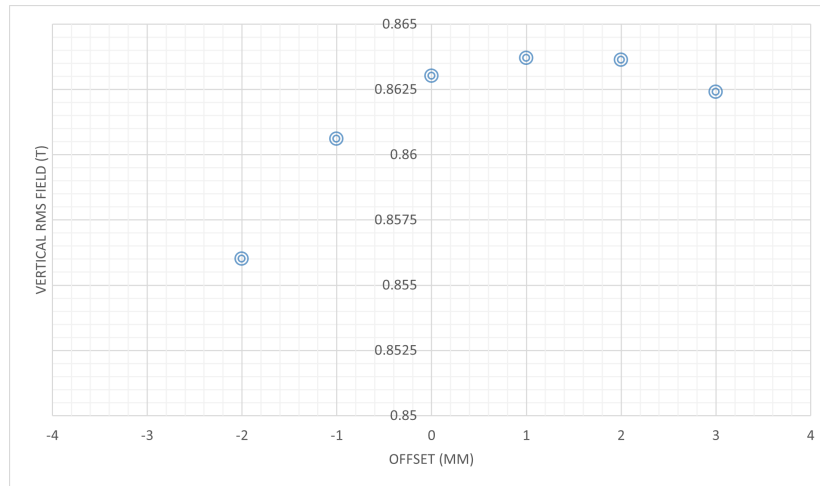
Figure 5.15: Model and Manufactured Magnets for the Force Compensated Prototype Undulator
 (The radia model differs from the manufactured magnets - due to time constraints from the manufacturing process)

Figure 5.15 shows the modelled and the manufactured force compensated magnets that were used to assemble the magnets array of the prototype undulator. The permanent magnets are in blue and purple to distinguish the two different magnetisation directions while the iron poles are in red and green to distinguish between the ones which enhance the undulator field and the ones which compensate the forces respectively.

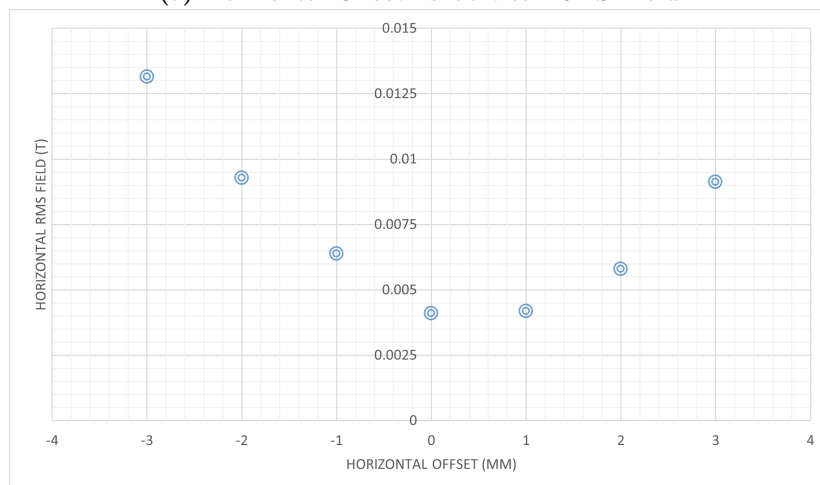
To study the effect of the side magnets, several magnetic measurements were performed at different horizontal offset i.e. away from the horizontal centre of the device to analyse the effect of the force compensation magnets on the magnetic field profile of the undulator. The blue frame shown in Figure 5.2 was shimmed from a pre-installed hard-stop aluminium block at the horizontal centre at the beginning of the measurement campaign described in this chapter. To perform the horizontal offsets, precision ceramic gauge blocks were used to alter the position of the frame by $\pm 3\text{mm}$ in steps of 1mm, which is more than sufficient region as the electron beam from a light source deflects horizontally within tens of μm . Three magnetic measurements were performed at each offset position and the RMS field values for the vertical and horizontal fields are then calculated in a similar way to the vertical alignment procedure explained earlier in this chapter. Figures 5.16a and 5.16b illustrate the relationship between the RMS field value and the horizontal offset for the vertical and horizontal fields respectively.

The change in the RMS magnetic field is minimal where the maximum difference in the horizontal and vertical fields is 9.04mT and 17.58mT respectively. Due to the slightly poor accuracy results highlighted when performing the repeatability analysis, the larger change in the RMS field value of the vertical field can be partially

contributed to random errors from the measurement bench. Hence, it can be said that the side magnets do not significantly affect the main undulator field within the horizontal range of $\pm 3\text{mm}$.



(a) Horizontal Offset vs Vertical RMS Field



(b) Horizontal Offset vs Horizontal RMS Field

Figure 5.16: The Effect of the Force Compensation Magnets on the Main Field of the Undulator

5.3 Chapter Summary

The testing setup of the new prototype undulator using the implemented μMMB was presented in this chapter along the challenges faced when assembling a stable testing environment. The process of setting the measurement setup and aligning the probe positioning system components was described as per the usual practices in a similar measurement campaign.

Unforeseen issues were faced due to the inherent mechanical properties of the measurement bench which caused errors in the magnetic measurements data which required further analysis to highlight the errors source.

The main characteristics of the prototype undulator were presented and the effect of the force compensation magnets on the field enhancing main magnets was investigated. Minimum interference on the main magnets due to the side magnets was noted which validates this design concept and adds more confidence to implement it in the upcoming SLS2.0 upgrade.

The new magnetic design with the force compensation looked promising and could reduce the overall size and cost of the new generation of undulators. This reduces the need for a heavy and bulky mechanical structure to support the weight and the attraction forces between the magnetic arrays of the undulator.

Chapter 6

Discussions & Conclusion

6.1 Summary of the Dissertation

During the period of this project, the previous prototype of the μ MMB was studied to highlight a path of improvements that would elevate the performance of the electronic systems in order to achieve a more reliable measurement system. The improved system can be easily utilised to perform measurement campaigns on various insertion devices while they are physically installed and deployed inside the tunnel or storage ring in light sources, such as SwissFEL and SLS.

In this chapter, several parts of the measurement system are critically analysed to highlight the main weaknesses of the system and to suggest future improvements to further enhance the measurement system accuracy, precision and overall functionality.

6.2 Summary of the Research Goals and Results Achieved

The initial goal to improve the implementation of the measurement system was performed and the integration of all components of the system, including the 3-axes Teslameter on a single PCB was achieved. To satisfy the physical space limitation for the system to fit inside a narrow vacuum chamber, improvements were made in the hardware used to perform critical tasks in the system such as the migration to compact and surface mount components packages for the CAN controller and transceiver and the ZigBee module respectively.

Also, the power delivery to the different electronics components was revised where dedicated DC-to-DC regulators to remove the dependence on an external power supply to supply the different voltage levels required by the bench. The input power to the bench is supplied from a single generic PLC power supply and the voltage levels to operate the bench are then produced on-board. 12V regulators were used to power the motion controllers for all 9 motors, 5V converters were used to power

the control and communication electronics, and $\pm 6V$ to power the 3-axes Teslameter instrument.

The electrical system was segregated over 2 custom PCBs where one houses all control and different communication electronics including the Raspberry Pi and interfaces to the other PCB which acts as the base plate that carries the rest of the electronic components along the linear motor rails smoothly including the Teslameter. The base plate PCB has sockets for the motion controllers that can be swapped and serviced with minimal effort and contains a stand-alone battery charging circuitry for an option to power the system from a Li-Po battery and eliminate any external wires from a power supply.

The developed system was then tested for benchmarking the performance when compared to the previous prototype of the bench and Teslameter as a stand-alone instrument. The measurement campaign performed showed that the new implemented bench lacked in performance when compared to the other two systems and further analysis was performed to investigate the source of the issue.

The investigation showed that the new mechanical stage was not effective in improving the stability of the Hall probe positioning system where it introduced new issues which are discussed later in this chapter.

The μ MMB was then utilised as the main measurement system to characterise, for the first time at PSI, a new prototype undulator that incorporates force compensation magnets adjacent to the field enhancing magnets. The magnetic characterisation and results obtained from the measurement campaign on the prototype undulator leads to more confidence in the magnetic design with force compensation by investigating the main characteristics of the device and quantifying the effect of the force compensation magnets on the magnetic field from the field enhancing magnets.

6.3 Limitations of the μ MMB

Several aspects of the developed system impacted the accuracy and precision of the magnetic measurements obtained. In this section, the drawbacks faced during the measurements which were mainly due to the mechanics of the bench are discussed.

6.3.1 Mechanical Bench

It was previously mentioned during the development of the prototype of the bench [4] that the mechanical support for the Hall probe holder which is a part of the Hall

probe positioning system lacks the mechanical integrity to support the weight of the holder. This led to roll angle and horizontal axis correction stages in the positioning system to be omitted from the tested prototype by hard fixing the holder directly to the vertical correction stage only. This allowed the initial benchmarking process to be performed to quantify the performance of the bench and as a proof-of-concept of a low-profile SAFALI based measurement bench.

To address this problem, a new stage for the Hall probe holder was manufactured with wider support for the probe holder, however, the ability to correct the roll angle was not implemented. The holder is firmly fixed to the new stage via 4 hex bolts and corrections in both the horizontal and vertical axes were possible. However, the horizontal stage was introducing too many vibrations in the vertical axis as illustrated in Chapter 3 and therefore, the active correction of the Hall probe position was applied only in the vertical axis given that the vertical position of the Hall probe is more sensitive to changes in the main magnetic field of the undulator.

Furthermore, during the benchmarking of the μ MMB, the magnitude of the absolute error in the repeatability testing was found to be higher when compared to the same errors obtained from the previous version of the bench and the Teslameter as shown in Chapter 5. An investigation was carried out and the source of the errors was due to the loose fit of the linear bearings of the horizontal correction stage which transferred the inherent vibrations from the linear motor to the Hall probe holder. The vibrations are amplified further at the tip of the probe holder from the lever effect.

The second system in the bench is the magnetic pole adjustment system which was described in Chapter 3. No official testing was performed to this system due to the lack of an insertion device that incorporates height adjustable magnets. Nevertheless, certain aspects of the system can be assessed predicatively from experience gained from other parts of mechanical bench without the need to perform certain tests due to similarities in the mechanical design.

The magnetic pole adjustment system consists of 2 motorised screwdrivers, one for each of the opposite magnet arrays such that simultaneous adjustments can be performed to both arrays. Each screwdriver is composed of 2 stages, one stage engages/disengages the screwdriver's head such that it is inserted properly in the hex screw and the other one rotates the hex screwdriver head to adjust the angular position of the hex screw and consequently adjust the height of the pole.

The mechanics of the screwdriver engage/disengage stage is identical to that of the roll angle adjustment stage in the Hall probe positioning system which was deemed

mechanically weak during the development of the first prototype of the bench. To slot the hex head of the screwdriver into the hex screwdriver groove, several engage attempts might be necessary at the exact position of the groove since the orientation of the hex screw is unknown to the system. This results in multiple engage attempts to press the hex head on the side of the screw and knowing the mechanical strength of the stage, would probably cause slippage in the connection between rotary motor and the mechanical stage which would indicate a false engagement event which is not ideal for the application.

From the above-mentioned points, it is advised that the mechanical design for the Hall probe positioning system is revisited and improved according to address the issues raised in this dissertation.

6.3.2 Electronics System

Although the electronics system performance was sufficient for the task, several improvements can be performed to further enhance the overall measurement system. For example, the main controller used for the bench is the Raspberry Pi Zero W which is powered by the BCM2835 System on Chip (SoC) [30]. The SoC is a single core ARM processor running on a 700MHz clock signal which is faster than most microcontrollers and provides more open-source support with the ability to low-level access to several essential peripherals such as SPI and UART.

Given the compatibility of the peripherals of the different Raspberry Pi computers, the option to operate the bench with a Raspberry Pi with a more powerful processor is viable and could result in better performance without major changes to the electronic systems. However, space constraints still apply, hence, an upgrade can utilise the *Raspberry Pi Zero W 2* [53] or a *Raspberry Pi Compute module 4 (CM4)* [54] which are a faster version of the Pi Zero W and a compact version of the full-size Raspberry Pi 4 respectively. The CM4 would require a redesign of the control PCB to have a dedicated socket for the different footprint of the CM4 while the upgrade to the Pi Zero W 2 is effortless as it is built on the same physical footprint of the currently utilised Pi Zero W.

The Raspberry Pi Zero W 2 was considered to be the main controller in the bench, however, due to the global shortage of electronic components and specifically the high demand on the Raspberry Pi boards, the previous Pi Zero W was used to avoid delays.

6.4 Future Improvements

The implemented μ MMB is a result of a set of mainly “pre-chosen” system components during the previous development period. This included the Faulhaber motors and motion controllers. Therefore, no major changes in the essential components was made as the core system components were established during the previous prototype implementation period to sufficiently fulfil the required performance criteria. On the other hand, the mechanical system requires further improvements to be considered as future upgrades as mentioned in this section. Focusing mainly on the mechanical system, the following can be improved to bring more functionality to the bench.

Hall probe positioning system: It was highlighted in Chapter 5 that the reproducibility of the Teslameter was heavily impacted by the vibrations transferred from the linear motor to the Hall probe sensor. Therefore, the positioning system must be redesigned to reincorporate the roll angle correction degree, improve the stability of the horizontal stage, and minimise the effect of the aforementioned vibrations.

Magnetic pole adjustment system: Although this system was not properly tested since no suitable apparatus was available during the testing phase, a foreseen issue in the system must be rectified. This was previously faced in the original probe holder stage where the Hall probe is attached to the small roll angle stage with little surface area and the mechanics of the stage were not rigid enough to support the weight of the sensor. The motorised screwdrivers are equipped with identical mechanical stages that engage/disengage the hex head to interface with the hex screws for pole height adjustment, the mechanics were prone to slippage and overall mechanical weakness and hence, an alternative mechanical stage must be considered.

Addition of homing sensors to all motors: One of the software improvements implemented in this research was the soft homing procedure that is performed at the start of the Python script of the bench. All rotary motors are equipped with single turn rotary absolute encoders that indicate the current position of the shaft of the motor uniquely within a single shaft turn, further rotary movement is compensated for in the motion controllers to keep track of multi turn movement required. The homing sequence assumes that the motion stages start from the lowest position possible, and that position is defined as the virtual homing point and the absolute position of the stage is calculated by the motion controller accordingly. To avoid the uncertainty from a rough homing procedure, small homing sensors can be included in a future revision of the bench such that homing can be done accurately to a physical reference point even when

the power is turned off from the source and the motion controller loses its current position. This improvement is not applicable to the linear motor as it is equipped with the Heidenhain linear absolute encoder.

Linear motor upgrade: The linear motor used was chosen mainly due to its low profile when compared to other offers in the industry. Although the motor package is compact, low-profile and is provide great performance, the lack of internal Hall effect feedback to the motor phases can be considered as a drawback. Hence, it is recommended to redesign the base plate of the bench such that it can incorporate a slightly taller linear motor with integrated Hall effect feedback sensors. This can be done by reducing the material thickness of the linear motor groove underneath the base plate to maintain the same clearance available for Hall probe positioning and the magnetic pole adjustment systems and provide more space for a taller linear motor that are also supplied from the same manufacturer and utilise the same operational concepts and structure.

Motion controllers upgrade: It was planned to use the new motion controller MC3001 from Faulhaber to drive the motors of the bench. Due to the long lead time on delivery caused by a global electronic components shortage, the older MCBL3002 and MCLM3002 were used. The main advantage of upgrading to the MC3001 in the future is the smaller physical footprint to reduce the length of the base plate PCB for a more compact implementation. This improvement is not essential as no performance benefit will be gained apart from longevity of technical support and availability from Faulhaber.



(a) Raspberry Pi Zero 2 W [53]



(b) Raspberry Pi-Compute Module 4 [54]

Figure 6.1: Main Controller Future Upgrade Suggestions for the μ MMB

Main controller upgrade: A simple plug and play upgrade to the main controller of the bench is to upgrade to a *Raspberry Pi Zero 2 W* as it is pin to pin compatible with the currently used *Raspberry Pi Zero W* but with faster SoC

and higher clock speeds.

Moreover, another upgrade is possible by using a *Raspberry Pi Compute Module 4 (CM4)* which performs identical to a full-size Raspberry Pi 4 with smaller footprint. However, an upgrade to the CM4 would require the control PCB to be redesigned to interface properly with the CM4 smaller General Purpose Input Output (GPIO) connector.

As of the start of this research, both options were released to the market however, it was very difficult to obtain one as the demand on Raspberry Pis was enormous due to the global shortage of electronic components. Figure 6.1 shows the Raspberry Pis suggested as upgrades.

Bibliography

- [1] Heidenhain,. EnDat Bidirectional Interface for Position Encoders. URL https://www.heidenhain.us/addl-materials/enews/stories_1012/EnDat.pdf. Online/Accessed on: Dec-2023.
- [2] Paul Scherrer Institute,. Layout of the SwissFEL, August 2023. URL <https://www.psi.ch/en/media/swissfel>.
- [3] Nolting, F., Bostedt, C., Schietinger, T., and Braun, H. The swiss light source and swissfel at the paul scherrer institute. *The European Physical Journal Plus*, 138(2):126, 2023. ISSN 2190-5444. doi: 10.1140/epjp/s13360-023-03721-y. URL <https://doi.org/10.1140/epjp/s13360-023-03721-y>.
- [4] Dalli, M., Calvi, M., Sammut, A., Sammut, N., and Schmidt, T. Development of a new magnetic measurement bench for in-vacuum undulators. *SN Applied Sciences*, 1(7):704, 2019. ISSN 2523-3971. doi: 10.1007/s42452-019-0725-8. URL <https://doi.org/10.1007/s42452-019-0725-8>.
- [5] Cassar, J., Sammut, A., Sammut, N., Calvi, M., Mitrovic, Z., and Popovic, R. S. Calibration and characterization of a reduced form-factor high accuracy three-axis teslameter, 2020.
- [6] Richter, S. High-Temperature Superconductor Application to Undulators for Compact Free-Electron Lasers. Anwendung von Hochtemperatursupraleitern auf Undulatoren für kompakte Freie-Elektronen-Laser, 2023. URL <https://cds.cern.ch/record/2859588>. Presented 05 May 2023.
- [7] Calvi, M., Camenzuli, C., Ganter, R., Sammut, N., and Schmidt, T. Magnetic assessment and modelling of the Aramis undulator beamline. *Journal of Synchrotron Radiation*, 25(3):686–705, May 2018. doi: 10.1107/S1600577518002205. URL <https://doi.org/10.1107/S1600577518002205>.
- [8] Vasserman, I., Gluskin, E., and Xu, J. Insertion devices: Magnetic measurements and tuning part 1 - magnetic sensors and measurement techniques, 01 2010.

- [9] J. Chavanne, C. P. ESRF insertion device field measurement benches. URL <https://www.esrf.fr/files/live/sites/www/files/Industry/files/magnetic-measuring-bench.pdf>. Accessed on 2023-11-22.
- [10] Grau, A., Baumbach, T., Casalbuoni, S., Gerstl, S., Hagelstein, M., Holubek, T., and Saez de Jauregui, D. Cryogen—free setup for local and integral magnetic field measurements of superconducting undulator coils. *IEEE Transactions on Applied Superconductivity*, 22(3):9001504–9001504, 2012. doi: 10.1109/TASC.2011.2179699.
- [11] Grau, A., Casalbuoni, S., Gerstl, S., Glamann, N., Holubek, T., Saez de Jauregui, D., Voutta, R., Boffo, C., Gerhard, T., Turenne, M., and Walter, W. Characterization of 30-cm-long superconducting undulator coils with the magnetic measurement system casper ii. *IEEE Transactions on Applied Superconductivity*, 26(4):1–4, 2016. doi: 10.1109/TASC.2016.2523806.
- [12] Campmany, J., Ribó, L., Colldelram, C., Becheri, F., Marcos, J., and Massana, V. A new bench concept for measuring magnetic fields of big closed structure. *Physics Procedia*, 75:1222–1229, 2015. ISSN 1875-3892. doi: <https://doi.org/10.1016/j.phpro.2015.12.124>. URL <https://www.sciencedirect.com/science/article/pii/S1875389215017630>. 20th International Conference on Magnetism, ICM 2015.
- [13] Marcos, J., Massana, V., García, L., and Campmany, J. Latest developments at the alba magnetic measurements laboratory. *Measurement Science and Technology*, 29(2):024002, jan 2018. doi: 10.1088/1361-6501/aa8ba2. URL <https://dx.doi.org/10.1088/1361-6501/aa8ba2>.
- [14] Tanaka, T., Tsusu, R., Nakajima, T., Seike, T., and Kitamura, H. In-situ undulator field measurement with the safali system. 01 2007.
- [15] SENIS - Magnetic & Current Measurement,. H3B Magnetic Transducers with Hybrid 1-2-3-axis Hall Probe sensors, . URL <https://www.senis.swiss/magnetometers/analog-magnetic-field-transducers/h3a-magnetic-transducers-with-hybrid-1-2-3-axis-hall-probe-sensors>. Accessed on: December-2023.
- [16] Thomas Schmidt,. New compact, modular in-vacuum undulator with magnetic force compensation, September 2023. URL <https://anl.app.box.com/s/91489ff8g3hykjzzzs1opz1edjhz5n3b>. Insertion Devices for Future Light Sources.

- [17] Elleaume, P., Chubar, O., and Chavanne, J. Computing 3d magnetic fields from insertion devices. In *Proceedings of the 1997 Particle Accelerator Conference (Cat. No.97CH36167)*, volume 3, pages 3509–3511 vol.3, 1997. doi: 10.1109/PAC.1997.753258.
- [18] Kinjo, R., Kagamihata, A., Seike, T., Kishimoto, H., Ohashi, H., Yamamoto, S., and Tanaka, T. Lightweight-compact variable-gap undulator with force cancellation system based on multipole monolithic magnets. *Review of Scientific Instruments*, 88(7):073302, 07 2017. ISSN 0034-6748. doi: 10.1063/1.4991652. URL <https://doi.org/10.1063/1.4991652>.
- [19] Yu, C., Zhu, Y., Zhang, W., Yang, J., He, Y., Zhen, T., Liu, T., Lei, Y., Yuan, Q., Yuan, D., Wen, Y., Deng, R., Jiang, Z., Deng, H., Liu, B., and Wang, D. Development of an apple iii undulator prototype with three-dimensional force compensation for shine. *Frontiers in Physics*, 11, 2023. ISSN 2296-424X. doi: 10.3389/fphy.2023.1174620. URL <https://www.frontiersin.org/articles/10.3389/fphy.2023.1174620>.
- [20] Faulhaber,. Brushless DC-Servomotors Series 0824 ... B. URL <https://www.faulhaber.com/en/products/series/0824b/#498>. Accessed on: December, 2023.
- [21] Zigbee Alliance,. ZigBee Pro Specification. URL <https://zigbeealliance.org/wp-content/uploads/2019/11/docs-05-3474-21-0csg-zigbee-specification.pdf>. Accessed on: December-2023.
- [22] FAULHABER,. Drive Electronics Support, . URL <https://www.faulhaber.com/en/support/drive-electronics/#q=MCBL%203002>. Accessed on: December-2023.
- [23] CiA,. CiA 301 CANopen application layer and communication profile, . URL <https://www.can-cia.org/groups/specifications>. Online.
- [24] CiA,. CiA 402 series CANopen device profile for drives and motion control, . URL <https://www.can-cia.org/can-knowledge/canopen/cia402/#>. Online.
- [25] Airex - An Allied Motion Company,. C-Series Ironless Linear Motors. URL <https://airex.com/wp-content/uploads/C-Series-Linear-Motor-Catalog.pdf>. Accessed on: December-2023.
- [26] FAULHABER,. Motion Controllers - Series MC 3001 P, . URL <https://www.faulhaber.com/en/products/series/mc3001p/>. Accessed on: December-2023.

- [27] Silicon Labs,. Si721x Field Output Hall Effect Magnetic Position Sensors Data Sheet. URL <https://www.silabs.com/documents/public/data-sheets/si721x-data-sheet.pdf>. Online/Accessed on: Dec-2023.
- [28] Faulhaber,. MOTION MANAGER 6 - MC V2.0/V2.5/SC. URL <https://www.faulhaber.com/en/support/ Faulhaber-motion-manager/#c78576>. PC Software.
- [29] Microchip,. Mcp25625 can controller with integrated transceiver data sheet, 2019. URL <https://ww1.microchip.com/downloads/en/DeviceDoc/MCP25625-CAN-Controller-Data-Sheet-20005282C.pdf>. Data sheet.
- [30] BROADCOM,. Microsoft word - bcm2835 arm peripherals.docx, 2019. URL <https://www.raspberrypi.org/app/uploads/2012/02/BCM2835-ARM-Peripherals.pdf>. Data sheet.
- [31] The kernel development community,. Socketcan - controller area network. URL <https://www.kernel.org/doc/html/next/networking/can.html>. Online, Accessed on: Dec-2023.
- [32] Hamamatsu,. Two-dimensional PSD S5990/S5991 series. URL https://www.hamamatsu.com/content/dam/hamamatsu-photonics/sites/documents/99_SALES_LIBRARY/ssd/s5990-01_etc_kpsd1010e.pdf. Data sheet - accessed on Dec-2023.
- [33] Beckhoff,. EL3702 - EtherCAT Terminal 2-channel - analog input - voltage +/-10 V - 16 bit - oversampling. URL <https://www.beckhoff.com/en-en/products/i-o/ethercat-terminals/el3xxx-analog-input/el3702.html>. accessed on Dec-2023.
- [34] Digi,. Digi xbee s2c 802.15.4 module. URL <https://hub.digi.com/support/products/digi-xbee/digi-xbee-s2c/>. accessed on Dec-2023.
- [35] Texas Instruments,. Tps709 150-ma, 30-v, 1-ua iq voltage regulators with enable, . URL https://www.ti.com/lit/ds/symlink/tps709.pdf?ts=1703199065752&ref_url=https%253A%252F%252Fwww.google.com%252F. Datasheet.
- [36] Texas Instruments,. 3-v to 5.5-v single-channel rs-232 1-mbits line driver and receiver with +/-15-kv iec esd protection, . URL <https://www.ti.com/lit/ds/symlink/sn65c3221e.pdf?ts=1703135945512>. Datasheet.
- [37] SENIS - Magnetic & Current Measurement,. Hall Probe S, . URL <https://www.senis.swiss/magnetometers/hall-probes/hall-probe-s/>. Accessed on: December-2023.

- [38] Analog Devices,. Full/low speed 5 kv usb digital isolator, 2012. URL <https://www.analog.com/media/en/technical-documentation/data-sheets/adum4160.pdf>. Data sheet.
- [39] Analog Devices,. 2.5 kv, isolated dc-to-dc converter, 2012. URL <https://www.analog.com/media/en/technical-documentation/data-sheets/adum5000.pdf>. Data sheet.
- [40] Jonas Malaco,. pyusb 1.2.1, July 2021. URL <https://pypi.org/project/pyusb/>. Online, Accessed on: Dec-2023.
- [41] Heidenhain,. Ak lic 411, ak lic 419 - (authorised documentation), 2023. URL https://product.heidenhain.de/JPBC/image/HWP.EN/hlr-system/AK_LIC411_LIC419_BA_1407031_Ver00_02_en.pdf. Operating Instructions.
- [42] Heidenhain,. Endat 2.2 implementation guide, 09 2021. URL https://endat.heidenhain.com/fileadmin/user_upload/endat/1302637-01-A-02_EnDat2-Implementation-Guide.pdf. Implementation Guide.
- [43] Atmel,. 8-bit avr microcontroller with 32k bytes in-system programmable flash, 09 2021. URL https://ww1.microchip.com/downloads/en/DeviceDoc/Atmel-7810-Automotive-Microcontrollers-ATmega328P_Datasheet.pdf. Datasheet.
- [44] Maxim Integrated,. Low-power, slew-rate-limited, rs-485/rs-422 transceivers, 09 2021. URL <https://www.analog.com/media/en/technical-documentation/data-sheets/MAX1487-MAX491.pdf>. Datasheet.
- [45] in Electronics, M. I. Cstne16m0v530000r0. URL <https://www.murata.com/en-global/api/pdfdownloadapi?cate=cgsubResonators&partno=CSTNE16MOV530000R0>. Datasheet.
- [46] Texas Instruments,. Bq2461x stand-alone 1- to 6-cell synchronous buck battery charger controller, 12 2019. URL https://www.ti.com/lit/ds/symlink/bq24610.pdf?HQS=dis-mous-null-mouser-mode-dsf-pf-null-ww&ts=1704060497960&ref_url=https%253A%252F%252Fwww.ti.com%252F. Datasheet.
- [47] Vishay General Semiconductor,. Surface mount transzorb transient voltage suppressors, 09 2022. URL <https://www.vishay.com/docs/89433/smc3k22ca.pdf>. Data sheet.
- [48] Traco Power,. Non-isolated dc/dc converter (pol) - tsr 2 series, 2 a, 09 2023. URL https://www.tracopower.com/sites/default/files/products/datasheets/tsr2_datasheet.pdf. Data sheet.

-
- [49] Traco Power,. Non-isolated dc/dc converter (pol) - tsrn 1 series, 1 a, 09 2023. URL <https://www.tracopower.com/int/tsrn1-datasheet>. Data sheet.
- [50] Traco Power,. Non-isolated dc/dc converter (pol) - tsr 2 series, 2 a, 09 2023. URL https://www.tracopower.com/sites/default/files/products/datasheets/tsr2_datasheet.pdf. Data sheet.
- [51] Analog Devices,. Spisolator digital isolators for spi, 2014-2017. URL https://www.analog.com/media/en/technical-documentation/data-sheets/adum3151_3152_3153.pdf. Data sheet.
- [52] Bracewell, R. N. and Bracewell, R. N. *The Fourier transform and its applications*, volume 31999. McGraw-Hill New York, 1986.
- [53] Raspberry Pi,. raspberry-pi-zero-2-w-product-brief.pdf, . URL <https://datasheets.raspberrypi.com/rpizero2/raspberry-pi-zero-2-w-product-brief.pdf>. Product Brief.
- [54] Raspberry Pi,. cm4-product-brief.pdf, . URL <https://datasheets.raspberrypi.com/cm4/cm4-product-brief.pdf>. Product Brief.

Appendix

Schematics of the Battery Charging Circuitry

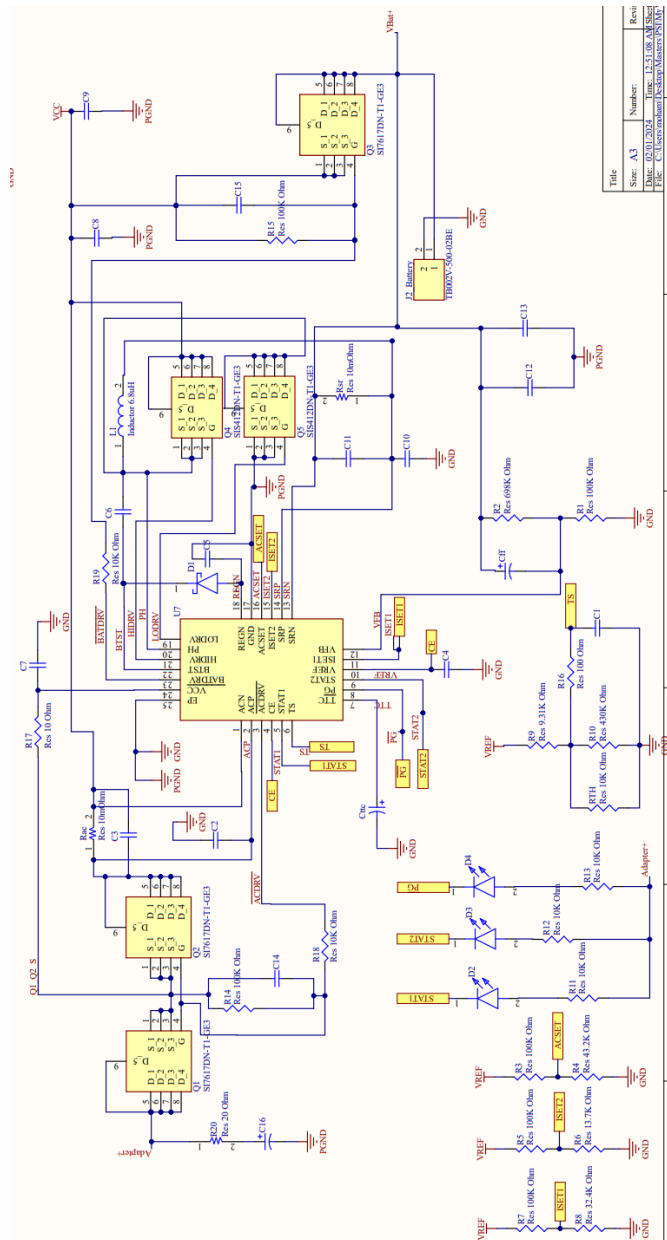


Figure A.1: The Schematics of the Stand-alone Battery Charger

Schematics of the PLC Side PCB

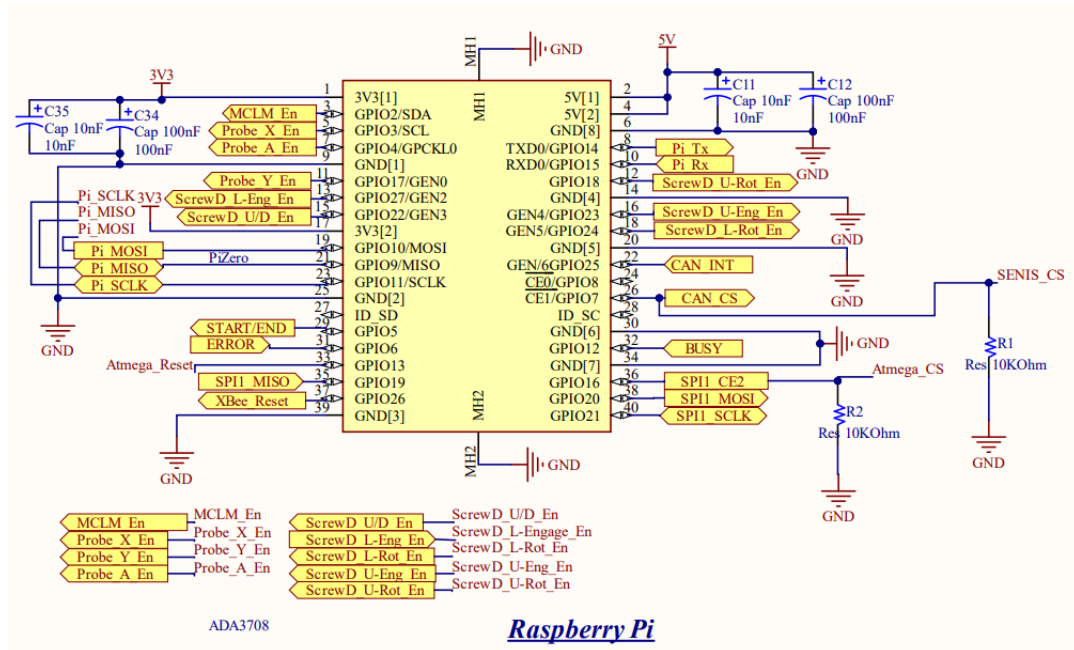


Figure A.2: The Schematics of the Raspberry Pi Zero W